Experimental Investigation of Flame-Wall Interaction by Laser-based Diagnostics

Am Fachbereich Maschinenbau
an der Technischen Universität Darmstadt
zur
Erlangung des Grades eines Doktor-Ingenieurs (Dr.-Ing.)
genehmigte

Dissertation

vorgelegt von

Hidemasa Kosaka, M. Sc.

aus Tokyo, Japan

Berichterstatter:	Prof. Dr. habil. A. Dreizler
Mitberichterstatter:	Prof. Dr.-Ing. C. Hasse
Tag der Einreichung:	06.11.2018
Tag der mündlichen Prüfung:	23.01.2019

Darmstadt 2019

D17

Preface

This work has been conducted during my time as a doctoral candidate at the institute of Reacting Flows and Measurement Techniques (RSM) at the Technische Universität Darmstadt.

I cordially thank my supervisor Prof. Dr. habil. Andreas Dreizler, who gave me the opportunity to work in a highly motivating, scientific atmosphere. The successful outcome of this work is primarily founded on our continuous discussions as well as his scientific foresight and good company. Further thanks are extended to Prof. Dr.-Ing. Christian Hasse for not only taking over the co-referee, but also the very fruitful discussions on many aspects of the flame fundamentals.

During the last three years, I enjoyed the collaboration with my colleagues. They are always ready for deep discussions and also chatting. From them, I received continuous support, excellent ideas and encouragement. My special thanks go to colleagues in the flame-wall interactions studies: Dr.-Ing. Christopher Jainski, Martin Rißmann and Florian Zentgraf. Without you this work would not be possible. Furthermore, I thank my office colleagues, especially for companions: Max Greifenstein, Sani Van der Kley, Nicola Luciano and Cooper Welch. It was a nice time with you. This also applies to the colleagues at the partner institutes of EKT and STFS. In particular, thanks go to Arne Scholtissek for your helpfulness and interest in many topics.

The cooperative atmosphere in the laboratory was very important to me. The list of people who could be mentioned here is long, so I thank Jan Köser, Lukas Becker, Carl-Philipp Ding, Andreas Preusche, Jhon Pareja and Dr. Ayane Johchi.

I would also like to thank the workshop team headed by Roland Berntheisel. The precise production of the components was the basis of all near-wall experiments. Thanks also to Andreas Ludwig and all the staff of the secretary, who have continuously contributed to the success of the work in the background.

Finally, I thank my wife Tomoko and my family for their support and patience. Especially during the finalization stage of the thesis, my sons Haruki and Sota provided me necessary distraction which always facilitated my work.

Hidemasa Kosaka

Darmstadt, November 2018

Abstract

Flame quenching resulting from flame-wall interactions (FWIs) is important in several thermochemical processes of practical relevance, such as internal combustion engines. Even though FWIs are restricted to regions close to walls of a combustion chamber, they are crucial for wall heat fluxes and unburned hydrocarbon emissions. This experimental work is intended to investigate parametric sensitivities that influence flame quenching at walls and to better understand the influence of non-adiabaticity upon the flame structure. This work uses quantitative and semi-quantitative laser-based diagnostics with high temporal and spatial resolution simultaneously. Experiments are performed on a generic burner with side-wall quenching configurations, where a branch of a V-flame interacts with a laterally oriented wall. Laminar and turbulent boundary conditions are generated for various wall temperatures and two different fuels (methane and dimethyl ether). To investigate the influence of wall heat flux on flame quenching, coherent anti-Stokes Raman spectroscopy (CARS) and phosphor thermometry are combined. From the measurements, gas and wall temperature profiles, wall heat fluxes and quenching distances are deduced and correlated. A further measurement of thermochemical states that provide the opportunity to look at the flame dynamics with flame chemistry. The simultaneous measurement of CARS (for the gas temperature) and laser-induced fluorescence (LIF) of carbon monoxide (CO) (for the CO concentration) are applied. Above all, an influence of the time scales of heat transfer on CO chemistry is shown. Furthermore, simultaneous planar LIF of the formaldehyde molecule and the hydroxyl radical are used to image local heat release rate (HRR) distributions. In the turbulent case, flame fluctuations prevail in the FWI zone and are analyzed statistically regarding flame curvature. The correlation of heat release rate, flame curvature and wall-normal distance is investigated using the instantaneous HRR images for different wall temperatures and equivalence ratios. Finally, the feasibility study of the near-wall Raman spectroscopy is carried out. Raman spectroscopy is a promising technique to quantify combustion-related species simultaneously. However, especially near the wall, scattering and reflections from the wall are even higher than that of the other measurement techniques. The purpose of this feasibility study is to characterize the Raman signal quality near the wall. The resulting signal-to-noise ratio is found to be suitable for further measurements.

Kurzfassung

Flammenverlöschen, das aus Flamme-Wand-Interaktionen (FWI) resultiert, ist in einer Vielzahl von technischen Prozessen wie z.B. in Verbrennungsmotoren, von praktischer Relevanz. Obwohl FWI auf Bereiche in der Nähe von Wänden einer Brennkammer beschränkt sind, sind sie entscheidend für die Wandwärmflüsse und die Bildung unverbrannter Kohlenwasserstoffe. Diese experimentelle Studie soll parametrische Sensitivitäten untersuchen, die das Flammenverlöschen an Wänden beeinflussen, und den Einfluss der Nichtadiabatizität auf die Flammenstruktur besser verstehen. Diese Arbeit beinhaltet quantitative und semiquantitative Messungen mit gleichzeitig hoher zeitlicher und räumlicher Auflösung. Die Experimente werden an einem generischen Brenner durchgeführt, bei dem ein Zweig einer V-Flamme mit einer seitlich orientierten Wand interagiert. Laminare und turbulente Randbedingungen werden für verschiedene Wandtemperaturen und zwei unterschiedliche Brennstoffe (Methan und Dimethylether) erzeugt. Um den Einfluss des Wandwärmestroms auf das Flammenverlöschen zu untersuchen, werden kohärente Anti-Stokes-Raman-Spektroskopie (CARS) und Phosphorthermometrie kombiniert. Aus den Messungen werden Wandwärmeströme und Verlöschabstände abgeleitet und korreliert. Die weitere Messung thermochemischer Zustände bietet die Möglichkeit, die Flammendynamik mit der Flammenchemie zu untersuchen. Dazu wird die gleichzeitige Messung der Gastemperatur mittels CARS und der CO-Konzentration mittels laserinduzierte Fluoreszenz (LIF) von CO genuzt. Es zeigt sich ein Einfluss der Zeitskalen der Wärmeübertragung auf die CO-Chemie. Außerdem werden simultane planare LIF-Messungen des Formaldehyd und des Hydroxyl-Radikals verwendet, um Verteilungen der lokalen Wärmefreisetzungsrate (HRR) abzubilden. Im turbulenten Fall sind Flammenschwankungen in der FWI-Zone vorherrschend und werden hinsichtlich die Korrelation von HRR, Flammenkrümmung und Wandnormalenabstand statistisch analysiert. Schließlich wird die Machbarkeitsstudie der wandnahen Raman-Spektroskopie vorgestellt. Die Raman-Spektroskopie ist eine vielversprechende Methode zur gleichzeitigen Quantifizierung verbrennungsrelevante Spezies. Verglichen mit der Signalstärke sind jedoch insbesondere in Wandnähe die Streuungen und Reflexionen an der Wand stärker als bei den anderen Messtechniken. Ziel dieser Machbarkeitsstudie ist es, die Raman-Signalqualität in Wandnähe zu charakterisieren. Das resultierende Signal-Rausch-Verhältnis erscheint für weitere Messungen als geeignet.

Contents

Nomenclature

Upper-case Latin letters		Unit
A	Area	m^2
A_{21}	Einstein A-coefficient for spontaneous emission	$1/s$
C_{Cal}	Global correction coefficient	–
D	Diameter	m
C_{CO_T}	Spectroscopic temperature correction coefficient	–
C_{Geo}	Geometrical correction coefficient	–
D	Diffusion term	kg/m^3s
D_k	Diffusion coefficient of species k	m^2/s
D_α	Thermal diffusion coefficient	m^2/s
Da	Damköhler number	–
E	Activation energy	J/mol
I	Intensity	–
Ka	Karlowitz number	–
L	Characteristic length	m
Le	Lewis number	–
Nu	Nusselt number	–
P	Electrical polarization	As/m^2
Pe	Peclet number	–
Pr	Prandtl number	–
R	Universal gas constant	J/molK
R	Correlation value	–
Re	Reynolds number	–
S	Signal intensity	–
Sc	Schmidt number	–
T	Temperature	K
V	Volume	m^3
X_k	Mole fraction of the species k	–
Y_k	Mass fraction of the species k	–

Lower-case Latin letters		Unit
a	Normalization factor	–
b	Exponential factor	–

c	Progress variable	–
c_p	Specific heat capacity	J/kgK
f	Focal length	m
h	Planck constant	J s
k_B	Boltzmann constant	J/K
$\vec{k}$	Wave vector	1/m
l	Structure size	m
l_0	Integral length scale	m
l_k	Kolmogorov length scale	m
p	Pressure	$\mathrm{N/m^2}$
$\dot{q}$	Heat flux	$\mathrm{W/m^2}$
$\dot{q}_\mathrm{N}$	Dimensionless heat flux	–
r	Radius	m
s_L	Laminar flame speed	m/s
s_T	Turbulent flame speed	m/s
t	Time	s
u	Velocity	m/s
u^*	Friction velocity	m/s
v	Vibration quantum number	–
x, y, z	Cartesian coordinates	m
y^+	Dimensionless wall distance	–

Upper-case Greek letters		**Unit**
Δ	Distance	m
Ω	Solid angle	sr
Ψ	Wave function	$1/\sqrt{\mathrm{m^3}}$

Lower-case Greek letters		**Unit**
α	Heat transfer coefficient	$\mathrm{W/m^2K}$
α, β, γ	Angle	deg
δ_F	Flame thickness	m
δ_T	Thermal boundary layer thickness	m
δ_Q	Quenching distance	m
ϵ	Dissipation rate	J/kgs
ϵ_0	Electric field constant	As/Vm
η	Transmission constant	–
λ	Thermal conductivity	W/mK
λ	Wavelength	nm
μ	Molecular viscosity	kg/ms
ν	Wavenumber	1/cm

ν	Kinematic viscosity	m^2/s
ϱ	Density	kg/m^3
σ	Absorption cross section	m^2
τ_k	Kolmogorov time scale	s
ϕ	Fuel/Air ratio (equivalence ratio)	–

Indices

ad	Adiabatic
BG	Background
e	Electric
F	Flame
fl	Fluorescence
i	Spatial direction
j	Reaction
k	Species
L	Laminar
T	Turbulent

Abbreviations

CARS	Coherent anti-Stokes Raman Spectroscopy
CCD	Charge-Coupled Device
CFD	Computational Fluid Dynamics
CL	Chemiluminescence
CMOS	Complementary Metal-Oxide-Semiconductor
DNS	Direct Numerical Simulation
FWHM	Full Width at Half Maximum
FWI	Flame-Wall Interaction
IC	Internal Combustion
ICCD	Intensified CCD
LES	Large Eddy Simulation
LIF	Laser-Induced Fluorescence
OH	Hydroxyl radical
PIV	Particle Image Velocimetry
PLIF	Planar LIF
PTV	Particle Tracking Velocimetry
SWQ	Side-Wall Quenching
TG	Turbulence Grid

1 Introduction

1.1 Background and motivation

Energy supply via combustion is one of the primary bases of our society. However, carbon monoxide (CO), carbon dioxide (CO_2), unburned hydrocarbons (UHC) and further harmful pollutants are formed during combustion processes. Climate-change concerns and legislative regulations require adequate solutions to reduce the impact of combustion on global warming. One of the main drivers of such harmful pollutants is the transportation sector. This sector, for example, contributed about 24 % of the world CO_2 emissions in 2017 [136]. The primary goals of the development of combustion technology are improving thermal efficiency and decreasing pollutant emissions.

Focusing on combustion applications with a closed geometry such as gas turbines and internal combustion engines, flames are spatially limited by the walls of the combustion chamber in their propagation [47, 53, 95]. The surfaces of the walls generally have significantly lower temperatures (max. $\approx$ 700 K) than typical hydrocarbon flame temperatures ($\approx$ 2200 K). When the flame approaches the wall, a large heat flux to the wall is caused due to the large temperature difference. It comes to the extinction of radicals and thus the flame quenches at a small distance from the wall (called *quenching distance*). Even though such flame-wall interactions (FWIs) are limited to regions very close to the walls, they are crucial for the formation of UHC, CO and wall deposits [32, 47] and overall heat losses relevant to the thermal efficiency. Increasing power densities associated with the recent trend of downsizing [67] cause a rising surface-to-volume ratio, i.e. a more pronounced impact of the FWI, which motivates detailed studies of the FWI.

From previous studies, it has been already observed that the FWI is a very complex process. Not only the above-mentioned interactions between the flame and the wall, but also the interaction of the flame with the wall-close flow field has the large influence on the combustion process. For the investigation of such mutually related processes (turbulence, wall friction, heat transfer and combustion process), the simultaneous determination of temperatures, species concentrations and velocities is necessary.

Strong growth in computational capacity over the last two decades can contribute to a multi-dimensional analysis of the FWI. However, today's computing

capacity is still far from sufficient to simulate real combustion systems using direct numerical simulation (DNS). In order to reduce computation times, the approach of the large eddy simulation (LES) is widely applied, where the flow field and combustion chemistry are spatially resolved in the computing grid scale. For the unresolved scales, combustion and turbulence models are required. In particular, close to the wall, current models sometimes fail and need circumvent a few artifices, such as the adiabatic wall or the disappearance of the chemical source term on the wall. For the development of such models, a variety of validation data from experiments with well-defined boundary conditions are of great importance.

The development of advanced diagnostic techniques is triggered by such requirements of both experimental tools for the investigation of the relevant phenomena to the FWI and numerical modeling. Despite its importance, experimental investigations of the FWI are still challenging due to the small characteristic space and time. Laser-based measurement methods offer high temporal and spatial resolutions and are suited for simultaneous multi-parameter measurements.

1.2 State of the art in FWI studies

FWI research was started early in the 19th century by H. Davy [46], who investigated mine-lamp flame quenching in small tubes. Since that time, FWI remained a typical topic in areas such as surface ignition [36], micro combustion technology, gas turbines [22], rocket engines [125] and in the design process of combustion chambers in IC engines [73]. Because laser diagnostics have proven their superiority of of high-resolution, non- or minimally invasive, accurate and precise measurements in harsh high-temperature environments, they have been widely used and developed in the past decades. This section gives the current state of laser diagnostics in combustion science and both experimental and numerical FWI studies.

1.2.1 Laser diagnostics in combustion

For the measurement of relevant combustion parameters such as temperature, species concentration and velocity, the measurement techniques must be chosen so that they disturb the process as little as possible. For example, the introduction of thermocouples into the boundary layer would significantly influence the flow field and the flame, which impedes the measured signal. The use of established methods of laser diagnostics has an advantage due to their non-intrusion for temporally and spatially imaging of the FWI.

The commonly used methods to measure temperatures in reacting flows are Rayleigh scattering [132], coherent anti-Stokes Raman spectroscopy (CARS) [152] and laser-induced fluorescence (LIF) of a tracer [157]. Because Rayleigh signals result from elastic scattering processes on molecules, the detected wavelength is equal to that one of the used laser light. Since the Rayleigh signal intensities from high temperature molecule are orders of magnitude smaller than the surface-reflected or scattered excitation laser light, the signals are superimposed by stray light and cannot be spectrally separated. To suppress a certain amount of such reflection and scattering, filtered Rayleigh scattering (FRS) has been developed recently [92]. Another method for gas phase thermometry is tracer-LIF. It has the ability to separate the excitation and detection wavelengths. However, it is necessary to introduce a tracer which must be homogeneously mixed with the probed flows. The tracers are usually solvents (acetone, toluene, 3-pentanone), which are flammable, and consequently already consumed before approaching the main reaction zone. Furthermore, tracer-LIF methods require a complex calibration. CARS thermometry is a nonlinear, four wave mixing process that generates a coherent blue-shifted wavelength signal. The generated CARS signal contains spectral information of the Boltzmann-distributed quantum mechanical state. A precise and calibration-free determination of the temperature can be realized by comparison with theoretical spectra. The main advantage is its small probe volume size. In principle, it is possible to measure temperature at distances of less than 70 microns from the wall surface [126], and is used in this work.

The determination of species concentrations is typically carried out by means of LIF or Raman spectroscopy. While LIF excites only one species, Raman spectroscopy enables to capture of all combustion-related major species and some intermediate ones simultaneously with a single laser shot. However, the signal intensities of Raman are low and they must be combined with thermometry for the density and spectroscopic correction. For quantitative LIF measurements, the temperature information is also needed.

Velocity fields can be determined by means of laser doppler velocimetry (LDV) or particle image velocimetry (PIV). LDV allows the point-wise detection of all three components of the velocity vector. The repetition rate depends on the number of tracer particles introduced into the flow field. PIV also requires tracer particles which can be detected by Mie scattering, and a velocity field can be calculated from the temporal particle displacements. For PIV, two velocity components in the measurement plane are determined with one camera. By using two or more cameras, the third velocity component can also be determined.

1.2.2 Experimental flame-wall interaction studies

The first systematic investigations of the FWI characterized the quenching distance of propane/air flames using parallel plates [68, 69]. For stoichiometric propane flames, the quenching distance was found to be about 2 mm. More complex geometries were introduced in the form of internal combustion engines [45]. Photographs of flame radiation showed the approximate position of the flame front which were in agreement with the calculated quenching distances. For the internal combustion engine, an ion probe flame detection was also devised through a gap inside the combustion chamber to provide quenching distances. It showed that quenching distances range from 0.1 mm to 2 mm [81]. Several experimental studies have shown the correlation between the quenching distance and the wall heat flux. Huang et al. [93] characterized the heat flux of the wall experimentally and numerically in a one-dimensional configuration. Lu et al. [122] applied a similar approach to study heat fluxes in a constant volume chamber where the flame propagated parallel to a flat wall. Further studies varied the wall temperature in different generic flame geometries [38, 65]. The variation of the wall material and pressure was also performed in a closed configuration and quenching distances were characterized using direct photography of the flame [10, 165]. It was observed that quenching distances decreased with increasing wall surface temperatures. A parametric study of the wall material was also performed using a single cylinder engine [74, 188]. The global heat flux was found to increase with rising in-cylinder wall temperatures for a combustion chamber coated with ceramics, which showed an opposite trend compared to the results in non-reacting geometries.

Boust et al. [21] introduced a simplified thermal formulation which allows the evaluation of quenching distances from wall heat fluxes and mixture properties. They proposed an equation for quenching distances as a function of the fuel/air ratio and the heat release rate in an unstretched steady laminar flame. Fuyuto et al. [75] performed spectroscopic measurements of temperature and flame radicals such as OH, CH_2O and CO in the quenching boundary layer with a premixed methane/air flat flame. They revealed limitations of 200 μm in spatial resolution attributed to the refraction of fluorescence, which is in the range of the quenching distance for a methane/air flame. Further studies were performed to measure the temperature and major species distributions in the near-wall region by Bohlin et al. [14]. They enabled the determination of thermochemical states (temperature and major species) in the thermal boundary layer within $\approx$ 30 μm from the wall. In addition, carbon monoxide (CO) measurements complementing the temperature data were performed in [100, 126]. Combined measurements of wall heat fluxes and velocities were reported by Egolfopoulos et al. [60] and compared with one-

dimensional simulations of stagnation flames. Experimental investigations in an internal combustion engine were carried out in [19] and a correlation between the flow field and heat fluxes was found.

For a complete understanding of the FWI, the simultaneous investigation of several variables is necessary because they are interdependent. Some of the recent challenges presented here realized such simultaneous measurements by using laser diagnostic techniques. However, it is still difficult to apply these diagnostic methods in FWI environments due to following reasons [54]:

- lack of spatial resolution to detect the smallest structures or a limited dynamic range to accommodate all relevant scales,
- poor signal-to-noise ratio due to scattered light from the wall surfaces,
- low concentration of particles or tracers for the measurement,
- optical accessibility of the near-wall regions, especially in technically relevant configurations.

In this work, the approach for laser-based measurements is therefore chosen carefully. CARS, LIF, phosphor thermometry and PIV are used in this work and they are characterized by means of spatial and temporal resolution, precision and accuracy, which are presented in Section 5.1 and 6.1.

1.2.3 Numerical flame-wall interaction studies

Early on, Lewis and von Elbe developed a "thermal theory" to describe flame quenching [116], which von Kármán improved through insights from aerodynamics [181]. Several authors performed one-dimensional simulations combined with detailed chemistry [64, 144, 187]. Popp et al. gave a good agreement of the maximum heat flux at the cold wall (T_{wall} = 300 K) with experimental results [144]. At higher wall temperatures (T_{wall} = 600 K), however, the result showed an increasing discrepancy, where there is an influence of increasing radical concentration and subsequent strongly exothermic radical recombination reactions. The higher wall temperature made the wall no longer chemically inert and the simulation results deviated from experimental observations. Further studies focused on the combustion of more complex hydrocarbons with regard to detailed kinetics near the wall [189].

The computing capacity of modern high performance computers allows a multidimensional analysis of the flame-wall interaction. Two-dimensional direct numerical simulation (DNS) of a methane/air flame with detailed chemical reaction

kinetics has been reported by Andrae et al. [3]. The considered equivalence ratios ($0.2 < \phi < 0.4$), however, are close to the lower ignition limit for atmospheric flames and have little relevance in practical combustion systems.

The influence of turbulence on quenching flames by means of three-dimensional DNS and a one-step global reaction mechanism was investigated by Bruneaux et al. [28] and a flamelet-based model was developed by Bruneaux et al. [29], which provides a good representation of DNS results. Three-dimensional DNS with detailed chemistry is still extremely cost-expensive. Therefore, approaches with reduced reaction mechanisms [33] are currently being used in order to calculate the pollutant production during engine combustion. Studies based on detailed chemical reaction mechanisms in the DNS context have been limited to the simulation of turbulent hydrogen flames [84], whose combustion behavior is significantly different from that of hydrocarbon-based fuels.

A numerical description of the flame-wall interaction in a three-dimensional complex fuel environment has not previously been reported in the literature, and a deterministic prediction of pollutant production in technical systems is currently not possible. One of the motivations of this work is therefore to provide validation data to close this gap.

1.3 Aim and structure of this work

Despite the many insights from the investigations mentioned above, a number of issues in the study of FWI still remain. Moreover, recent developments in laser and camera technologies have enabled further investigations.

The aim of this work is to investigate parametric sensitivities that influence fundamental properties of flame quenching at walls and to better understand the influence of non-adiabaticity upon the flame structure. For this reason, this work deals with simultaneous multi-parameter measurements relevant to the FWI simultaneously. The investigated flames have defined boundary conditions and high reproducibility of the experiments, which is realized by using a canonical flow configuration. Consequently, the different key parameters on FWI can be considered as separate as possible from other effects.

In the investigations carried out in this work, the main focuses are the following three topics:

- wall heat flux related to quenching distances,
- the behavior of the thermochemical states in terms of gas phase temperature and CO concentration during the FWI,

- the influence of the near-wall flame curvature on the local heat release rate,

including the effect of higher wall temperatures and the use of methane and dimethyl ether (DME) for fuel. Studying elevated wall temperatures is important in the FWI as wall temperature is a key controlling parameter for flame quenching. Both, the recent trend of IC-engine downsizing and innovative insulation methods for combustion chambers [183] result in elevated surface temperatures of combustor walls. Furthermore, the investigation of alternative fuels is considered relevant, as they feature the potential of reduced exhaust gas emissions. Methane has been widely used in experiments which facilitate the modeling of the chemical reactions because it is the most simple hydrocarbon, whereas DME has excellent properties as an alternative diesel fuel, yielding lower emission levels compared to conventional diesel fuel [160].

The structure of this thesis begins with some essential fundamentals in Chapter 2, which help to understand the combustion, especially the near-wall contribution. In Chapter 3 the methodologies on laser-based diagnostics, which are used to study the flame-wall interaction, are described. Chapter 4 presents the generic flame-wall interaction burner used for measurements. It includes the description of laminar one-dimensional flame calculations which is carried out to complement the experimental study. In the following Chapters 5 and 6, the experimental setups are presented and the applied measurement techniques are characterized in the context of this work. The results of the investigations are presented and discussed. As an outlook to further investigations, a feasibility study of near-wall Raman spectroscopy is discussed in Chapter 7. The work concludes in Chapter 8 with a summary of the obtained knowledge and an outlook.

2 Fundamentals

This chapter provides an insight into fluid dynamics, heat transfer and a brief overview of the current understanding of premixed combustion including the flame-wall interaction (FWI). A more detailed introduction to combustion is in the textbooks of Lewis and von Elbe [116], Warnatz et al. [185], Poinsot and Veynante [142], Turns [177] and Cant and Mastorakos [31]. The description of flows and the turbulence was provided by Spurk and Aksel [166] and Pope [143] as well as for boundary layers by Schlichting and Gersten [154].

In principle, combustion can be divided into two extreme cases, namely, premixed combustion, where the fuel and oxidizer are homogeneously mixed before reaction, and non-premixed combustion (diffusion flames), where the fuel and oxidizer are provided separately. There is a transition area called partially premixed combustion. In terms of FWI, most previous studies have dealt with premixed combustion, relevant to gasoline engines, while non-premixed combustion, which is important for diesel and rocket combustion, has been studied seldom [43, 184]. Some recent innovative combustion systems, such as Premixed Charge Compression Ignition (PCCI) combustion, go through these different modes of combustion according to their time scales. Because this work focuses on only the FWI of premixed flames, the presented fundamentals are limited to premixed combustion.

Another subdivision in combustion is based on the number of existing phases. For example, in direct-injection gasoline engines, fuel is injected in liquid phase into the combustion chamber, where it evaporates and burns. However, this work deals only with single-phase combustion, where the fuel is always in gaseous phase.

Most practical combustion applications are operated in a turbulent flow regime, since it is possible to significantly increase the fuel conversion rate compared to a non-turbulent (laminar) configuration. Nevertheless, laminar flames are still important for a fundamental understanding of combustion. A large number of concepts for describing turbulent flames are based on models constructed for laminar flames [142]. Another advantage of investigating laminar flames is that they can realize well-defined boundary conditions both experimentally and numerically. Therefore, this work focuses on both configurations and the following sections provide the fundamentals on fluid dynamics of laminar and turbulent regimes.

2.1 Fluid dynamics

2.1.1 Free stream

Combustion of gaseous fuels consists of a large number of chemical reactions in an environment influenced by fluid dynamics. The general approach to describe these fluid dynamics is the use of conservation equations [143]. The basis is the conservation of mass described as

$$\frac{\partial \varrho}{\partial t} + \frac{\partial}{\partial x_i}(\varrho u_i) = 0, \tag{2.1}$$

where $\partial \varrho / \partial t$ represents the change in density over time and u_i is the local velocity.

Another important component in the calculation of the fluid flow is the conservation of the momentum (so-called Navier-Stokes equation). The equation, independently developed by Claude Navier [135] and George Stokes [171], represents the application of the Newton's law to a continuum as

$$\frac{\partial}{\partial t}(\varrho u_i) + \frac{\partial}{\partial x_j}(\varrho u_i u_j) = -\frac{\partial p}{\partial x_i} + \frac{\partial \tau_{ij}}{\partial x_j} + \varrho g_i. \tag{2.2}$$

Here, p represents the local pressure, τ_{ij} is the stress tensor and g_i is the gravity vector.

Considering combustion processes, it usually results in an inhomogeneous temperature distribution and a chemical conversion of individual species. These additional processes require further equations to describe the processes. A changing species concentration is considered by means of a transport equation of the mass fraction, Y_k, of each species [59].

$$\frac{\partial}{\partial t}(\varrho Y_k) + \frac{\partial}{\partial x_j}(\varrho Y_k u_j) = -\frac{\partial}{\partial x_j}\left(\varrho D_k \frac{\partial Y_k}{\partial x_j}\right) + \dot{\omega}_k. \tag{2.3}$$

Equation (2.3) shows that species transport can occur by convection (second term on the left side) and by diffusion (first term on the right side). The species diffusion is determined by Fick's law and the diffusion coefficient, D_k. The last term on the right side $\dot{\omega}_k$ stands for the chemical source term which plays a important role in combustion applications through the conversion of the fuel.

The last necessary equation for describing non-isothermal flows is the energy equation. The conservation of energy can be represented by various thermodynamic parameters such as temperature, T, internal energy, e, or enthalpy, h. In practical applications, the use of enthalpy has been proven to be appropriate. The conservation of energy is given as [59]

$$\frac{\partial}{\partial t}(\varrho h) + \frac{\partial}{\partial x_j}(\varrho h u_j) = -\frac{\partial}{\partial x_j}\left(c_p \varrho D_\alpha \frac{\partial T}{\partial x_j}\right) + \dot{\omega}_T + \dot{Q}. \tag{2.4}$$

The conservation of energy with convection and diffusion terms shows a similar structure as the species conservation. D_α stands for the thermal diffusion coefficient, c_p for heat capacity at constant pressure and $\dot{\omega}_T$ for heat release by combustion. The term $\dot{Q}$ considers external enthalpy input or losses.

Huge efforts have been taken to fully understand and solve these equations due to their enormous relevance to many kinds of practical applications. However, there is no mathematical proof to provide analytical solutions for given boundary conditions in real reacting flows.

Depending on the specific problem, it is possible to simplify the set of equations due to their similarity in the structure. An important method is to introduce dimensionless numbers which can be defined [109, 117, 143] as

$$\mathrm{Pr} = \frac{\nu}{D_\alpha} \mathrel{\hat{=}} \frac{\text{momentum diffusion (kinematic viscosity)}}{\text{thermal diffusion}}, \tag{2.5}$$

$$\mathrm{Sc} = \frac{\nu}{D_\mathrm{k}} \mathrel{\hat{=}} \frac{\text{momentum diffusion (kinematic viscosity)}}{\text{species diffusion}}, \tag{2.6}$$

$$\mathrm{Le} = \frac{D_\alpha}{D_\mathrm{k}} \mathrel{\hat{=}} \frac{\text{thermal diffusion}}{\text{species diffusion}}. \tag{2.7}$$

The Prandtl, Schmidt and Lewis numbers (Pr, Sc, Le) describe the relations between the different diffusion coefficients. In addition to these numbers, a characteristic dimensionless Reynolds number, Re, was introduced to describe the transition from laminar to turbulent as follows [149],

$$\mathrm{Re} = \frac{uL}{\nu} \mathrel{\hat{=}} \frac{\text{convection of momentum}}{\text{diffusion of momentum}} \tag{2.8}$$

with the characteristic velocity, u, the characteristic length scale, L, and the kinematic viscosity, ν. The Reynolds number describes the ratio between destabilizing

flow momentum and stabilizing viscous forces. For low Reynolds numbers the influence of frictional forces prevails over the inertial forces, thus resulting in a laminar flow. With increasing u or decreasing ν the influence of the inertial forces increases, resulting in a more unstable flow, i.e. a turbulent flow. The point of transition is not fixed, depending strongly on the geometry of the domain.

In general, turbulent flows contain a variety of flow structures of different sizes. A fully developed turbulent flow has a continuous spectra of length scales as shown in Fig. 2.1 with logarithmic scales of wavenumber, k, and the frequency spectrum, E. The large eddies are generated due to the shear stress caused by velocity gradients in the energy containing range. They are deformed and shrink in size while distributing their energy to smaller structures in the inertial range, where a theoretical equation can be derived as $E(k) \sim k^{-5/3}$ [143]. At the smallest scales, the energy is dissipated into thermal energy. The distribution of turbulent energy over different scales can be interpreted as an energy cascade. The smallest scales (called Kolmogorov scales) are in equilibrium with energy transfer from larger scales and energy loss by viscous dissipation according to Kolmogorov [111]. The Kolmogorov scales for length, l_k, and for time, τ_k, can be determined by the dissipation rate, ϵ, and the kinematic viscosity, ν,

$$l_\mathrm{k} = \left(\frac{\nu^3}{\epsilon}\right)^{1/4} \tag{2.9}$$

$$\tau_\mathrm{k} = \left(\frac{\nu}{\epsilon}\right)^{1/2}. \tag{2.10}$$

Furthermore, turbulent flows are characterized by other scales using the velocity field, for instance, the integral length scale, l_0 plays an important role as it carries most of the turbulent kinetic energy (see Fig. 2.1). The integral scale can be determined by calculating autocorrelations of the velocity fluctuation components in space and time [175]. A normalized autocorrelation function, R_{ii}, of the velocity fluctuation components, u_i', is given by

$$R_{ii}(x,t,l) = \frac{\overline{u_i'(x,t)u_i'(x+l,t)}}{\sqrt{\overline{u_i'^2(x,t)}}\sqrt{\overline{u_i'^2(x+l,t)}}}, \tag{2.11}$$

$$R_{ii}(x,t,\tau) = \frac{\overline{u_i'(x,t)u_i'(x,t+\tau)}}{\sqrt{\overline{u_i'^2(x,t)}}\sqrt{\overline{u_i'^2(x,t+\tau)}}}. \tag{2.12}$$

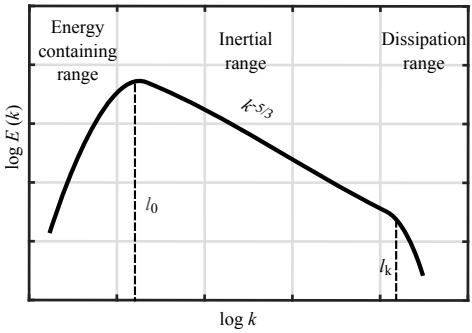

Figure 2.1. Schematic of the turbulent kinetic energy, E, spectrum as a function of the wavenumber k adapted from [143].

in space and time, respectively.

For $l = 0$ and $\tau = 0$, the data is correlated with itself and $R_{ii} = 1$. With increasing displacement, l or τ, the autocorrelation decreases. It is possible that the function takes a negative value. This is the case, for example, when an oscillating measurement signal is shifted by half a phase length [102].

This autocorrelation function can be used to determine appropriate integral scales as follows,

$$l_0(x,t) = \int_0^\infty R_{ii}(x,t,l)dl \tag{2.13}$$

$$\tau_0(x,t) = \int_0^\infty R_{ii}(x,t,\tau)d\tau \tag{2.14}$$

where τ_0 represents the integral time scale. In particular, the l_0 and τ_0 can be defined as the integral of the determined autocorrelation up to the first zero crossing of R_{ii} and is of practical relevance [175].

2.1.2 Near-wall flows

Special care is required with the flow field in the vicinity of the wall. The layer of fluid in the vicinity of a wall is called a boundary layer. In the boundary layer, the

viscosity of the fluid plays the dominant role. The viscosity reduces the mean velocity of the free flow until it comes to zero at the wall due to the no slip condition. Figure 2.2 shows the wall-normal velocity profile of a laminar boundary layer on a flat plate. The thickness of the boundary layer, δ_b, can be defined as the distance from the wall where the mean velocity is as high as 99 % of the free stream velocity u_0, expressed as

$$\delta_b = y(u = 0.99u_0). \tag{2.15}$$

A mathematically superior definition than the arbitrary boundary layer thickness is the displacement thickness [143]:

$$\delta_b = \int_0^\infty \left(1 - \frac{u}{u_0}\right) dy. \tag{2.16}$$

In terms of the turbulent flow, a fully developed turbulent boundary layer profile is depicted in Fig 2.3, where u^+ is the flow velocity normalized by the friction velocity, $u_\tau = \sqrt{\tau_w/\varrho}$, and y^+ is the wall distance normalized by the viscous length scale, $\delta_\nu = \nu/u_\tau$.

According to [143, 147], the region close to the wall ($y^+ < 5$) is called the viscous sublayer. In this layer the momentum exchange in the wall-normal direction happens only due to viscous forces and turbulence is negligible. Therefore, the velocity increases with the wall distance. The normalized velocity follows

$$u^+ = y^+. \tag{2.17}$$

The region of $5 < y^+ < 30$ is called the transition region. Further away from the wall of $y^+ > 30$, the empirical log law holds for canonical flows, which is defined as

$$u^+ = \frac{1}{\kappa} \ln y^+ + B. \tag{2.18}$$

From experimental data, it is known that the von Kármán constant [180], κ, is generally given as 0.41 and the integration constant, B, is 5.2.

Boundary layers for temperature or species concentration can be defined in an analogous manner because of their similarity to flow boundary layers. With forced convection, such as the heat transfer through gas flow, the ratio of the velocity boundary layer, δ_b, to the thermal boundary layer, δ_T, can be characterized with the dimensionless number Pr,

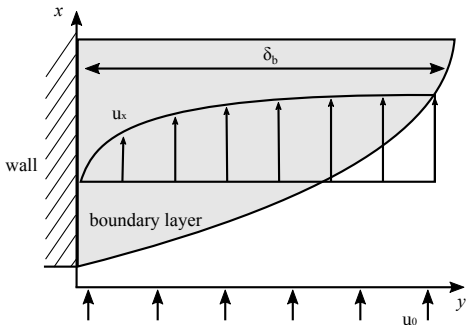

Figure 2.2. Laminar boundary layer development on a flat plate.

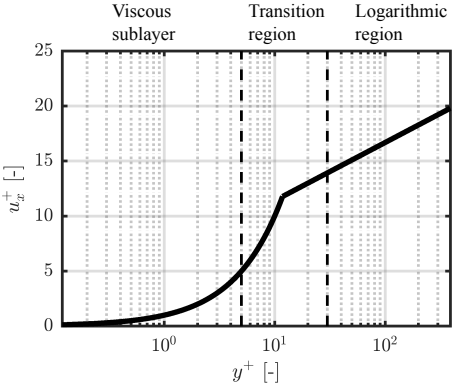

Figure 2.3. Representation of the different areas of a turbulent boundary layer in the semilogarithmic scale based on an image given in [143]. There is a distinction in the viscous sublayer, the transition region and the logarithmic region.

$$\frac{\delta_b}{\delta_T} \propto \mathrm{Pr}^{1/2}. \tag{2.19}$$

The Prandtl number for diatomic gases is in the order of 1 (for an ideal diatomic gas, Pr = 0.74), which is the reason why the thermal boundary layer and the flow boundary layer have approximately the same thickness [167].

2.2 Heat transfer mechanisms

As already indicated in Chapter 1, the enthalpy loss of the flame to the wall is a crucial factor in the consideration of the flame-wall interaction. Therefore, this section covers the basics of heat transfer, which can be distinguished by different heat transfer mechanisms. First, if there is heat transfer in an isotropic material, it is heat conduction. One-dimensional heat conduction is described by Fourier's Law [59],

$$\dot{q_\kappa} = -\lambda \frac{\partial T}{\partial x}. \tag{2.20}$$

The heat flux $\dot{q_\kappa}$ is proportional to the gradient of temperature and thermal conductivity λ.

Many problems of heat transfer, however, take place between a solid surface and a fluid flow, which is dominated by a convective heat transfer. This results in the already described formation of a thermal boundary layer on the solid surface. For the calculation of the underlying microscopic physical processes leading to the thermal boundary layer, a complete three-dimensional solution of the laws of mass, momentum and energy is usually required. Especially in the turbulent thermal boundary layer, the flow and temperature fields intensively interact with each other. The coherent vortical structures within the boundary layer have a significant influence on the heat transfer near the wall [173]. The solution of the turbulent heat transfer near the wall requires an enormous computational effort.

For global quantification of the turbulent heat transfer processes, the dimensionless Nusselt number is often used in practical engineering for a variety of configurations [59] as

$$\mathrm{Nu} = \frac{\alpha L}{\lambda} \tag{2.21}$$

where α represents the heat transfer coefficient and L is a characteristic length. The Nusselt number, Nu, represents the ratio between convective heat transfer and

heat conduction. Implementing Nu enables the estimation of the heat transfer in simple geometries with defined boundary conditions.

Governing heat transfer from a fluid to a wall or vice versa is also described by Fourier's Law, and is as follows,

$$\dot{q_{\mathrm{h}}} = -\alpha(T - T_{\mathrm{wall}}) \tag{2.22}$$

where $\dot{q_{\mathrm{h}}}$ is the heat flux, T and T_{wall} are the temperatures of the fluid and the wall, respectively, and α is the heat transfer coefficient of the fluid.

The heat transfer is influenced by a characteristic quantity of convection, and also determined by radiation. Thermal radiation is emitted by most kinds of materials, and depends on the temperature of the material as follows [16, 168],

$$\dot{q_{\mathrm{r}}} = \epsilon\sigma T^4 \tag{2.23}$$

where $\dot{q_{\mathrm{r}}}$ is the heat transfer by radiation, ϵ is the emissivity, σ is the Stefan-Boltzmann constant and T is the absolute temperature of the emitting body. If the surfaces are *grey*, as is often the case, their emissivity is less than 1. Heat transfer by radiation is a very complex phenomenon. By using Eq. (2.23) or similar equations, it is possible to resolve only few elementary issues, but it becomes nearly impossible to resolve complex cases. It is therefore necessary to apply experimental data or empirical computation methods derived from experimental surveys. In the configurations considered in this work, however, thermal radiation plays a subordinate role and is ignored.

2.3 Basic concepts of combustion

Combustion is an exothermic, self-sustaining chemical reaction of a fuel and an oxidizer. In practical combustion processes, fuels are mainly composed of hydrocarbons, while air serves as oxidizer. Globally, the hydrocarbons react with oxygen from the air to form carbon dioxide (CO_2) and water (H_2O). The various reactions during the process lead to the electronic excitation of molecules within the reaction zone, which in turn emit light when returning to their ground states (chemiluminescence). The reaction volume with emitting light, called *flame*, is the heat release zone. There, temperatures can reach up to 2200 K in atomospheric premixed methane/air flames with the initial temperature of 300 K [79]. The light emission can be utilized as a source for measurement techniques. The structure, shape, size and temperature of the flame can vary strongly the physicochemical processes within the reaction zone. These processes are mainly determined by the

combustion mode, which was already introduced, as premixed, non-premixed or partially-premixed.

The investigations in this work aim understanding temperature/ CO themochemical states during the FWI by using methane/air and DME/air premixed flames. Therefore, this section focuses on the formation and the oxidation path of CO and the structure of premixed flames.

2.3.1 Reaction kinetics

The following section provides the basic concepts of methane (CH_4) and DME (CH_3OCH_3) oxidation that can be found in various references [105, 177]. The global reactions for each fuel oxidation with the stoichiometric configuration are as follows,

$$CH_4 + 2O_2 \longrightarrow CO_2 + 2H_2O, \tag{2.24}$$

$$CH_3OCH_3 + 3O_2 \longrightarrow 2CO_2 + 3H_2O. \tag{2.25}$$

Equations. (2.24) and (2.25) describe the redistribution of C and H atoms during the oxidation process globally. It is assumed that all fuel and O_2 molecules react completely to form CO_2 and H_2O. The global description is not sufficient for the prediction of minor species such as CO. In reality, the oxidation processes are more complex and consists of a large number of elementary reactions which describe the reactive collisions of single molecules on the atomic level. Therefore, intermediate species are formed that are partially or totally consumed in the course of subsequent reactions. This point of view is especially important under FWI condition, as the enthalpy loss to the wall results in the breakup of certain reaction chains of elementary reactions. Reaction mechanisms including subsets of rate-limiting elementary reactions are used to simulate these complex chemical processes. The GRI mech 3.0 reaction mechanism [164] is widely applied to model the chemistry of the relatively simple molecules and is also applied to one-dimensional flame calculation for methane/air flame in this work (introduced in Section 4.3). For DME/air flames, the Zhao reaction mechanism [192] is applied.

The most dominant pathway for methane oxidation at 2200 K in a well-stirred reactor is [177]

$$CH_4 \xrightarrow{OH,H,O} CH_3 \xrightarrow{O} CH_2O \xrightarrow{OH,H,O} CHO \xrightarrow{H_2O,M,OH} CO \xrightarrow{OH,M,O} CO_2. \tag{2.26}$$

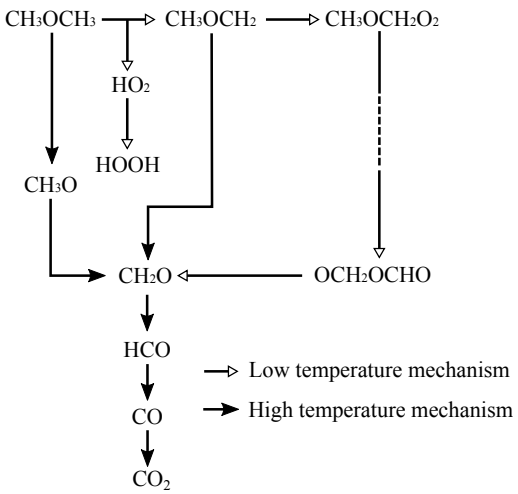

Figure 2.4. Schematic diagram for the overall reaction path of DME oxidation (based on an image given in [105]).

The pathway follows a successive dehydration of the CH_4 molecule by various radicals. During the breakup process, the hydroxyl radical (OH) also plays an important role. The OH radical, therefore, is a good indicator for the reaction processes in the flame, which will be discussed in Section 3.3.3 through Laser-Induced Fluorescence (LIF) of OH radicals.

In contrast to methane oxidation pathways, DME has both low temperature and high temperature reaction mechanisms. The detailed mechanisms of DME were developed and used to study the ignition and oxidation [86]. The overall reaction mechanism is shown in Fig. 2.4 [105]. The low temperature mechanism is dominant in the range of 600 - 850 K, whereas the high temperature mechanism is more active above 900 K.

In comparison to the corresponding methane/air flames, the formaldehyde (CH_2O) mole fraction is much higher in DME flames. The dissociation of methoxymethyl radicals (CH_3OCH_2) exists in DME flames, which is a very important channel in the high-temperature mechanism. It provides a major source of CH_2O via a channel that is not present in the methane oxidation mechanism. Therefore, this reaction channel can provide much higher mole fractions of CH_2O in DME flames. This is an advantage in terms of CH_2O-LIF for heat release rate imaging which is explained in Section 3.3.3.

2.3.2 Structure of premixed flames

The implementation of premixed combustion is a key strategy to reduce nitric oxides (NOx) and soot emissions of high temperature combustion systems. In premixed combustion, the fuel and oxidizer are perfectly mixed before being supplied to the combustion chamber. The state of the mixture can easily be characterized by the equivalence ratio, ϕ, which is described by the ratio of the actual fuel mole fraction to the stoichiometric mole fraction as

$$\phi = \frac{X_{\text{fuel}}/X_{\text{air}}}{X_{\text{fuel,st}}/X_{\text{air,st}}}. \tag{2.27}$$

For $\phi = 1$, $\phi > 1$ and $\phi < 1$, the mixture is referred as stoichiometric, rich and lean, respectively. The equivalence ratio is one of the major parameters in this work.

The mixture must be within the flammability limits to sustain a stable combustion reaction. For a methane/air mixture under atmospheric conditions, the flammable equivalence ratio ranges $\phi = 0.50$ - 1.68, whereas $\phi = 0.50$ - 5.30 for a DME/air mixutre [191].

One-dimensional laminar premixed flames can be calculated with numerical codes, such as Cantera [80], Chem1D [34] or CHEMKIN [35]. The use of detailed reaction mechanisms yields important quantities derived from the results. In this work, the following two numerically calculated reference flames are provided,

- an undisturbed, adiabatic freely-propagating flame,
- a premixed flame which contains an additional enthalpy defect representing the heat transfer to the wall.

The first case is solved using Cantera to provide the fundamental flame structure and also to simulate the reference flat flame which will be explained later in Section 5.1.1. The latter non-adiabatic case is solved using an in-house solver [193] which is introduced in Section 4.3 to simulate flames with flame-wall interaction. For the computations of methane/air and DME/air flames, the GRI-3.0 mechanism [164] and the mechanism of Zhao et al. [192] are used, respectively. Figure 2.5 shows the result of the simulation (Cantera) of a freely propagating, atmospheric, stoichiometric methane/air flame. On the left side the mole fractions of the main species as well as the intermediates, OH and CO, are shown. The chemical reaction takes place in the main reaction zone in the sub-mm-range. On the right side, the temperature profile and the definition of the laminar flame thickness, which is described below, are presented.

A flame front divides the combustion region into two characteristic states: the burned and the unburned states. In the course of chemical reactions, the flame front moves towards the unburned mixture, leaving products in the burned region. The reaction volume where combustion takes place is a very thin zone between the burned and the unburned mixture.

A characteristic flame thickness, called the "laminar flame thickness", δ_F, is determined as the "diffusive flame thickness" by Poinsot et al. [141] and is described as

$$\delta_F = \frac{\lambda_U}{\varrho_U c_p s_L} \tag{2.28}$$

where λ_U represents thermal conductivity and the subscript "U" denotes unburned gas. Hasse et al. [90] gave another expression as

$$\delta_F = \frac{T_{ad} - T_U}{\partial T / \partial y}_{max} \tag{2.29}$$

where T_{ad} represents the adiabatic flame temperature and T_U represents the unburned fresh gas temperature. The laminar flame thickness calculated by Eq. (2.29) is shown graphically in Fig. 2.5 (right). There are also other definitions which may provide a significantly different solution from that derived by this definition. Therefore, when comparing sizes normalized by the laminar flame thickness, particular attention must be paid to their definitions. The flame characteristic time for the chemistry, τ_c, is obtained by normalizing the flame thickness to the laminar flame speed, s_L,

$$\tau_c = \frac{\delta_F}{s_L}. \tag{2.30}$$

The flame front can be divided into three zones which are governed by different physical mechanisms. These zones are the preheat zone, the reaction zone and the oxidation zone [79]. In the preheat zone only slow low temperature reactions take place. The approaching mixture is continuously heated by thermal diffusion energy from the reaction zone. The physics are governed by the equilibrium of convective and diffusive transport processes. The thickness of the preheat zone is in the order of δ_F. Above 900 - 1000 K, chain branching reactions start [79]. These reactions are attributed to the beginning of the reaction zone. The reaction zone is characterized by high temperature chemistry where the fuel molecules are oxidized and many intermediate species like CO and OH are created. These intermediate species are important for experimental investigations of flames and can be detected by planar

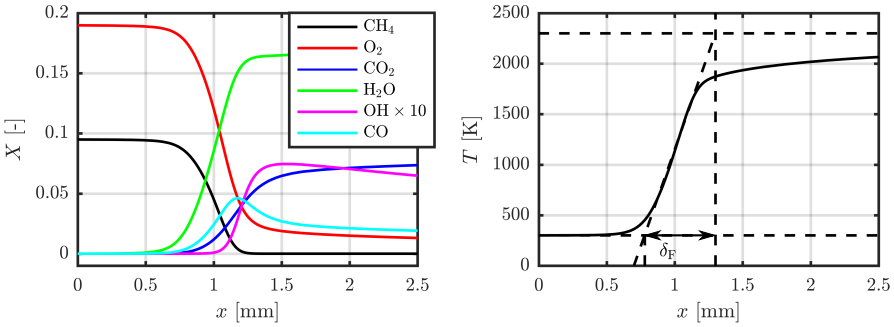

Figure 2.5. Mole fractions (left) and temperature (right) profiles of a simulated one-dimensional laminar flame ($\phi = 1$, initial temperature = 300 K). In the temperature profile, the definition of the laminar flame thickness is shown.

laser-induced fluorescence. The steepest gradient of the OH concentration can be used as flame front marker. In the reaction zone the heat release is at its maximum. The third zone is the oxidation zone, which is largely influenced by the oxidation of CO to CO_2.

For an adiabatic system the temperature continuously increases over the flame front until the adiabatic flame temperature, T_{ad}, is reached. The adiabatic temperature, T_{ad}, highly depends on the equivalence ratio, ϕ, as shown in Fig. 2.6 (left) estimated by one-dimensional flame calculation, Cantera.

The propagation speed of the flame front is controlled by the equilibrium between the heat release inside the flame front and the thermal diffusion to the unburned gas. The propagation speed of the flame front towards the unburned mixture is called the "laminar flame speed", s_L. In the case of a laminar flat flame, the approaching unburned mixture velocity equals the laminar flame speed. It is common practice to define the laminar flame speed based on the gas velocity of the unburned mixture. The laminar flame speed is influenced by several parameters, such as the initial temperature, the equivalence ratio, the fuel type and the pressure. Figure 2.6 (right) shows the laminar flame speed as a function of the equivalence ratio, ϕ, for unstretched methane/air and DME/air flames. For both fuels the peak flame speed is located in slightly the rich branch.

For laminar flames, the propagation speed depends on the thermal and chemical properties of the mixture. In contrast, the propagation speed of turbulent premixed flames depends significantly on the flow field. The turbulent flame front is wrin-

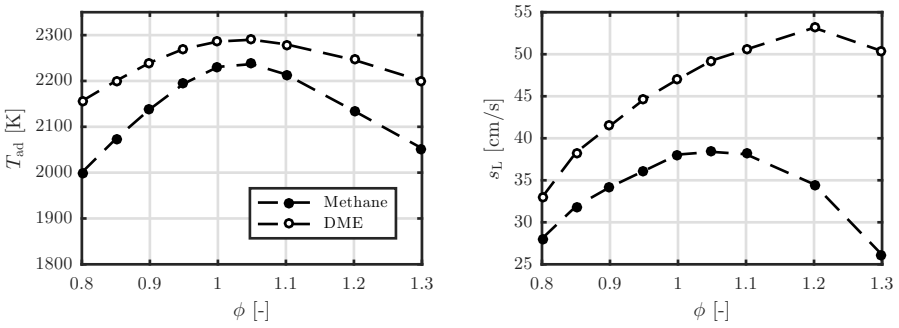

Figure 2.6. Dependency of adiabatic temperature T_{ad} (left) and laminar flame speed s_L (right) as a function of the equivalence ratio ϕ.

kled by the velocity fluctuations. The effective cross-sectional area of the turbulent flame, A_T, is significantly increased, which increases the flame propagation speed, called the "turbulent flame speed", s_T, as follows

$$\frac{s_T}{s_L} = \frac{A_T}{A_L}. \tag{2.31}$$

A classification of premixed flames under the influence of large or small scale turbulence can be introduced. This is useful to identify whether the structure of the flame front and its thermochemical state is altered by the penetration of turbulent eddies, or the flame front can still be treated as laminar. For this purpose, Damköhler proposed a scale comparison which is expressed as the Damköhler number [44],

$$\mathrm{Da} = \frac{\tau_t}{\tau_c} = \frac{(l_0/u')}{(\delta_F/s_L)}. \tag{2.32}$$

The Damköhler number, Da, is the ratio between the turbulent time scale of the flow field, τ_t, and the time scale of the chemical reaction, τ_c. Both can be calculated by a characteristic length and velocity scale (l_0/u') for the flow field and (δ_F/s_L) for the chemistry, respectively.

For an additional classification of turbulence-flame interaction, the Karlovitz number was introduced. By comparison between the laminar flame thickness, δ_F, and the dissipative Kolmogorov scales of the flow, l_k, the turbulent Karlovitz number, Ka, is defined as [185]

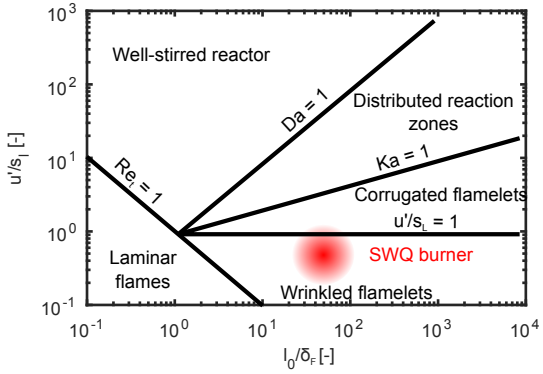

Figure 2.7. Borghi-Peters regime diagram for premixed flames [17]. In addition, the location of the measured turbulent flames in this work is shown (SWQ burner, colored red).

$$\mathrm{Ka} = \frac{\delta_\mathrm{F}^2}{l_\mathrm{k}^2}. \tag{2.33}$$

Using these equations, premixed flames can be categorized as shown in Fig. 2.7. The regime diagram is originally based on the work of Borghi and Casci [17] and later modified by Peters [138]. It classifies premixed flames based on the ratio of turbulent and chemistry length and time scales. In the double logarithmic representation of Fig. 2.7, the regime of purely laminar flames is distinguished from turbulent flames by the turbulent Reynolds number, $\mathrm{Re_t} = (u' l_0)/\nu = 1$, line. According to Peters, turbulent premixed flames can be classified into four different regimes.

In the region of $\mathrm{Ka} < 1$, the *flamelet* [1] regime is characterized by a very thin flame front compared to the smallest dissipation structures of the flow field. The turbulence can only kinematically wrinkle the flame front, thus the laminar structure of the flame is maintained. This thin flame regime can be further divided into wrinkled and corrugated flamelets. In the wrinkled flamelets regime, the flame front is merely stretched and wrinkled by velocity fluctuations that are smaller than the laminar flame speed ($u' < s_\mathrm{L}$). The corrugated flamelet regime can be characterized by the turbulent fluctuations exceeding the laminar flame speed ($u' > s_\mathrm{L}$).

[1] A laminar flamelet concept covers a regime in turbulent combustion where chemistry is faster than transport processes such that reactions occur in thin layers (so-called *flamelet*) [138]

In the corrugated flamelet regime, velocity fluctuations can partially influence the flame front and modify its topology. The transition from the corrugated flamelets regime to the distributed reaction zones is described by the straight line where Ka = 1. This line describes the equality of size of the Kolmogorov scale and the flame thickness. Ka > 1 denotes the regime where the smallest vortices can penetrate the preheat zone of the flame. Thus, it is dominated by small scale turbulence. For the region above the line Da = 1, the turbulent vortices broaden the flames and no clear flame front can be found.

The classifications of the burner configurations used in this work are represented by the circular-red area in Fig. 2.7. A detailed description of the burner and its operating conditions will be given in Section 4.1.

2.4 Flame-wall interaction

As mentioned in Chapter 1, flame-wall interaction (FWI) is a coupling process where the flame and wall interact with each other. FWI causes significant wall heat fluxes which lead to flame quenching at the wall. Flames near walls impact the flow boundary layer, which also affect chemical reactions and flame propagation. Due to the complexity of practical devices, FWI has been investigated in several canonical configurations. The following chapters classify and describe these approaches.

2.4.1 Phenomenological description of flame-wall interaction

The two key thermal properties that describe FWI are the position of the flame and the heat flux to the wall. The temporal evolution of both quantities is shown in Fig. 2.8 during FWI of a laminar flame. The result shown here were derived from one-dimensional DNS calculation by Poinsot et al. [141]. The position of the flame front corresponds to an isotherm at $0.9 \cdot T_{\mathrm{ad}}$. If the flame burns far away from the wall, the wall heat flux is practically non-existent. When the flame comes close to the wall, a large temperature gradient occurs near the cold wall. As a result, the wall heat flux increases intensively and the flame propagation is slowed down by slower chemical reactions. At some point, the propagation of the flame stops and the heat flux becomes maximum. At this point, the quenching time of the flame, t_{Q}, and the quenching distance, δ_{Q}, are usually defined. In Fig. 2.8, the quenching distance and the wall heat flux are non-dimensionalized with definitions introduced below.

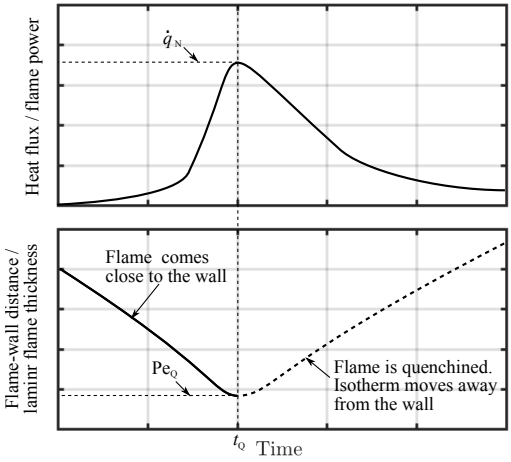

Figure 2.8. Numerical results for a laminar flame-wall interaction based on [141]. The normalized wall heat flux, $\dot{q}_N$, and the position of the flame (represented by an isotherm at $0.9 \cdot T_{ad}$) are shown.

For better comparability of different investigations, the quenching distance, δ_Q, is usually non-dimensionalized with the flame thickness, δ_F, as the quenching Peclet number, Pe_Q,

$$Pe_Q = \frac{\delta_Q}{\delta_F}. \tag{2.34}$$

Similarly, the instantaneous heat flux, $\dot{q}$, is normalized by the laminar characteristic heat release, "flame power", [141] as

$$\dot{q}_N = \frac{\dot{q}}{(\varrho_U Y_{Fuel} s_L \Delta H)} \tag{2.35}$$

where the quantity Y_{Fuel} is the fuel mass fraction in the unburned gas mixture and ΔH is the enthalpy change. For lean flames the denominator of Eq. (2.35) can be approximated with $\varrho_U Y_{Fuel} s_L \Delta H = \varrho_U c_p s_L (T_{ad} - T_u)$.

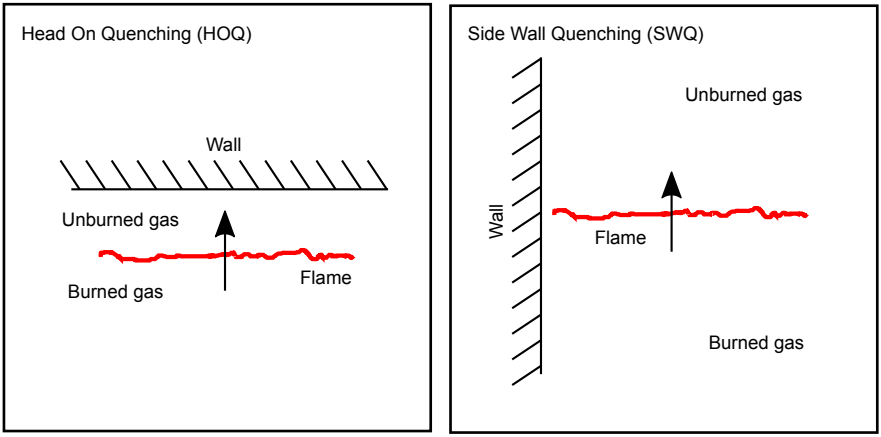

Figure 2.9. Typical extreme cases of quenching for premixed flames.

2.4.2 Types of flame-wall interactions

Flame quenching can be divided into its extreme cases, namely, head-on quenching (HOQ) and side-wall quenching (SWQ). Figure 2.9 shows a schematic of both configurations. HOQ is always a transient event initiated within premixed mixtures, generally by an electric or laser spark. During HOQ, a flame propagates towards the wall. The flame front and the wall surface are parallel. In laminar flows, the flame propagates at constant speed until the flame approaches the wall. It is followed by flame quenching. For turbulent flows, Poinsot et al. [141] gave distinction to the expression "influence zone". In this zone heat losses to the wall start to rise. Accordingly, instantaneous flame power and consumption speed of the flame decrease. When local heat release rates decrease to the level of wall heat losses, the flame cannot maintain any further propagation and is thermally quenched. The quenching zone is characterized by low temperatures. For HOQ, the corresponding quenching Peclet number is reported by several sources to be in the order of $Pe_Q = 3.5 \pm 1$ for methane/air, ethylene/air and propane/air flames [93, 187].

Side-wall quenching (SWQ) occurs when a flame propagates in the direction parallel to a wall, which is investigated in this work. Even in the simplest stagnant case, SWQ is a two-dimensional problem. In contrast to HOQ, SWQ occurs only in the part of the flame that is near the wall. The quenching Peclet number is in the order of $Pe_Q = 7$ [141], which is larger compared to the HOQ configuration and leads to less heat loss.

3 Methodology on laser-based diagnostics

Laser-based measurement techniques have represented the state of the art in modern experimental combustion research for many years. The advantages of laser diagnostics open up a variety of new methods to investigate combustion processes. All laser diagnostic techniques are based on the physical interaction between light and matter. This chapter gives an introduction to the basics of these interactions, which are relevant to the understanding of this work. A detailed derivation of the underlying physics is found in relevant literature [5, 91].

3.1 Fundamentals on quantum mechanics

The fundamentals of the relevant light-matter interactions can be explained either with a classical or a quantum-mechanical approach. Both methods lead in large part to the same results, but differ substantially in their basic ideas. In the following section, both approaches will be explained and their most important results will be also presented.

3.1.1 Classical description

Understanding the light-matter interactions requires a physical model for the description of light as well as the knowledge of the structure of matter. This can be done by a classical approach using the well-known Maxwell equations [128]. The description of light, or general electromagnetic radiation, is based on the idea of a wave as

$$\nabla^2 \vec{E} - \frac{n^2}{c^2} \frac{\partial^2 \vec{E}}{\partial^2 t} = 0. \tag{3.1}$$

Here, n stands for a refraction factor, c for the speed of light and $\vec{E}$ for the electric field strength. The wave equation is a linear, partial differential equation of second order. Assuming the special case of a plane, harmonic, electromagnetic wave whose

field size propagates only in one spatial direction (x-axis), then a solution can be given as

$$E = E_0 \exp\{i(\omega t - kx)\}. \tag{3.2}$$

Here, E_0 describes the amplitude and k the wave vector, which is defined as the ratio of angular velocity, ω, to the speed of light, c, as

$$k = \frac{\omega}{c} = \frac{2\pi}{\lambda}. \tag{3.3}$$

With the set of equations from Maxwell, the electrodynamic properties of light can be predicted. The description of Maxwell equations is based on a continuous and macroscopic approach where light can theoretically occupy all energy states [96]. In the classical description, matter is considered to be a collection of vibratory electric dipoles. The idea comes from the fact that an external electric field, such as light, leads to an oscillating force on the electrons of molecules or atoms. This stimulates the electrons to vibrate with the frequency of the incident light. The influence of the electric field on the much heavier atomic nucleus can be neglected here. The shift of the moving electrons causes the generation of microscopic dipole moments. These moments result in a macroscopic polarization, $\vec{P}$, of matter. In electrodynamics, the following linear relationship between the electric field strength, $\vec{E}$, of the light and the polarization applies as follows,

$$\vec{P} = \chi \epsilon_0 \vec{E} \tag{3.4}$$

where the linearity constant, χ, is a complex quantity and is called a susceptibility. The χ is a material property indicating the ability to electrically polarize at an external electric field. The real part of χ corresponds to the dispersion and the imaginary part corresponds to the absorption of the light. The susceptibility is frequency-dependent and usually shows one or more resonances. These resonances correspond to the absorption lines of the polarized medium. The quantity ϵ_0 is the electric field constant in a vacuum. The determination of χ can be done in classical physics by means of the Lorentz-Lorenz model [96].

3.1.2 Quantum mechanical description

On the basis of the classical wave theory, many optical effects such as refraction, dispersion and scattering can be explained. Some of the common measurement techniques in use can also be understood by classical wave theory. However, it quickly became apparent that fundamental observations of the light-matter interaction cannot be explained by the Maxwell equations. These contradictions led to a completely new way of looking at microscopic physical processes with the development of quantum mechanics. Based on the ideas of Niels Bohr on atomic structure [15] and Max Planck on the properties of light [140], processes such as the photoelectric effect can now be conclusively explained.

Contrary to the classical description, according to Planck's ideas, light can have both the classical properties of a wave and of a particle. This description, called wave-particle dualism, is elementary for the quantum-mechanical interaction of light and matter.

Light particles are referred to as photons, which have no mass in the stationary state. The energy of a photon, E, is linearly linked to the frequency, ν, of the light by the Planck's constant, h, ($h = 6.63 \cdot 10^{-34}\mathrm{J} \cdot \mathrm{s}$) as follows,

$$E = h \cdot \nu. \tag{3.5}$$

The photon energy equation represents a connection between the wave and quantum-mechanical representation of light. In contrast to the classical wave theory, light can exist only at discrete energy values.

According to the idea of quantum mechanics, not only the energy of light, but also of any matter, such as, atoms or molecules is quantized in the form of an electromagnetic field. This finding was described by Niels Bohr with a quantum-mechanical model of the hydrogen atom. The angular momentum of an electron orbiting around a nucleus is quantized as discrete electron orbits with quantized energy levels. If the orbits of both an electron and the quantum state change in vacuum, it always occurs with the emission of light.

In general, the energy state of a quantum-mechanical system can be determined by the time-independent Schrödinger equation [156]. As a solution to this differential equation, the wave function, ψ, is obtained, which is assigned to a discrete energy value of the system. The size of the wave function has no direct physical meaning. However, the magnitude square, $|\psi|^2$, can be interpreted as the probability of the existence of a particle in a given control volume. Depending on the complexity of the system under consideration, all achievable energy levels can be described in this way by one or more quantum numbers. For simple systems like

the hydrogen atom, an analytical solution of the Schrödinger equation can be derived. However, as the structures of the atoms or molecules become more complex, simplifications are required to solve the equation.

Table 3.1. Selected quantum numbers for a molecule [5].

Symbol	Quantum number	Value
v	Vibrational quantum number	v = 0,1,2,...
J	Rotational quantum number	J = 0,1,2,...
M	Magnetic quantum number	$M = J, (J\text{-}1), \ldots, -J$
$\vec{S}$	Electron spin	$\vec{S}$ = 0,1/2,1,3/2,...

The energy states of the molecules are described with a set of quantum numbers (see Table 3.1) [5]. For further consideration, the most important quantum numbers are the vibrational quantum number, v, which indicates the vibrational level of an electronic state, and the rotation quantum number, J, which denotes the rotation of a molecule in a vibration state. The common notation for the electronic states of diatomic molecules is as follows [5],

$$\Xi^{2S+1}L^{sym}. \tag{3.6}$$

In Eq. (3.6), Ξ stands for the electronic energy state of the molecule. It is denoted by X for the ground state and for the excited states by A, B, ... in alphabetical order. The term $2S + 1$ stands for the spin multiplicity of the outer electrons. The values of the the spin multiplicity are 1, 2, 3,..., which corresponds to a singlets, doublets, triplets,... states. L denotes the orbital form of the molecules and is named with the Greek capital letters Σ, Π, Δ,.... The addition sym, which indicates the symmetry with respect to the kernel plane, appears only in the Σ-state and is either + with the same parity of the atomic states or - with unequal parity.

For the molecules with two or more atoms relevant for this work, additional classification can be derived from the vibration of the nuclei against each other and the rotation of the nuclei structure. The total energy, E, is divided into an electronic, E_e, vibrational, E_v, and rotational part, E_r, as

$$E = E_\mathrm{e} + E_\mathrm{v} + E_\mathrm{r}. \tag{3.7}$$

A transition between two energy levels requires a difference of energy, ΔE. This difference of energy is also composed of the terms for the individual transitions in Eq.(3.7) as

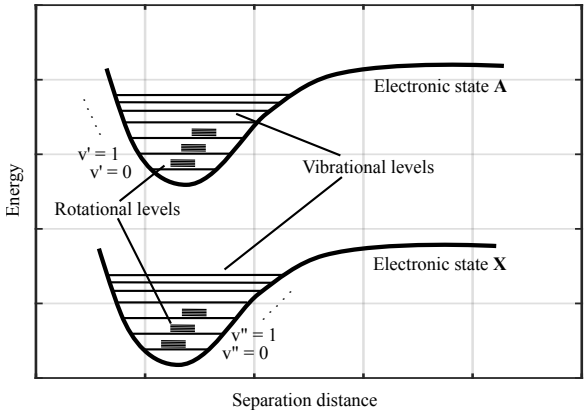

Figure 3.1. Schematic representation of the different energy levels of a diatomic molecule based on an image given in [110].

$$\Delta E = \Delta E_{\mathrm{e}} + \Delta E_{\mathrm{v}} + \Delta E_{\mathrm{r}}. \tag{3.8}$$

The terms for the electronic, vibrational and rotational transition here are clearly distinguished by their order of magnitudes and are divided as follows:

$$\Delta E_{\mathrm{e}} > \Delta E_{\mathrm{v}} > \Delta E_{\mathrm{r}}. \tag{3.9}$$

This division of the different energy levels can be clarified by means of the configuration coordinate model. Figure 3.1 shows this model for a diatomic molecule. The distance between the two atomic nuclei is plotted against the energy of the entire system. The two potential curves X and A represent the energy states in the electronic ground and excited states, respectively. By adding vibrational and rotational levels, a further splitting of the states takes place.

3.1.3 Elementary processes of light-matter interaction

In spectroscopy, three resonant interactions between light and matter play a major role, i.e., the absorption, the stimulated emission and the spontaneous emission.

They are called resonant processes because the energy of the interacting photon, E_{Photon} $(= \mathrm{h} \cdot \nu)$, matches the energy difference $E_1 - E_0$ of the transition. The

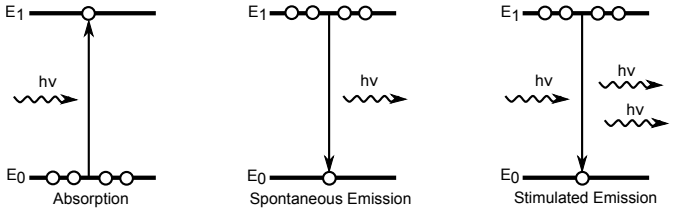

Figure 3.2. Sketches of the different resonant interaction mechanisms between a photon and a quantum-mechanically described particle.

magnitude, E_0, corresponds to the energy of the ground state and E_1 to that of the excited state. As shown in Fig. 3.2, these processes are described in a two-level system.

Absorption: If a molecule (or an atom) is in the ground state, E_0, an incoming photon can convert the molecule into an excited state, E_1. The incoming photon is annihilated during this process. The absorption corresponds to a resonance of the susceptibility, χ (Eq. (3.4)), at the wavelength of light.

Spontaneous emission: If a molecule (or an atom) is already in the excited state, E_1, it remains there with a certain lifetime before it falls back to the more energy-favorable ground state, E_0. This process is called spontaneous emission. A photon with the energy, $E_{\text{Photon}} = E_1 - E_0$, is emitted.

Stimulated emission: If an already excited molecule or atom is in the E_1 state and the energy of an absorbed photon corresponds to the energy, $E_1 - E_0$, stimulated emission may occur. In addition to the incident photon, another photon of the same wavelength, polarization direction and phase angle is emitted. This property, referred to as coherence, is an elementary prerequisite for the functioning of a laser.

In addition to both spontaneous and stimulated emission, there are a number of non-radiative competitive processes. These have an influence on the emission intensity as well as on the lifetime of the excited state. Since the measured variables in many laser-based measurement methods are related to the fluorescence emission, such processes must be taken into account. An overview of the most important competing processes in this work can be found in Section 3.3.4.

3.1.4 Non-linear processes in light-matter interaction

The field strengths produced by pulsed laser systems can become so great that the linear relationship between the electric field $\vec{E}$ and the polarization $\vec{P}$ shown in Eq. (3.4) is no longer able to correctly describe all occurring phenomena. The resulting non-linearity can only be taken into account by terms of higher order, which can be found in the power series evolution of the polarization,

$$\begin{aligned}\vec{P} &= \epsilon_0 \sum_n \chi^{(n)} \vec{E}^n \\ &= \epsilon_0 \chi^{(1)} \vec{E} + \epsilon_0 (\chi^{(2)} \vec{E}) \vec{E} + \epsilon_0 ((\chi^{(3)} \vec{E}) \vec{E}) \vec{E} + \cdots .\end{aligned} \tag{3.10}$$

The terms $\chi^{(2)}$ and $\chi^{(3)}$ are called second and third order susceptibilities. As the order increases, the values of susceptibilities become smaller and smaller, thus reducing their influence.

The consequence of such additional susceptibilities is the emission with higher or lower wavelengths than the incident emission. This effect is applied in a series of laser-optical methods. In the following part, a brief overview of the non-linear interactions relevant in this work is given.

Frequency doubling: Frequency doubling plays a decisive role in the extension of the spectral emission range of lasers [131]. This results in a doubling of the laser frequency or a halving of the wavelength. Thus, for example, the working range of a Nd:YAG laser extends from the infrared to the visible green and even to the UV range.

This effect is based on the simultaneous excitation of a non-centrosymmetric crystal with two monochromatic waves of the same frequency, polarization and direction. At sufficiently high electric field strengths with the media where the second-order susceptibility can exist, the term with the susceptibility, $\chi^{(2)}$, becomes more important. This results in producing a further laser beam with twice the frequency.

Two-photon absorption: Through two-photon absorption, transitions with energy differences larger than that of the incident single photon can be achieved [131]. At sufficiently high laser power, two photons whose energy sum corresponds to the excitation energy are simultaneously absorbed. Thus, transitions whose energy difference is so high that they are in the vacuum UV range ($\lambda < 200$ nm) can be realized.

Coherent anti-Stokes Raman scattering: Coherent anti-Stokes Raman scattering (CARS) combines three lasers of at least two different wavelengths. The detailed description of the process is discussed in Section 3.3.2.

3.2 Statistical thermodynamics and the distribution function

Statistical thermodynamics bridges the gap between the quantum-mechanical properties of molecules and the macroscopic phenomenological laws of thermodynamics. The concept of statistical thermodynamics is based on the distribution function.

Assuming that all energy states (electron configuration, vibration, rotation, coupling mechanisms) of an atom or a molecule are equally probable, in the case of thermodynamic equilibrium, the population distribution depends solely on the temperature. This relationship is described by the Boltzmann distribution function [129],

$$N_i = N \frac{g_i e^{-E_i/(k_\mathrm{B} T)}}{\sum_j g_j e^{-E_j/(k_B T)}}. \tag{3.11}$$

N stands for the number of particles, N_i for the number of particles in the E_i energy state, g_i for the degeneracy factor of this state and k_B for the Boltzmann constant. The molecules of a system constantly exchange energy through collisions, but the distribution of occupation across all states remains almost constant. To determine the temperature, the state sums of all energy states and their degeneracy factors are not necessary to be known. In principle, it is sufficient to know the population densities of two energy levels i and j. This results from Eq. (3.11) in the following relationship for the temperature

$$T = \frac{E_j - E_i}{k_\mathrm{B} \cdot \ln(N_i/N_j)}. \tag{3.12}$$

The Boltzmann distribution is thus a connection between the quantum-mechanical properties and thermodynamic parameters of a system.

3.3 Laser diagnostics in combustion

There are a variety of laser diagnostics techniques relevant to combustion. These techniques are mostly based on the light-matter interactions described in the previous section. The following section explains the basics of the measurement techniques used in this work.

3.3.1 Particle Image Velocimetry (PIV)

PIV is an optical measurement technique for the determination of fluid velocities and it is based on the Mie-scattering of light from particles seeded to the investigated flow. A detailed description of the measurement technique can be found in [148]. A schematic PIV setup is shown in Fig. 3.3.

In order to achieve good followability of the particles to the flow, small particles have an advantage. This results in a conflict of the ideal size of particles, since the intensity of the light scattered by the particle decreases with the size of the particles. Particles of the order of several μm are generally a good compromise here. The reason is that, according to the Mie-theory, the intensity, I, of the light scattered by the particle depends on the ratio of the particle size, d_p, to the wavelength of the light, λ, [148] as

$$\begin{aligned} \frac{d_\mathrm{p}}{\lambda} \ll 1 \; : \; I \propto \left(\frac{d_\mathrm{p}}{\lambda}\right)^6 \\ \frac{d_\mathrm{p}}{\lambda} \gg 1 \; : \; I \propto \left(\frac{d_\mathrm{p}}{\lambda}\right)^2 . \end{aligned} \tag{3.13}$$

Furthermore, to improve the followability of the particle, a small difference in density between the particle and fluid is desirable. In non-reacting flows, silicon oil droplets are often used because of their low density and small diameter compared to those of solid particles [98]. For measurements in flames, ceramic particles, such as aluminum oxide (Al_2O_3), titanium oxide (TiO_2) or boron nitride (BN) are often used [139, 169, 170].

In PIV, the displacement of particle ensembles between two time points can be determined by comparing two sequentially recorded images [148]. With known optical magnification and time difference, Δt, between two images, the velocity vectors result in

$$\vec{u} = \frac{\Delta \vec{r}}{\Delta t} = \frac{\vec{r}(t+\Delta t) - \vec{r}(t)}{\Delta t} \tag{3.14}$$

with the spatial displacement, $\Delta\vec{r}$, between the two images. The displacement is determined by the discrete cross-correlation of two images. For two-dimensional PIV in the x-y plane, the cross-correlation, R, is represented as

$$R(\Delta x, \Delta y) = \Sigma_i \Sigma_j I_1(i,j) I_2(i+\Delta x, j+\Delta y) \tag{3.15}$$

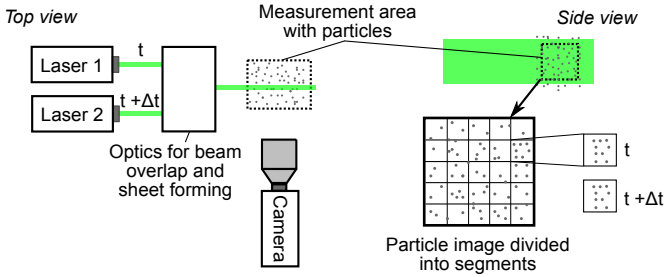

Figure 3.3. Principle of Particle Image Velocimetry (PIV).

with the intensity, I, of the pixel with the coordinates (i, j). Values of $(\Delta x, \Delta y)$ with the maximum of R then correspond to the displacement vector.

To record two images sequentially, the measurement plane is illuminated twice in a short duration with a laser-light sheet. In practice, this is done by a double-pulse laser. The images are captured with a sufficiently fast operated camera. For the determination of velocity fields, captured images are divided into subgroups (interrogation areas). The parameters of the experiment should be chosen so that in each subgroup sufficient particles are present and can be imaged to reliably determine the cross-correlation. However, the subgroups should be small enough to resolve the characteristic structures of the flow.

In the configuration used in this work, two speed components in the measurement plane are determined, but the technique can also be extended to three components (stereo PIV) and a three-dimensional volume (tomographic PIV).

3.3.2 Coherent anti-Stokes Raman Spectroscopy (CARS)

The CARS technique is one of the most accurate methods for determining gas temperatures in combustion environments. CARS is a non-linear diagnostic technique that relies on anti-Stokes Raman scattering of the target molecule using three incident waves. The fundamentals of CARS in this work are based on the study by Eckbreth [57], where a detailed explanation is given, as well as helpful discussion in [106]. In the following description, only the essential steps and results for the understanding of the CARS method are introduced.

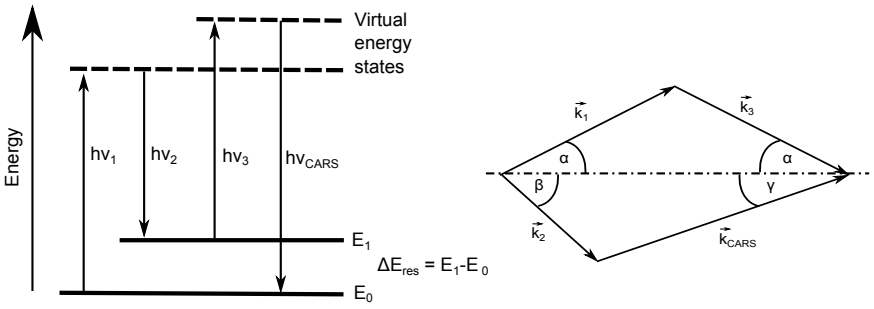

Figure 3.4. Schematic diagram of the energy transitions of CARS-process (left) and CARS wave vector diagram (right).

3.3.2.1 Fundamentals of CARS

The CARS process is referred to as a four-wave interaction process. The quantum-mechanical scheme of this process is shown in Fig. 3.4 (left). In the first step, a molecule (or atom) is excited to a virtual energy state by means of a pump laser beam with energy $h\nu_1$. If a Stokes beam of energy $h\nu_2$ interacts with the molecule at the same time as the pump beam, a real energy state E_1 can be achieved. For this process to occur, it is necessary that the energy identity, $\Delta E = h\nu_1 - h\nu_2$, corresponds to that of a molecule-specific Raman-allowed transition. Usually, these are vibrational or rotational transitions in CARS. As a result, the molecule is in a simultaneous superposition of a virtual and real state, which produces a coherent polarization of the excited molecule. With a further photon of the probe beam of energy $h\nu_3$, the molecule can be brought to a virtual state again. This virtual state is not stable and the molecule instantaneously returns to the ground state, with emitting a photon.

Because the CARS process is an elastic scattering where the initial and final states are identical (see Fig. 3.4 (right)), conservation of both energy and momentum is valid. The energy conservation is represented by Eq. (3.16) and the conservation of momentum by Eq. (3.17).

$$h\nu_1 - h\nu_2 + h\nu_3 - h\nu_{CARS} = 0 \tag{3.16}$$

$$\vec{k}_1 - \vec{k}_2 + \vec{k}_3 - \vec{k}_{CARS} = 0 \tag{3.17}$$

Equation (3.17) is well known from literature as the phase-matching condition. Therefore, the CARS signal is very directional and well collimated along the direction that satisfies the condition of phase-matching. The two geometries that are mostly implemented for CARS spectroscopy in a gas phase are: (a) collinear CARS where all of the input laser light propagates along a line and the phase-matching condition is automatically met along the same line and in the forward direction, and (b) BOXCARS [56] where the input beams are illuminated in a cross-beam configuration such that the three beams overlap only in the probe volume.

As already described in Section 3.1.4, the susceptibility in non-linear optical processes have higher-order terms. The decisive term for the CARS process is the susceptibility of the third order. It can be deduced (see [106]) that the intensity of the CARS signal depends to a large degree on the phase matching of the wave vectors $\vec{k}$. In the collinear CARS implementation, the CARS pump, Stokes and probe beams are not spatially separated. Without a significant refractive index change, linear alignment of the beams can keep an optimal arrangement. However, if there is the large refractive index change, which often occurs during FWI, the alignment is no longer optimal. Even a deviation of 0.3° leads to a signal loss of about 50 % [56]. Another disadvantage of the collinear CARS implementation is a poor spatial resolution of the measure system in the beam-wise direction. For this reason, the BOXCARS arrangement is typically chosen and is also used in this work. In this arrangement, shown in Fig. 3.4 (right), the pump, Stokes and probe beams are spatially separated. All beams can intersect at certain angles without violating the phase matching. This arrangement guarantees a short interaction length with high spatial resolution.

Because the energy difference, $h\nu_{CARS}$, is greater than the transition by the difference $h\nu_3$ - $h\nu_2$, the CARS signal is shifted to shorter wavelengths, i.e. anti-Stokes-shifted with respect to the pump laser. Since the CARS signal depends on the number density of eigenstate squared of the molecule, it is thus possible to deduce the proportion of molecules in this population state. According to Eq. (3.12), the population density of at least two levels is necessary to determine the temperature. This could be done by tuning (scanning) the Stokes laser frequency to another transition. However, this time-consuming process is usually unsuitable for combustion diagnostics, since averaged values would be measured over a long period of time. For this reason, the Stokes laser is often not monochromatic, but has a certain spectral bandwidth. In the case of the nitrogen molecule (N_2) used in this work, the bandwidth of the laser is approximately 6 nm and is often used for measurement during combustion. Thus, the energy states of the first three vibration levels of the

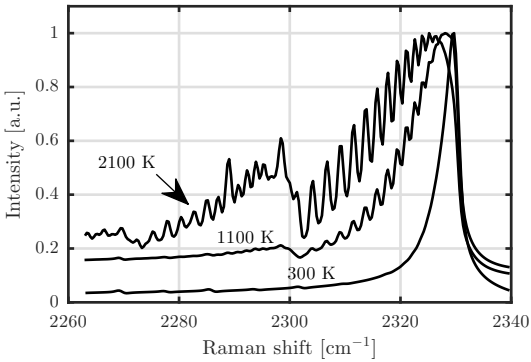

Figure 3.5. Three measured normalized CARS spectra of the N_2 molecule at $T = 300$, 1100 and 2100 K.

N_2 molecule can be excited simultaneously. An example of a measured CARS spectrum at different temperatures is shown in Fig. 3.5. For the N_2-CARS spectrum, it can be seen that only the first vibration level is excited at room temperature (Raman shift at 2330 cm^{-1}). From temperatures of about 1000 K, further rotation and the second vibration levels (2298 cm^{-1}) are excited. At adiabatic combustion temperatures above 2000 K, the third level of vibration of the N_2 molecule is also excited and it is clearly visible in the spectrum (2289 cm^{-1}).

3.3.2.2 Intensity of CARS signal

The intensity of the CARS signal depends linearly on the intensities of the three exciting laser beams $I(h\nu_i)$ as well as quadratically on the interaction length l [106],

$$I_{\mathrm{CARS}} \propto I(h\nu_1)I(h\nu_2)I(h\nu_3)l^2\left|\chi^{(3)}\right|^2. \tag{3.18}$$

As discussed in the previous section, the quadratic dependence on the interaction length l requires an optimal alignment of the CARS pump, Stokes and probe beams.

Furthermore, the third-order susceptibility has a quadratic influence on the signal intensity, which is equivalent to the particle density of the target molecule. In the case of the CARS process, the derivation of this susceptibility is made up of different terms [106], which is briefly discussed further in the next section.

3.3.2.3 Influence of susceptibility

The derivation of the susceptibilities of the third order, $\chi^{(3)}$, can be done both classically [48] and quantum mechanically [55].

For gas mixtures, a non-resonant component of the susceptibility, χ_{NR}, has to be considered in addition to the resonant component, χ_{CARS}. The non-resonant component, χ_{NR}, is considered to be a frequency independent real constant as

$$\begin{aligned}\chi^{(3)} &= \sum_k (\chi_{\mathrm{CARS}})_k + \chi_{\mathrm{NR}} \\ &= \sum_k (\chi^{\mathrm{Re}}_{\mathrm{CARS}} + \chi^{\mathrm{Im}}_{\mathrm{CARS}})_k + \chi_{\mathrm{NR}} \\ &= \sum_k (\chi^{\mathrm{Re}}_{\mathrm{CARS}})_k + \chi_{\mathrm{NR}} + \sum_k (\chi^{\mathrm{Im}}_{\mathrm{CARS}})_k,\end{aligned} \tag{3.19}$$

where k represents the wave number. In the case of broadband CARS, the purely non-resonant spectrum is an image of the spectral profile of the Stokes laser. Here, $\chi^{\mathrm{Re}}_{\mathrm{CARS}}$ and $\chi^{\mathrm{Im}}_{\mathrm{CARS}}$ can be called the dispersive and the resonant part of the CARS susceptibility, respectively. The summation over k considers all Raman-resonant transitions. The formation of the square of sums according to Eq. (3.18) leads to

$$\begin{aligned}|\chi^{(3)}|^2 &= |\sum_k (\chi^{\mathrm{Re}}_{\mathrm{CARS}})_k + \chi_{\mathrm{NR}} + \sum_k (\chi^{\mathrm{Im}}_{\mathrm{CARS}})_k|^2 \\ &= |\sum_k (\chi^{\mathrm{Re}}_{\mathrm{CARS}})_k + \chi_{\mathrm{NR}}|^2 + |\sum_k (\chi^{\mathrm{Im}}_{\mathrm{CARS}})_k|^2 \\ &= |\sum_k (\chi^{\mathrm{Re}}_{\mathrm{CARS}})_k|^2 + |\sum_k (\chi^{\mathrm{Im}}_{\mathrm{CARS}})_k|^2 + |\chi_{\mathrm{NR}}|^2 + 2\chi_{\mathrm{NR}} \sum_k (\chi^{\mathrm{Re}}_{\mathrm{CARS}})_k.\end{aligned} \tag{3.20}$$

Here, the first term on the right side stands for the dispersive component, the second for the resonant component, the third for the non-resonant background signal and the fourth for a mixed term. The non-resonant background signal must be taken into account when calculating theoretical spectra.

3.3.2.4 CARS thermometry

Temperature measurement based on the CARS method relies on the fact that the equilibrium population distribution among different quantum-mechanical states in a molecule are governed by the Boltzmann distribution function (Eq. (3.11)).

The temperature is extracted directly from the frequency-domain CARS data of vibrational or rotational lines. In fuel/air reacting flows, probing N_2 for thermometry has advantages because N_2 is present at high concentrations throughout the reaction zone. For that reason, nanosecond (ns)-ro-vibrational CARS thermometry based on N_2 is applied in this work. A major drawback of ns-CARS is the interference of the non-resonant background signal with the resonant CARS signal. Various polarization schemes can be used to reduce the non-resonant signal [58]. Interference of the non-resonant signal with the resonant CARS signal is the most pronounced issue when the pump, Stokes and probe beams are overlapped temporally. However, this condition is difficult to avoid in the ns-regime. Therefore, the contribution of the non-resonant signal has limited the applicability, sensitivity and accuracy of ns-CARS.

3.3.3 Laser-Induced Fluorescence (LIF)

In the field of combustion diagnostics, laser-induced fluorescence (LIF) is a widely used technique to gain information about the thermochemical state of a flame within a measurement volume. The most prominent application, which is also utilized within this work, is the observation of the flame front position by imaging the concentration of the hydroxyl radical (OH).

LIF is a technique capable to trace the existence of minor diatomic species within a reacting system such as OH, CO, NO and CH. However, LIF can also be applied to atoms or larger molecules such as acetone or toluene. In LIF, the wavelength of the exciting laser is tuned to a specific absorption line of the target molecule. The molecule is thereby excited at a higher electronic state. When the molecule returns to its ground state, it emits fluorescence photons which are then collected by an optical detector, such as a photomultiplier or a camera. The effective lifetime of the excited states for minor species is only a few nanoseconds. Thus, in terms of turbulent time scales, the fluorescence process can be assumed to be instantaneous.

For most molecules of interest such as the OH radical, a single photon in the ultra-violet spectrum (UV) is sufficient for excitation. However, in the case of some other molecules, for example CO, single photon excitation is impractical for the investigation of atmospheric flames. A solution is two-photon LIF which excites the molecule by the simultaneous absorption of two photons with half of the required energy. In the configuration used in this work, point-wise LIF (zero-dimensional) and planar LIF (called PLIF, two-dimensional) are applied, but the technique can be extended to the three-dimensional measurement [118].

LIF measurements in turbulent combustion are typically conducted using pulsed laser systems with a pulse length of 10 – 100 ns. Because the laser intensities

are relatively high, the produced fluorescence signal discriminates well against the chemiluminescence radiation, which continuously emits photons. The measured signal intensity, S_{LIF}, in the linear regime, which is created by a single laser pulse, can be formulated [57] as

$$S_{\mathrm{LIF}} \propto \frac{\Omega}{4\pi} V\eta \cdot I_{\mathrm{Laser}} \cdot N \cdot \sigma_{\mathrm{abs}} \cdot \frac{A_{21}}{(A_{21} + Z_{21})}. \tag{3.21}$$

The fluorescence intensity is proportional to the laser intensity, I_{Laser}, the particle number density, N, and the absorption cross section, σ_{abs}. The size A_{21} stands for the corresponding Einstein coefficient of the spontaneous emission. The quantity Z_{21} represents the radiationless loss rate of collisional quenching. It is the summation of the quenching rates for each of the collisional partners and is a function of the local temperature and composition given by

$$Z_{21} = N_{\mathrm{tot}} \sum_i X_i \sigma_i \left(\frac{8 k_{\mathrm{B}} T}{\pi \mu_i} \right)^{0.5}, \tag{3.22}$$

where N_{tot} is the total number density, X_i is the mole fraction, σ_i is the quenching cross-section and μ_i is the reduced mass [146]. The value $\Omega/4\pi \cdot V\eta$ is a test-dependent factor, consisting of the detected solid angle, Ω, the excited volume, V, and the transmission efficiency, η, of the detector.

When using two-photon absorption for fluorescence excitation, the equation expands to

$$S_{\mathrm{LIF}} \propto \frac{\Omega}{4\pi} V\eta \cdot I_{\mathrm{Laser}}^2 \cdot N \cdot \sigma_{\mathrm{abs}} \cdot \frac{A_{21}}{(A_{21} + Z_{21})}. \tag{3.23}$$

The quadratic dependence of the fluorescence on the laser intensity becomes visible. Additionally, σ_{abs} here denotes the absorption cross-section of the two-photon process. A detailed derivation can be found for single-photon absorption in [88] and two-photon absorption in [158].

The advantage of laser-induced fluorescence is its higher signal intensity compared to non-resonant processes (e.g., Raman spectroscopy). Furthermore, the spectral range of emission is usually outside the excitation wavelength of the laser. This prevents the occurrence of undesired stray light in the measurement signal.

3.3.3.1 CO-LIF

Quantitative measurement of CO concentration in combustion environments poses a major challenge. Because CO levels in typical flames are very low, a potential measurement system faces a stringent requirement for sensitivity and accuracy. A common procedure for determining the CO concentration is the use of LIF of the CO molecule. The energy levels of the CO molecule that are essential for LIF are shown in Fig. 3.6.

In principle, the excitation of the electronic levels $A^1\Pi^+$, $B^1\Sigma^+$ and $C^1\Sigma^+$ can take place. Due to the energy differences of the electronic levels, the required wavelengths for excitation are $\lambda < 200$ nm. These energies can only be reached in flames with two-photon processes. For two-photon CO-LIF, the most commonly used excitation wavelength is 230.1 nm, matching the $B^1\Sigma^+ \leftarrow\leftarrow X^1\Sigma^+$ transition. The $B^1\Sigma^+ \rightarrow A^1\Pi^+$ Angström band in the visible region (451 - 725 nm) is used for detection [1]. Besides, the 217.5 nm excitation of the $C^1\Sigma^+ \leftarrow\leftarrow X^1\Sigma^+$ transitions with subsequent fluorescence through the $C^1\Sigma^+ \rightarrow A^1\Pi^+$ Herzberg band (360 - 600 nm) [120] can be used in CO-LIF.

When using the CO-LIF technique in a flame, there are a number of energy loss and interaction processes that must be taken into account in a quantitative measurement.

Energy transfer to substance partners: During the transition processes, inelastic collision with surrounding particles can reduce fluorescence. In the case of CO-LIF, this factor must be taken into account in order to ensure a quantitative measurement of the CO concentration. Settersten et al. [161] investigated the quenching rates of excited CO with various partners.

Absorption of additional photons: The absorption of additional photons can cause photoionization of the CO molecules. Especially at high power densities of the laser, this process can be essential. As a result, the quadratic dependence of the LIF signal on the laser energy changes to a lower exponent.

Interference with C_2-LIF: The C_2 molecule is a radical in the flame, which can often interact with the CO-LIF measurement technique. Especially in fuel-rich flames, the C_2 concentration is high enough to have a measurable impact on the CO-LIF results. Part of the excitation energy for the CO molecule at 230.1 nm can be absorbed by C_2 molecules. The influence of this effect on the CO measurement is difficult to estimate in a real experimental set-up and is therefore often ignored.

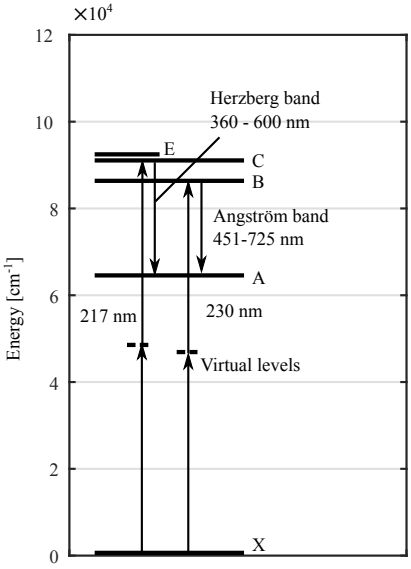

Figure 3.6. The electronic singlet states of the CO molecule and major transitions. Wavelengths are given for two-photon transitions [91].

In addition to the aforementioned effects, it must be taken into account that the fluorescence of the CO Angström band is in a similar range to that of the C_2 chemiluminescence of the Swan band, and thus they can interfere with each other. By using a narrow-band filter in front of the detector or very short exposure times, this problem can be avoided.

3.3.3.2 OH-LIF

The aim of planar OH distribution measurements in this work is the determination of the main reaction zone of flames. This area, referred to as the flame front, shows an increase in the OH concentration within a few micrometers. The behavior of the steep concentration gradient is shown by 1D flame calculations for an atomospheric and stoichiometric methane/air flame (Fig. 2.5). It can be seen that the position of the steepest OH gradient is shifted by approximately 0.4 mm relative to the steepest temperature gradient and thus is also a good indicator for the zone of greatest heat release [6]. A planar measurement of the OH distribution thus offers the possibility of determining the flame front position in a plane.

The absorption spectrum of the OH molecule has many transitions from the $X \rightarrow A$ level. These are in the UV range between 240 and 320 nm and can be calculated using spectroscopic database programs such as LIFBASE [123]. Depending on the temperature, the respective vibration levels of the electronic ground state are differently occupied. A detailed derivation of the OH spectrum can be found in [49].

Many absorption lines are accessible with laser systems and have been used in the past for LIF measurements. For example, upon excitation with XeCl excimer lasers, the $Q_1(3)$ line at 308.2 nm [159] was used. Applying Nd:YAG-pumped dye lasers, the $Q_1(6)$ or $Q_1(7)$ line at 282.9 and 283.2 nm [101, 176] may be excited. For planar measurements in a broad temperature range, the temperature-insensitive $Q_1(6)$ line is suitable and it yields a high fluorescence intensity. A close look at the simulated relevant absorption lines is shown in Fig. 3.7, where the $Q_1(6)$ line is marked.

In the excited state, there is an energy transfer with a change in the rotational quantum number (Rotational Energy Transfer, RET) and another energy transfer with change of the vibrational quantum number from $\nu' = 1$ to $\nu' = 0$ (Vibrational Energy Transfer, VET) as shown in Fig. 3.8. After a short residence time (in the order of ns), the ground state ($\nu'' = 0$) is restored with the spontaneous emission of a photon. Disturbances of this process can be caused by quenching of the excited molecule with other molecules. During the collision, the molecule transfers its excited energy and returns to its ground state without the emission.

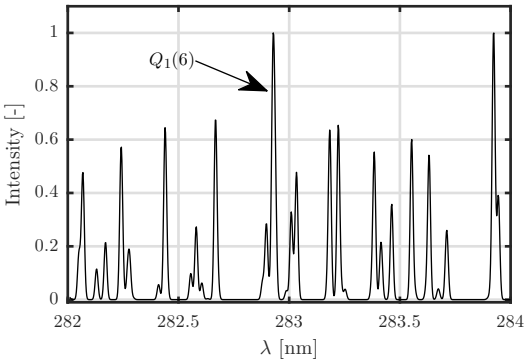

Figure 3.7. Simulated absorption lines of the OH radical at the excitation wavelengths from 282 to 284 nm by LIFBASE [123].

For the OH radical, these processes are produced by excitation of the first excited state $A^2\Sigma^+(v' = 1)$ from the ground state $X^2\Pi(v'' = 0)$ in Fig. 3.8. Due to the energy loss mechanisms mentioned above, the fluorescence is red-shifted, and is detected at 308 nm. Additionally, the $X^2\Pi(v'' = 1) \leftarrow A^2\Sigma^+(v' = 1)$ transition with fluorescence at 313 nm can be found simultaneously.

For the quantitative determination of OH, the knowledge of the temperature and quenching partners is always necessary, which limits the quantitative determination of OH [78]. Therefore, OH is mostly semi-quantitatively used as a criterion for the main reaction zone in flames.

3.3.3.3 CH_2O-LIF

Formaldehyde (CH_2O) is an important intermediate species in the oxidation of hydrocarbons as it is typically formed in cool-flame regimes or near the flame front. CH_2O is well studied spectroscopically. The $\tilde{A}^1A_2 - \tilde{X}^1A_1$ electronic transition is the subject of a paper by Dieke and Kistiakowsky [50]. The exploratory studies by researchers such as Brand [24], Moule and Walsh [133], Strickler and Barnhart [172], as well as Clouthier and Ramsay [40], extend the understanding of the electronic spectrum of CH_2O.

The transition $\tilde{A}^1A_2 - \tilde{X}^1A_1$ dominates the vibrational bands between 270 nm and 360 nm starting with the 4_0^1 and 4_0^3 bands, respectively [23]. The relevant excitation lines of the vibration band of the $\tilde{A}^1A_2 - \tilde{X}^1A_1$ transition are shown in Fig. 3.9. The spectroscopic detection of CH_2O has already been performed at

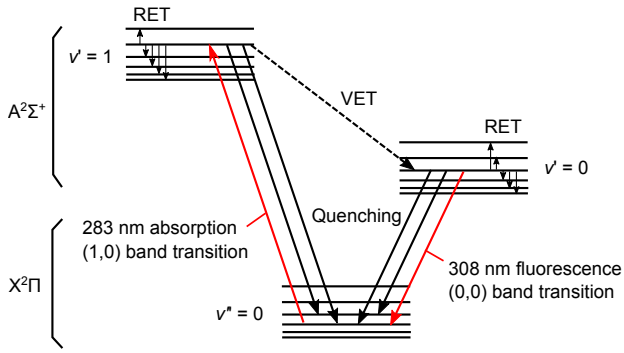

Figure 3.8. Schematic view of energy levels for the $X^2\Pi(v'' = 0) \leftarrow A^2\Sigma^+(v' = 1)$ transition of OH [110].

various wavelengths in many experimental studies within the range shown in Fig. 3.9.

The band 4_0^1 near 353 nm can be excited by XeF excimer lasers, which are tunable in a narrow wavelength range and thus can be set exactly to the respective transition [13]. A relatively weak, but very often used rotation transition at the edge of the 4_0^1 band can be stimulated at 355 nm [52, 82]. In this area, the quantum efficiency compared to 353 nm is very low. However, frequency-tripled Nd:YAG lasers are available at 355 nm with high pulse energies. Thus, they can partially compensate for the disadvantage of the weak band. Another disadvantage of 355 nm excitation is that polycyclic aromatic hydrocarbons (PAH) are excited in addition to CH_2O [76]. The PAHs are excited by their broadband absorption spectrum even at 353 nm. However, the ratio of detected PAH to CH_2O fluorescence by the excitation of a targeted transition with narrow-band dye lasers (≈ 0.1 cm^{-1}) is significantly smaller than that with non-seeded frequency-tripled Nd:YAG lasers (≈ 1.0 cm^{-1}).

The combination vibration of the $2_0^1\,4_0^1$ transition shows another experimentally used excitation wavelength [153, 163]. It lies in the range of 339 nm and is only to be stimulated with dye lasers. The achievable pulse energies are therefore generally lower than that from solid state lasers at 355 nm, but the $2_0^1\,4_0^1$ band has an advantage of more than 10 times the signal over the excitation of the 4_0^1 band at 355 nm, according to Paul and Najm [137]. Although energy levels in the 2_0^1 band are known to be dissociative, the large absorption cross section [151] compensates for it. There are also two practical advantages to move to an excitation at 339 nm. The emission is more separated from the pump wavelength that allows the more complete collection of disperse fluorescence using high-transmission interference

filters, and this wavelength is available with high-performance laser dyes. When the excitation laser is fixed on the isolated line at 339 nm, the dispersed fluorescence spectrum depicted in Fig. 3.10 is obtained covering the wavelength region from 380 to 470 nm. The emissions in the excited state can be clearly distinguished from the excitation laser [162]. In this work, the excitation wavelength of 339 nm is used.

Because there is insufficient information on the factors influencing the quenching of CH_2O [82] to calculate absolute CH_2O concentrations, only semiquantitative measurements of CH_2O-LIF have been reported by Paul and Najm [137], Kyritsis et al. [114] and Gordon et al. [82]. One possibility for reducing the influence of temperature on the quenching of CH_2O is the excitation of a hot band [108, 124]. Klein-Douwel et al. [108] excited the 4_1^0 band at around 370 nm, showing that the influence of temperature dependence on the LIF signal can be minimized.

Local heat release rate imaging by simultaneous CH_2O-/OH-LIF

When passing through the flame front of a premixed flame, high temperature chemistry increases the formation of OH radicals wheareas CH_2O molecules are formed in the cool-flame region as already discussed. In a spatially and temporally narrow area within the reaction zone, both OH and CH_2O are present simultaneously. Therefore, the simultaneous measurement of CH_2O- and OH-LIF is widely used to detect the zone of the heat release in premixed configurations [134]. In this study, the product of two-dimensional CH_2O- and OH-PLIF signals, $S_{CH_2O} \times S_{OH}$ is used instead of the product of their concentrations.

Laminar one-dimensional flame calculations[1] are carried out for stoichiometric methane/air and DME/air flames to complement the correlation between the heat release rate (HRR) and the product, $S_{CH_2O} \times S_{OH}$. The OH-LIF signals are calculated using the linear LIF regime expressed as Eqs. (3.21) and (3.22). Quenching cross-sections in Eq. (3.22) are obtained from Tamura et al. [174]. In contrast to OH-LIF signal simulations, those of CH_2O-LIF are more complex because it involves excitation of overlapping transitions and the temperature- and species-dependent quenching cross-sections are unknown. In this work, the procedure described in [41, 146] is used. Thus, the CH_2O-LIF signals are expressed by Eqs. (3.21) and (3.22) with the additional terms that account for temperature dependency of both populations of overlapping transitions and the quenching cross-sections. The temperature dependency of populations of the lower states relevant to transitions near

[1] This section is partly taken from the publication by Kosaka et al. [112] which was created during the work on this thesis. In Ref. [112], I shared authorship with Arne Scholtissek and we both contributed equally to this part.

the 339 nm excitation are calculated using AsyrotWin [12, 103] spectral simulation software for the temperature range from 300 K to 2000 K. For the spectral simulation, band origins and rotational constants are derived from [40]. Figure 3.11 shows simulated absorption lines near the 339 nm excitation of the $\tilde{A}^1A_2 - \tilde{X}^1A_1$ system ($2_0^1\,4_0^1$-, $4_0^2\,6_0^1$- and 4_0^3-bands) at 300 K. Absorption lines are convoluted with the line width of 0.05 nm and the resulting absorption spectrum is shown in Fig. 3.12. The calculated absorption spectrum shows a good correlation with the experimentally measured absorption spectrum shown in Fig. 3.9. To describe the temperature dependency of populations of the relevant transitions, the calculated absorption spectra for the different temperatures are convoluted with the dye-laser line profile. Figure 3.13 shows the calculated dependency and a temperature-dependent polynomial fit, f, described by

$$\begin{aligned} K_0 &= 0.1678 \\ K_1 &= 0.006498 \\ K_2 &= -1.808 \times 10^{-5} \\ K_3 &= 2.148 \times 10^{-8} \\ K_4 &= -1.311 \times 10^{-11} \\ K_5 &= 4.033 \times 10^{-15} \\ K_6 &= -4.954 \times 10^{-19} \end{aligned} \tag{3.24}$$

$$f(T) = K_0 + K_1 \times T + K_2 \times T^2 + K_3 \times T^3 + K_4 \times T^4 + K_5 \times T^5 + K_6 \times T^6$$

which is applied in this work. The procedure is further applied to the temperature dependency of populations of the relevant transitions near the 355 nm excitation and approved by the comparison with results from the literature [41, 145, 146]. For the quenching cross-sections, a temperature dependence of $T^{-0.5}$ [41] is applied.

Figure 3.14 shows the resulting correlation between the calculated $S_{CH_2O} \times S_{OH}$ and HRR. For the complement of flame curvature and strain, their influence on the correlation is considered and shown as a horizontal axis and the thickness of the line in Fig. 3.14, respectively. Here, positive flame curvature, κ, is defined as convex towards the unburned gas region, whereas negative curvature is concave towards the unburned gas.

The computational results show a good correlation between the calculated $S_{CH_2O} \times S_{OH}$ and HRR over the considered range of fuels, curvatures and strains. Following this correlation, qualitative HRRs are deduced from relative distributions of S_{CH_2O} and S_{OH} measured simultaneously by PLIF in this work.

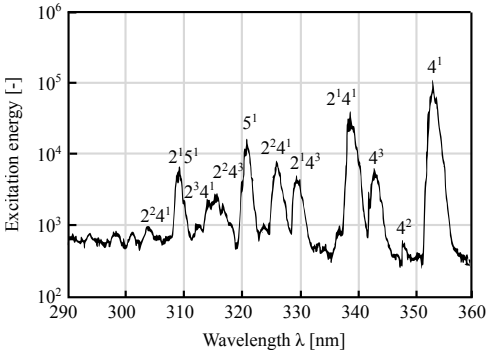

Figure 3.9. Absorption spectrum of the $\tilde{A}^1A_2 - \tilde{X}^1A_1$ transition of CH_2O. Marked are the individual transitions of the vibrational bands, according to [130].

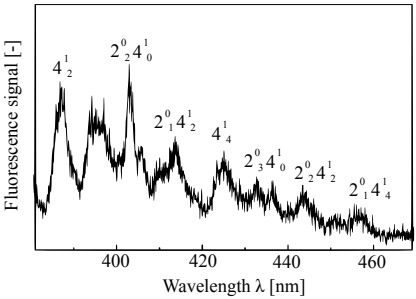

Figure 3.10. Dispersed fluorescence of CH_2O after excitation of the line in the $2^1_0 4^1_0$ combination band near 339 nm [163].

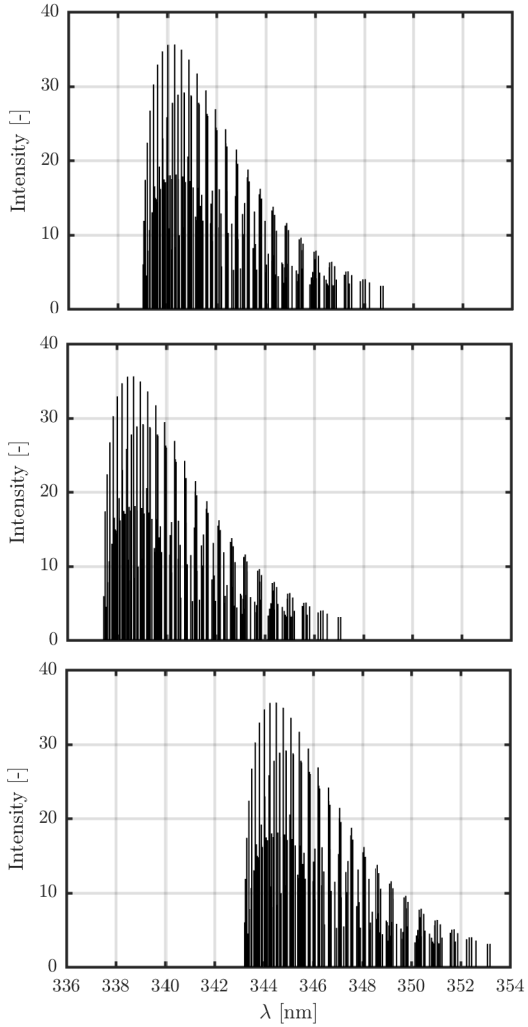

Figure 3.11. Simulated absorption lines of the $\tilde{A}^1A_2 - \tilde{X}^1A_1$ transition of CH_2O at 300 K by AsyrotWin [12, 103]. Top: $2_0^1\ 4_0^1$-band, middle: $4_0^2\ 6_0^1$-band, bottom: 4_0^3-band.

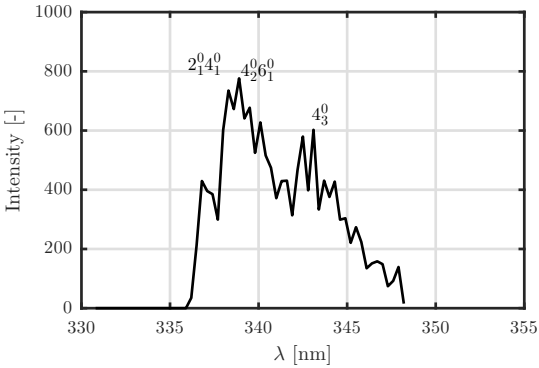

Figure 3.12. Calculated absorption spectrum of the $\tilde{A}^1A_2 - \tilde{X}^1A_1$ transition near the 339 nm excitation. Marked are the individual transitions of the vibrational bands.

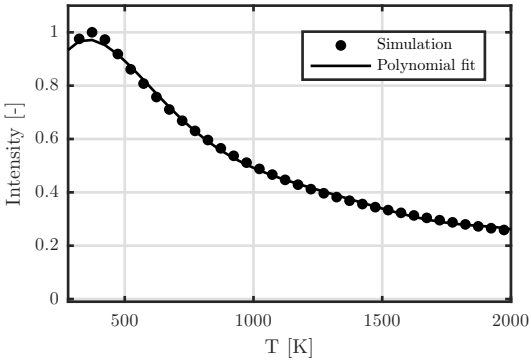

Figure 3.13. Calculated temperature dependency of population of lower states relevant to transitions near the 339 nm excitation of the $\tilde{A}^1A_2 - \tilde{X}^1A_1$ system (dot) and a temperature-dependent polynomial fit (solid line).

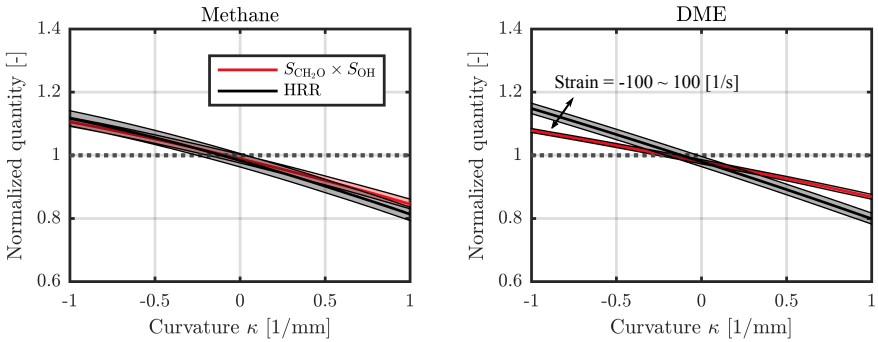

Figure 3.14. Correlation between the product of $S_{CH_2O} \times S_{OH}$ and HRR derived from premixed flame solutions for stoichiometric methane/air and DME/air flames. Curvature (horizontal axis) and strain (area along the line) are considered.

3.3.4 Laser-induced phosphor thermometry (PT)

For the remote determination of surface temperatures, thermographic phosphors (TP) provide the potential for a semi-invasive, accurate, temporally and spatially highly resolved sensing method [27]. Thermographic phosphors are rare-earth or transition metal doped ceramic materials (referred to as the host), whose phosphorescence emission following an (UV) excitation is temperature-dependent. Therefore, the temperature of phosphor-coated surfaces can be determined by measuring their phosphorescence spectral properties after laser excitation. In combustion applications, surface thermometry based on TPs has been used in static [25] or moving systems [51]. The phosphorescence process is shown in Fig. 3.15. In the following part, an idealized two-level system is assumed and S_0 refers to a singlet-ground state, S_1 is a singlet-excited state, T_1 a triplet-excited state to distinguish between different spin orientations. Detailed descriptions are given in [178].

Absorption: If a molecule (or an atom) is in the ground state, S_0, an incoming photon can convert it into an excited state, S_1. The incoming photon is annihilated during this process.

Relaxation: After the resonant absorption of a photon and the transition to a higher vibrational energy level of the excited state, there is the emission of a photon of the same wavelength. It is also possible that a non-radiative return to the lowest level of vibration energy takes place. The potential energy released in the process is converted into kinetic energy of the molecule and transferred to neighboring molecules. This process is referred to as relaxation.

Relaxation involves further non-radiative transfer processes that significantly reduce the expected emission intensity, where substances can lead to a transition between two electronic states of different spin multiplicity ($S_1 \rightarrow T_1$). This non-radiative transition is called intersystem crossing. It leads to the population of a multiplet (e.g. triplet) state. Although this transition between different spin multiplicity is spin-forbidden, it is a very efficient process for phosphorescence. The energy transferred to the multiplet level is therefore no longer available for fluorescence.

Emission: Population distributions of excited molecules can be derived from the relative position of the potential curves as shown in Fig. 3.1. The Franck-Condon principle provides a detailed explanation of vibronic transitions. A detailed description is omitted here with reference to the corresponding literature [91].

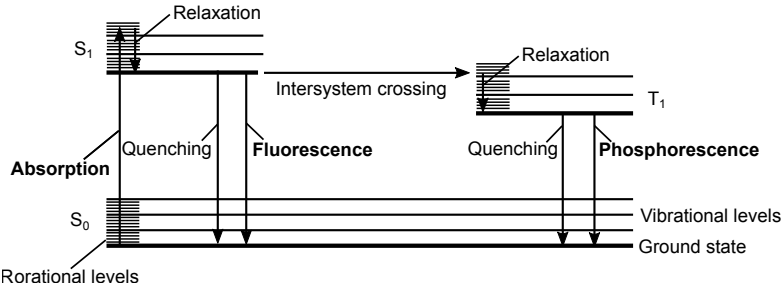

Figure 3.15. Jablonski energy level diagram showing the luminescence process [119].

In the idealized two-level system shown in Fig. 3.15, after the transition to the excited state, S_1, spontaneous emission takes place, and a molecule returns to the electronic-ground state ($S_1 \rightarrow S_0$). This process is a spin-allowed (singlet-singlet) transition that is on the order of nanoseconds.

Another pathway to the ground state is via an intersystem crossing associated with relaxation, which results in phosphorescence. The non-radiative process of the intersystem crossing represents a competitive process to fluorescence and provides the population of a multiplet state (T_1). The return to the singlet ground state ($T_1 \rightarrow S_0$) is generally spin-forbidden and therefore unlikely to occur, as reflected in the long lifetime of phosphorescence.

As mentioned above, the processes of intersystem crossing between non-degenerated and degenerated electronic states are required for phosphorescence but they are usually forbidden on the bases of quantum-mechanical selection rules, resulting in low probabilities of occurrence. The probability strongly depends on the probed molecule. For example, for molecular structures with higher atomic sizes (e.g. transitional metals) this probability increases. Many efficient phosphors originate from a deliberately added impurity.

The transitions between states of different spin multiplicities ($S_1 \rightarrow T_1$ and $T_1 \rightarrow S_0$ in Fig. 3.15) are orders of magnitude slower than fluorescence. They cause the phosphorescence decay time to be of the order of 1 μs to 100 μs at room temperature. An example of measured phosphorescence intensity profile at different temperatures is shown in Fig. 3.16. With increasing temperature, higher energy vibrational states are excited, promoting non-radiative relaxation pathways. The increase in the rate of non-radiative transitions results in a faster depopulation

of the excited state and therefore a shorter phosphorescence lifetime as shown in Fig. 3.16.

Types of phosphor thermometry: In the past, several approaches have been investigated to use the phosphorescence for thermometry. These approaches can be divided into : time-resolved and time-integrated methods. The first approach needs to temporally resolve the phosphorescence and use it for the determination of its rise or decay time (time-domain) or of its phase shift to a modulated excitation (frequency-domain) [2, 107]. The time-integrated approach often exploits the temperature dependent change of the overall phosphorescence intensity or spectral position of one or more spectral bands of the emission spectrum [179]. The time-resolved approach (especially decay time methods) are generally superior in accuracy and precision, whereas the time-integrated methods have an advantage for thermometry in the measurement of fast moving targets [70]. Since the object for thermometry in this work is a static wall surface, a time-resolved approach is suitable. In the following part, the decay time method is further explained.

To describe time-dependent phosphorescence, Becquerel [9] provided a decomposition equation, which describes the phosphorescence intensity with a monoexponential approach,

$$I(t) = I_0 e^{-\frac{t}{\tau}}. \tag{3.25}$$

The time-dependent intensity, $I(t)$, is thus dependent on the initial intensity, I_0, at time $t = 0$ directly after the excitation and the decay constant, τ, which is referred to as the decay time.

For the choice of a suitable phosphor, the temperature range, the relevant time scales and the properties of the detection system are decisive. On one hand, the phosphor must have sufficient sensitivity in the expected temperature range. On the other hand, the phosphorescence decay must be short enough so that temperature changes of the measurement target are not faster than the decay. In addition, the detection system must be able to temporally discretize the decay process. This results in an upper limit of the phosphorescence decay time due to the expected dynamic of temperature changes, and a minimum decay time limited by the bandwidth of the measurement system. Furthermore, the dynamics of the phosphor must allow sufficient precision of the temperature measurement. The phosphor must be excitable in a suitable manner and should have a monoexponential decay. Finally, the signal intensity should be high and the emission should be in a favorable wavelength range.

For surface temperature measurements in combustion applications, gadolinium gallium garnet doped with chromium ($Gd_3Ga_5O_{12} : Cr$) has in principle suitable

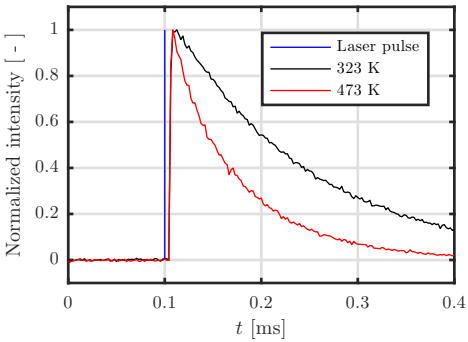

Figure 3.16. Two measured phosphorescence intensity profile of $Gd_3Ga_5O_{12} : Cr, Ce$ at 323 and 473 K.

properties due to its decay time [71]. A problem is the afterglow of this phosphor, which can be avoided by a co-doping with cerium [72]. $Gd_3Ga_5O_{12} : Cr, Ce$, which is used in this work, is highly luminous, has approximately a mono-exponential decay, and is sensitive in a range from room temperature to about 750 K. The emission takes place in a wavelength range of about 700 to 850 nm and it is therefore suitable for detection with monochromatic CMOS cameras. The decay time ranges from 10 to 100 μs and can be temporally well discretized with a correspondingly reduced resolution with high-speed CMOS cameras.

4 Flame-wall interaction burner and supplemental laminar flame calculation

Flame-wall interaction (FWI) processes have a decisive influence on the formation of pollutants and heat losses in complex technical combustion systems. However, experimental investigations in real geometries are often difficult to conduct. Real systems have only very limited accessibility for diagnostics and the combustion processes are often very complex. Due to unknown boundary conditions such as fuel composition or elaborate geometries, it is almost impossible to separate the actual flame-wall interaction from other effects. For these reasons, research on basic FWI processes rely on generic experimental setups. These systems have the advantage of defined boundary conditions combined with a good metrological accessibility and a manageable degree of complexity, which are also required for a numerical calculation as for comparison. In this work, a canonical configuration, which is called a side-wall quenching (SWQ) configuration, is used.

4.1 Burner construction and operating conditions

The burner used in this study for the SWQ configuration (called SWQ burner) is sketched in Fig. 4.1. This burner was previously constructed and built in [97] and it is used in this work with modifications for varying the wall temperature and the fuel. The burner consists of a converging Morel nozzle with a quadratic cross-section (40×40 mm^2) to provide a top-hat velocity profile at the outlet. Homogeneously mixed fuel and dry air are fed to the burner's plenum at room temperature. Honeycombs and fine meshes are used to homogenize the flow before it enters the converging part of the nozzle. Sharp edges at the nozzle exit minimize recirculation zones. Turbulence intensities can be enhanced by an optional turbulence grid. A dried air co-flow surrounds the premixed central jet flow. All flow rates are controlled by calibrated mass flow controllers (Bronkhorst). A circular ceramic rod (diameter 1 mm) is placed 16 mm above the nozzle exit to stabilize a V-shaped premixed flame. One branch of this V-flame impinges on a temperature controlled stainless steel wall. Since the mean axial flow is parallel to

Table 4.1. Operating conditions of the SWQ burner.

	Main flow					Co-flow	
Fuel	Re [-]	ϕ [-]	U_{bulk} [m/s]	$\dot{m}_{air}$ [g/s]	$\dot{m}_{fuel}$ [g/s]	U_{bulk} [m/s]	$\dot{m}_{air}$ [g/s]
Methane	5000	0.83	1.88	3.24	0.156	1.35	3.5
		1	1.88	3.19	0.186		
		1.2	1.88	3.14	0.219		
Dimethyl ether	5000	0.83	1.80	3.19	0.296	1.35	3.5
		1	1.78	3.13	0.350		
		1.2	1.77	3.06	0.411		

the wall, side-wall quenching (SWQ) occurs. The front side of the wall, where the flame impacts, is cylindrical with a slight curvature (radius 300 mm). This curved shape allows the use of focused point-wise laser diagnostics very close ($\approx 100\ \mu$m) to the wall surface. The entire burner is mounted on a traversing system. Experiments are performed with an equivalence ratio of 0.83, 1.0 and 1.2 for methane/air and dimethyl ether (DME)/air flames. The Reynolds number is set to 5000 based on nozzle exit conditions of the fuel/air jet (the characteristic length scale equals the hydraulic diameter of the nozzle edge, 41.7 mm). The corresponding bulk flow velocities and mass flow rates at standard temperature and pressure conditions are summarized in Table 4.1. Laminar flames are investigated without the turbulence grid (TG) in place whereas turbulent flames are generated by inserting the grid. Due to Helmholtz resonances generated by the burner's plenum, the laminar flame tip near the wall shows axial fluctuations in the order of $\pm$ 200 μm.

Wall temperatures are controlled by a bath-thermostat (Huber, CC-304B) operated with thermal oil (Huber, thermofluid P20.275.50). Oil temperatures are set to yield wall temperatures of 330, 450, 540 and 670 K measured by a thermocouple embedded in the wall ($\approx 80\ \mu$m behind the surface) and placed at $z = 48$ mm (see Fig. 4.1b). The coordinate system is defined such that z points along the axial direction, being zero at the nozzle exit and positive in the downstream direction (see Fig. 4.1b).

For all measurements in this work, the laser optics as well as the detection system are installed stationary, whereas the burner stands on traversing units during measuring operation. These can be moved in all three spatial directions with a repeat accuracy and an absolute positioning capability of $< 5\ \mu$m each. Thus, a precise alignment of the burner relative to the measurement location is possible.

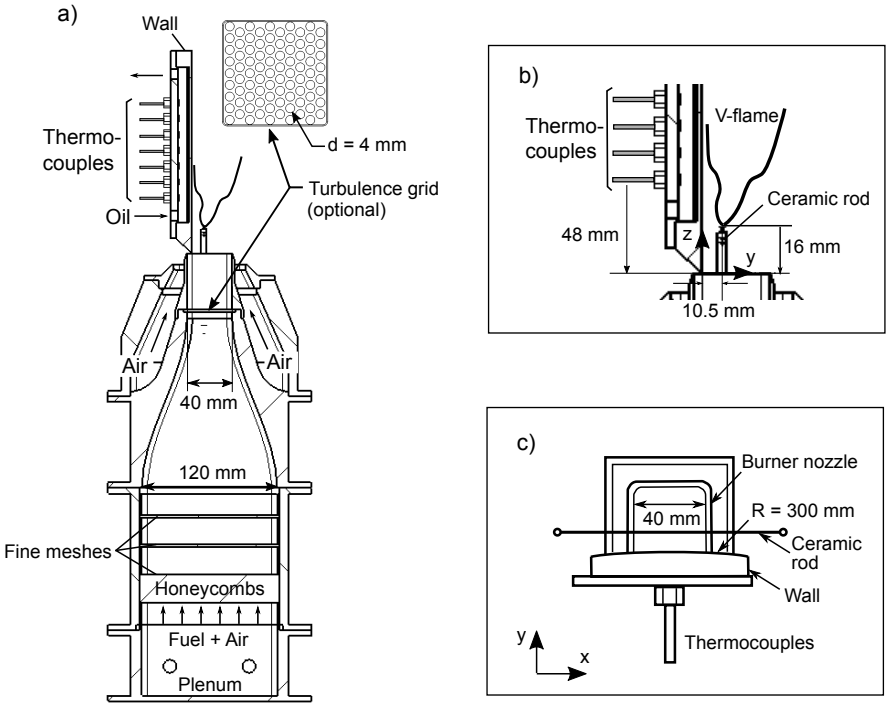

Figure 4.1. Construction of the SWQ burner. The x - y - z coordinate system is shown in the detailed drawing of the nozzle region. a) Side view, b) details of nozzle exit and positions of the thermocouples with a side view, c) details of nozzle exit and wall shape with a top view.

4.2 Characterization of the flow boundary conditions

4.2.1 Experimental setup

For a characterization of the flow field and a deeper understanding of the flame dynamic processes in the studied side-wall quenching (SWQ) configuration, measurements of the velocity field are made on the SWQ burner. Measured planes are located in different areas of the burner. For insights of the cold flow without the wall, a first measurement field of size, 42 (y) × 32.5 (z) mm^2, is located in the area of the burner exit (Fig. 4.2 b). Subsequently, the influence of the wall on the flame is examined with a similarly large measurement field of 18 × 18 mm^2 in the quenching zone of the flame (Fig. 4.2 c). The orientation of the wall corresponds to the standard configuration described in Section 4.1. Both measurement planes are perpendicular to the wall oriented in the symmetry plane of the burner.

For the measurement of the velocity field both above the nozzle and at the quenching zone, two-dimensional / two-component PIV is used. For this purpose, Al_2O_3 particles of 1 μm diameter in average are mixed in the main flow. These particles have a melting temperature of over 2300 K and thus are usable with typical flame temperatures.

For the measurement above the nozzle, the particles are illuminated with a frequency-doubled Nd:YAG laser (λ = 532 nm, max. 30 mJ/pulse at 10 Hz, NewWave, Gemini PIV). The laser beam is shaped to a light sheet by a combination of cylindrical lenses and focused to the measurement plane to an approximately 120 μm sheet as shown in Fig. 4.2 a. To detect the Mie-scattering from particles, a digital CMOS camera (LaVision, Imager sCMOS) equipped with a 180 mm lens (Sigma AF 180 mm f / 3.5 EX HSM APO), which is arranged perpendicular to the measurement plane, is used.

The measurement at the quenching zone[1], the higher repetition rate is required for the statistical analysis of the turbulent behavior, such as integral scales. The particles are therefore illuminated with a high-speed frequency-doubled Nd:YVO_4 laser (λ = 532 nm, 4.0 mJ/pulse at 10 kHz, Edgewave IS 4II-DE) in the measurement plane. To detect the Mie-scattering from particles, a digital high-speed CMOS camera (Vision Research, Phantom v711) equipped with a 180 mm lens (Sigma AF 180 mm f / 3.5 EX HSM APO) is used.

For the measurement above the nozzle and at the quenching zone, the software DaVis 8 (LaVision) is used to process the PIV raw images. After a spatial calibration

[1] This measurement was performed by Christopher Jainski and Martin Rißmann during the work on the thesis [97]. We contributed equally to this section.

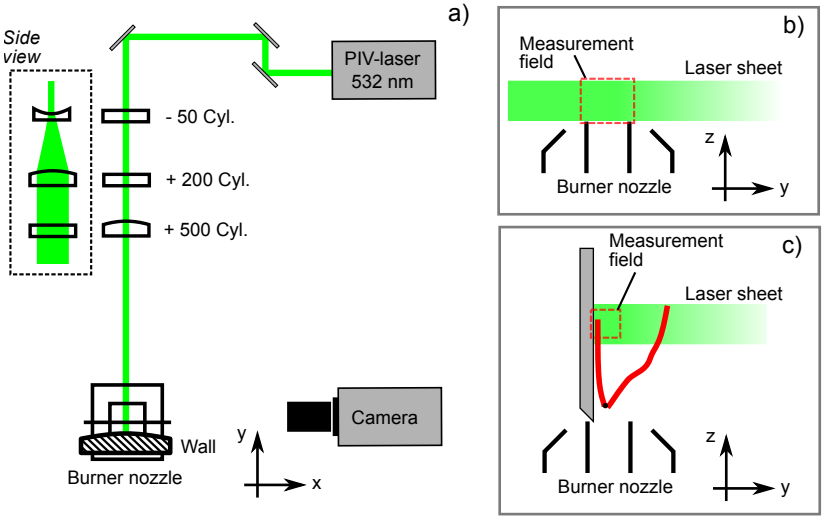

Figure 4.2. Optical setup of PIV measurements on the SWQ burner. a) Top view, b) configuration for the flow field characterization above the nozzle with a side view, c) configuration for the measurement in the quenching zone with a side view.

with a point target (Type 7, LaVision), the time-series images are processed. The process starts with an interrogation window of 64 × 64 pixel^2, which is reduced to 32 × 32 pixel^2. Furthermore, a window overlap of 75 % is selected, resulting in a vector spacing of 190 μm.

For the measurement configurations of the area above the burner exit, the resulting velocity field is evaluated and discussed in the following Section 4.2.2. The measurement in the quenching zone of the flame, recorded at 10 kHz, offers the possibility to identify and evaluate transient processes in the measurement data. The results of this measurement with the wall are discussed later in Section 5.3.

4.2.2 Flow boundary conditions

During the design of the SWQ burner, it is of particular importance to achieve defined and reproducible boundary conditions at the outlet of the nozzle. In the case of the configuration without the turbulence grid, the flow should be as laminar as possible. These properties are characterized by PIV measurements of the velocity field above the nozzle exit. The burner is operated without combustion with air

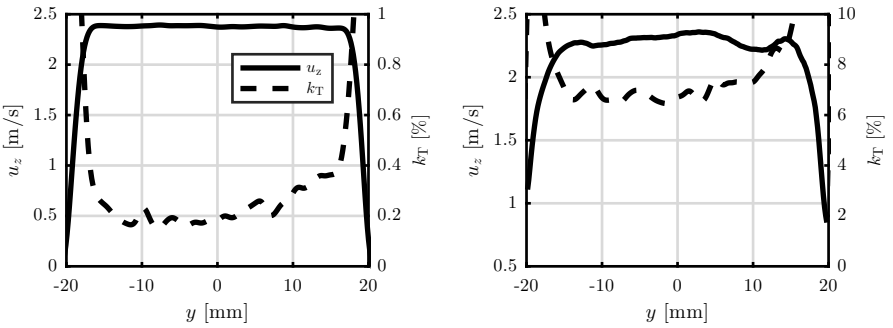

Figure 4.3. Profiles of the mean axial velocity, u_z, and the turbulent intensity, k_T, in the center plane of the nozzle 5 mm above the nozzle outlet. Left: laminar case without the TG, right: turbulent case with the TG. Re = 5000 without combustion. At $y = 0$ mm, the center axis of the nozzle is located.

as flow medium and without wall. Figure 4.3 shows the average profiles of axial velocity, u_z, at the nozzle exit for both laminar and turbulent configurations. These are measured 5 mm above the nozzle at a Reynolds number of 5000. It shows in both cases a well-formed top-hat profile of the flow. In the turbulent flow, however, influences from the turbulence grid in the form of small bumps can be seen. When considering the turbulent intensity, k_T ($= \sqrt{\overline{u'^2}}$), it is noticeable that the flow without the TG exhibits laminar behavior. Here, k_T of the core flow is below 0.4 %. In the turbulent configuration, k_T is above the laminar case at 6-8 %.

4.3 Laminar flame calculations

Laminar one-dimensional flame calculations[2] are carried out to complement the experimental observations. Therefore, two different flame simulations are applied: Cantera [80] for a flat flame burner configuration, which is presented in Section 5.1.1, and an in-house solver [193] for the SWQ burner, respectively. Furthermore, for the SWQ burner, two different flame configurations are studied: an undisturbed, adiabatic freely-propagating flame [104] and a premixed flame which contains an additional enthalpy defect representing heat transfer to a wall. Comparing the two flame configurations, the response of the thermochemical states

[2] This section is partly taken from the publication by Kosaka et al. [113] which was created during the work on this thesis. In Ref. [113], I shared authorship with Arne Scholtissek and we both contributed equally to this part.

of the premixed flame to heat loss can be examined. For the in-house solver, the following equations are solved,

$$\frac{\partial \varrho u}{\partial z} = 0 \tag{4.1}$$

$$\varrho c_\mathrm{p} \frac{\partial T}{\partial t} + \varrho c_\mathrm{p} u \frac{\partial T}{\partial z} = \frac{\partial}{\partial z}\left(\lambda \frac{\partial T}{\partial z}\right) - \varrho c_\mathrm{p} \frac{\partial T}{\partial z} \sum_{i=1}^{N} c_{\mathrm{p},i} Y_i V_i - \sum_{i=1}^{N} h_i \dot{\omega}_i - \dot{q}_\mathrm{wall} \tag{4.2}$$

$$\varrho \frac{\partial Y_i}{\partial t} + \varrho u \frac{\partial Y_i}{\partial z} = -\frac{\partial}{\partial z}(\varrho Y_i V_i) + \dot{\omega}_i \tag{4.3}$$

where T and Y_i represent temperature and species mass fractions, respectively, ϱ, the density, u, the velocity, c_p, the specific heat capacity, λ, the thermal conductivity, h, the enthalpy and $\dot{\omega}_i$, the net formation rate of species i. The species diffusion velocity, V_i, is modelled with a mixture averaged approach according to Curtiss and Hirschfelder [42]. In the temperature equation, the term $\dot{q}_\mathrm{wall}$ models a sink term due to heat transfer to the wall. For the undisturbed freely-propagating flame this term is set to zero while for the premixed flame with wall heat transfer it is modelled as,

$$\dot{q}_\mathrm{wall} = \lambda \frac{A_\mathrm{wall}}{V_\mathrm{cell}} \frac{\partial T}{\partial y} = \lambda C (T - T_\mathrm{wall}) \tag{4.4}$$

where C is a parameter which is a function of the wall-normal coordinate, y. It incorporates the distance to the wall and relates the wall surface area, A_wall, to the cell volume, V_cell. For the premixed flame with wall heat transfer, this parameter is successively increased until reaching the extinction limit of the flame due to the imposed heat losses. Results shown below are for a value of the parameter C as close to extinction as possible. This modeling approach can be considered as a first step to describe the impact of heat-losses associated with side-wall quenching on the thermochemical state. A more sophisticated and quantitative approach would require a fully-resolved 2D simulation as shown in [77].

The equations above are solved using an in-house flame solver [193] with a damped Newton algorithm and adaptive mesh refinement. Transport properties are evaluated with the EGlib transport library [62] and chemical source terms are obtained from an in-house chemistry library. For the computations of methane/air and DME flames, the GRI-3.0 mechanism [164] and the mechanism of Zhao et al. [192] are used, respectively.

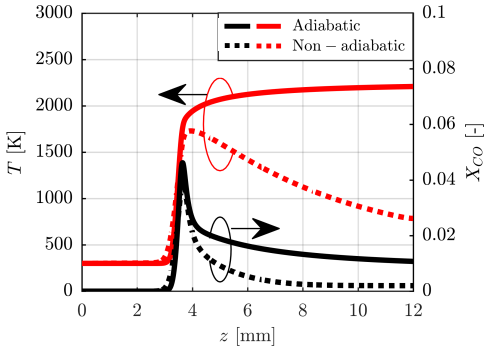

Figure 4.4. Premixed flame solutions with (non-adiabatic) and without (adiabatic) wall heat transfer. Temperature (red) and CO mole fraction profiles (black) versus the physical space coordinate z.

Figure 4.4 shows the premixed flame solution for the stoichiometric methane/air flame with (non-adiabatic) and without (adiabatic) wall heat transfer in physical space. It is observed, that heat losses to the wall substantially influence the overall flame temperature and especially the post-flame oxidation zone, while the effect on the pre-heat zone is minor. These trends will be discussed below in the analysis of the experimental results.

5 Investigation of wall heat flux and thermochemical states

One of the main reasons for the flame quenching during the FWI is the enthalpy loss across the wall. This causes also the change of flame chemistry in the near-wall region as already described in Section 1.2.2. The aim of this experiment presented in the following chapter is to describe the wall heat flux and the thermochemical states during side-wall quenching (SWQ). For this purpose, the previously described SWQ burner from Section 4.1 is used. The chapter begins with a description of the optical setup used here, the characterization of the measurement systems and the data evaluation. Subsequently, a global analysis of flame behavior and wall heat fluxes is presented. Additionally, certain aspects of thermochamical states are discussed in terms of CO/T-scatter plots.

5.1 Combination of CARS/CO-LIF/phosphor thermometry/OH-PLIF

Figure 5.1 displays the optical arrangement of the applied laser diagnostics. Gas phase temperatures are measured by CARS and CO-concentrations by CO-LIF. Additionally, wall surface temperatures are recorded by phosphor thermometry (PT) along a line in the axial direction. For flame front tracking, planar OH-LIF is applied. The OH-image plane is aligned perpendicularly to the wall. Because CARS and CO-LIF used in this work are the point-wise measurement techniques, each recording is carried out with traversing the burner assembly in the y- and z-directions as shown in Fig. 5.1. For each measurement position, a set of 400 (in the laminar case) or 20000 (in the turbulent case) CARS/CO-LIF data points are recorded with the phosphorescence and OH-PLIF images.

5.1.1 CARS

For the measurement of gas phase temperature, the ro-vibrational CARS method with the nitrogen molecule (N_2) is used in this experiment. In the process, both the vibration and rotation states of the N_2 molecule are used, which is particularly suitable in flames due to its stability for high temperature. As explained in Section

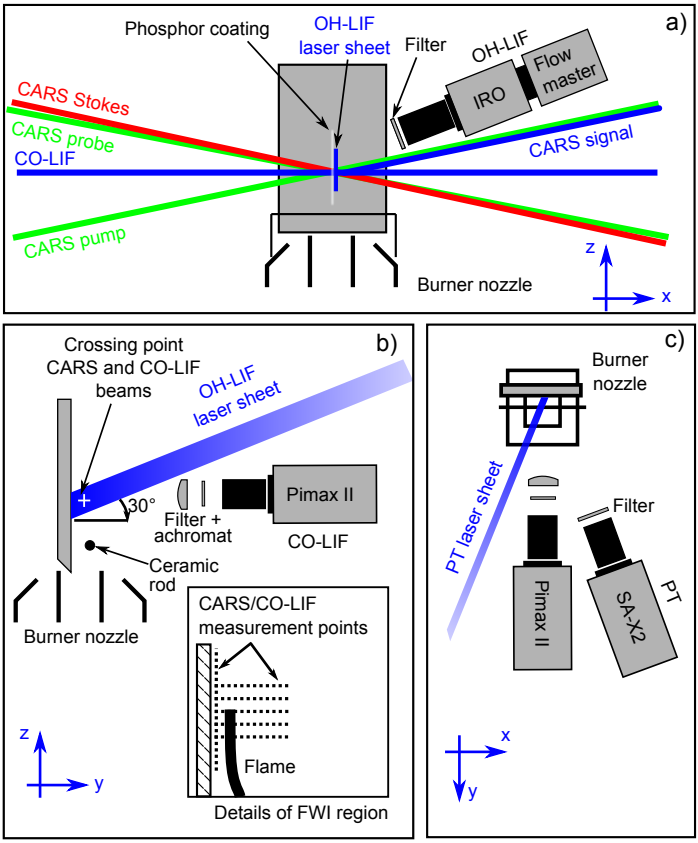

Figure 5.1. Optical arrangement for the combined CARS, CO-LIF, phosphor thermometry and OH-PLIF measurements. a) Front view, b) side view, c) top view. At the wall, the light sheet used for OH-PLIF imaging is displaced 1 mm from the phosphor coating to avoid bias in the recordings and damage of the coating.

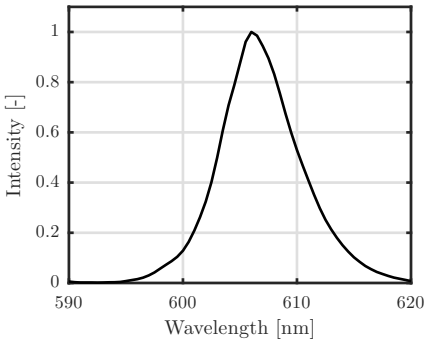

Figure 5.2. Measured emission spectrum of the broadband Stokes laser with a central wavelength of 607 nm, which is taken with a spectrometer (BLACK-Comet C-50).

3.3.2, the three laser beams of the pump, Stokes and probe are used for the CARS excitation. The CARS signal is recorded by a spectrometer coupled with a CCD camera.

5.1.1.1 Optical setup

The CARS setup is based on a Q-switched frequency doubled Nd:YAG laser (Spectra-Physics, Quanta-Ray PIV-400-10, one cavity used) operating at 532 nm and a 10 Hz repetition rate. The laser output is split into both pump and probe beams as well as into a third beam for pumping a custom-build modeless dye laser, following the design principles from Ewart [63]. The dye laser provides a broad emission spectrum for the Stokes beam using a mixture of Rhodamine 610 and Rhodamine 640 laser dyes dissolved in ethanol. The emission of the dye laser is optimized for a peak intensity around 607 nm as shown in Fig. 5.2.

Pulse energies for each laser beam are adjusted by a combination of half-wave plates and polarizing beam splitter cubes (18 mJ for the pump and probe beams and 13 mJ for the Stokes beam). Telescopes are used to collimate the beams. Planar BOXCARS phase-matching is realized parallel to the surface of the wall by using a spherical lens ($f = +300$ mm). To satisfy the phase-matching condition, angles of 2° (pump and probe) and 2.3° (Stokes) relative to the principal beam direction are chosen. After the probe volume, the four beams are collimated with another spherical lens ($f = +300$ mm). Since the CARS signal is nearly superimposed on the pump beam, the pump beam is separated from the CARS signal by two dichroic mirrors (HT at 532 nm and HR at 473 nm) and a band-pass filter (HR

at 532 mm). The probe and Stokes beams are directed into a beam dump after the beams pass the area of interest. The CARS beam is then focused with a spherical lens ($f = +100$ mm) and spatially aligned with the spectrometer slit (SPEX Industries, SPEX 1707). The spectrometer is equipped with a grating of 2400 lines/mm and operates in its first diffraction order. It is spectrally calibrated by means of a xenon spectral lamp (LOT Oriel, LSP033) at the three emission-peak wavelengths of 473.41, 479.26 and 480.7 nm and a subsequent creation of a linear calibration polynomial.

CARS spectra are recorded at 20 Hz by a CCD camera (Princeton Instruments, Pixis 400) mounted in the spectrometer, using 1340 × 40 pixels of the chip with a vertical binning (all 40 pixels). Every second image recording is located in between two laser pulses (10 Hz) and is used to perform a background subtraction in the post-processing. Furthermore, a pure methane flow is used to generate non-resonant spectra which is necessary for spectral correction of the Stokes laser influence in the CARS post-processing. The recorded single-shot spectra are fitted using the CARSFT algorithm [37]. For temperatures below 1200 K, CARS signals are recorded using a 10 % transmission neutral density (ND) filter in front of the spectrometer to match signal intensities to the dynamic range of the CCD camera. At locations with large temperature fluctuations, the data is recorded for both filter setups, i.e., with and without the ND filter. Above 1200 K, signals are recorded without the ND filter in place.

The coordinate y denotes the wall-normal direction with $y = 0$ mm fixed at the wall surface. The wall-closest point is determined by monitoring the attenuation of the pump beam with a beam monitor placed behind the burner assembly in the beam-wise direction. Using this method, the $y = 0$ mm point can be determined with an accuracy of $\pm$ 30 μm. The wall-closest measurement point of CARS/CO-LIF is located at a wall distance of 100 μm.

5.1.1.2 Data evaluation

Pre-process

Before the measured CARS spectra can be evaluated for temperature determination, they need a series of corrections. First, a shot-to-shot background is subtracted from the raw data. This step is especially important in order to separate the luminescent signal of the C_2 molecule from the CARS signal. This lies in the same spectral range. The subtraction also removes the dark and ambient noise of the spectrum.

Thereafter, all spectra are normalized to the maximum value (usually the peak of the first vibration level). In the next step, a further normalization takes place on the average non-resonant background. The background can be taken in nitrogen-free environment (here: methane). With the information of the non-resonant background, the spectral Stokes laser profile and the spectral transfer function of the detection system can be taken into account. In a final step, the square root of each spectrum is taken, since the height of the recorded bands in the CARS spectrum is proportional to the square of the temperature (or susceptibility $\chi^{(3)}$). The prepared spectra are then handed over to CARSFT as described in the following.

Fitting of the spectra

The evaluation is based on the CARSFT routine [37], which is called automatically via a MATLAB script developed in [106]. The whole procedure is summarized in Fig. 5.3. The CARSFT code calculates theoretical CARS spectra and fits them to measured data. The free parameters of the fit are called the control and fit parameters. The control parameters represent experimental parameters such as the line shape of the transitions or the polarization and angle of the laser beams. These parameters are set once at the beginning of the evaluation and remain mostly constant thereafter for all measurement points. The fit parameters include, for example, a spectral offset of the recorded data and the temperature corresponding to the spectrum to be finally determined. These are often not known in advance and are changed during the evaluation.

For the fast convergence of the fit variables, the averaged spectrum is fitted for each measurement point in a first step. Initially, only the first CARS vibration band is used and a set of parameters is determined in several iterations (see Fig. 5.3 A). In the next step, the second CARS vibration band is included in the evaluation and the parameter set is refined further iteratively (Fig. 5.3 B).

The determined parameters are used as a basis for further evaluation. First, a starting temperature for the following single-spectrum evaluation is determined from the mean value spectrum (Fig. 5.3 C). In the single spectral analysis, the temperatures of all spectra are determined with the previously determined parameter set (Fig. 5.3 D). In this step, only the temperature is a fit parameter.

Combining temperature data

In unsteady systems, such as with the introduction of turbulent flows and FWI, large temperature fluctuations can be present. Due to the quadratic dependence of the CARS signal on the temperature, the dynamic range of the used CCD camera is

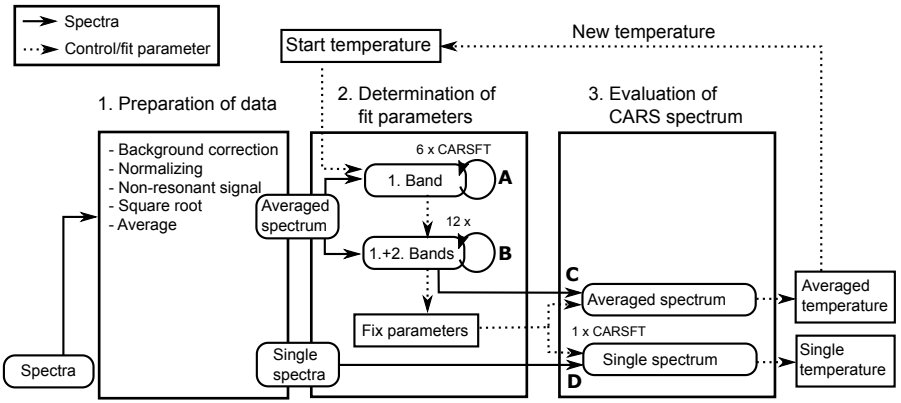

Figure 5.3. Program sequence of the temperature calculations by means of CARS [106]. The round arrows indicate an iterative fit process using CARSFT. Dashed lines: flow of control and fit parameters.

not sufficient to cover both cold and hot gas signal amplitudes. In order to obtain representative statistics in areas of high temperature fluctuations, these areas are recorded with different strength neutral density filters. By means of fixed threshold values of the peak intensity, the spectra are selected before the evaluation and the usable values are handed over to the fit algorithm. Afterwards, the temperatures recorded for the same measurement with two filter combinations (with and without the filter) are calculated and the mean value is taken from all valid temperatures.

5.1.1.3 Spatial and temporal resolution

The spatial resolution of the system is determined by the overlap of the three laser beams in the measurement volume. The beam diameters are measured in the focus area with a beam monitor (Data Ray Inc., WinCamD). The full width at half maximum (FWHM) are 50 μm for the pump and probe lasers and 70 μm for the Stokes laser. The overlapping area is therefore approximately 50 μm. In the beam wise direction, the measurement volume is determined by traversing a thin glass plate (0.1 mm). The plate also produces a broadband resonant signal of the material of the glass, which is detected with the spectrometer as a function of the displacement of the plate. The measured FWHM of the peak-value profile with the traversing in the beam wise direction is 1.5 mm. The temporal resolution is given by the laser pulse duration, while all three beams are superimposed in the

measurement volume. This is detected by means of a photodiode and is measured to be approximately 9 ns (FWHM). The system repetition rate between two CARS acquisitions is 10 Hz.

5.1.1.4 Precision and accuracy

In order to quantify the precision of the CARS system, measurements are made on both a tube heater and a matrix-stabilized premixed flat flame burner [83]. The tube heater covers the temperature range of 300 - 900 K. The flat flame achieves the temperature range of about 1900 - 2200 K with operation at $0.8 < \phi < 1.3$. The relative standard deviation of derived temperatures by CARS is given in Fig. 5.4. Since both systems can be considered stationary, the precision can be calculated from the standard deviation of the measured temperature. It is found that the precision has a strong dependence on the temperature. Such a behavior can be explained by the excitation of the quantum-mechanical states of the N_2. A resulting CARS spectrum (300 K) as shown in Fig. 3.5. If only the first vibration level is excited at room temperature, the recorded spectrum can only be compared with the theoretical spectra which exhibits a single peak. This leads to a relatively poor precision of the ro-vibration CARS method used at lower temperatures. As the temperature increases, more and more levels of the N_2 are excited. Thus, the quality of the calculated fit increases significantly and leads to an improved precision at flame temperatures.

The measurement accuracy of the CARS method is given based on the tube heater and the exhaust gas region of the flat flame burner. For this purpose, the outlet temperatures of the tube heater are measured with a thermocouple (type K) as a reference. The temperatures of the flat flame burner exit are evaluated with the adiabatic flame temperature calculated by a one-dimensional flame calculation (Cantera). For the tube heater with the range of 300 - 900 K, there is a mean temperature deviation of 6.8 K between the thermocouple measurements and the temperatures determined by CARS. This corresponds to a systematic error of 0.5 - 2.2 % as shown in Fig. 5.5 (right). Figure 5.5 (left) shows the temperature measured 10 mm above the flat flame burner exit and calculated by the one-dimensional simulation. The resulting deviation from the reference temperatures are summarized in Fig. 5.5 (right). The deviation of the measured values from the simulation on the lean side ($\phi < 0.9$) is less than 3 K. Then the deviation increases with increasing equivalence ratio up to 48 K. These deviations correspond to errors of 0.2 - 1.3 %. It should be noted that in the simulation no radiation losses are corrected, which causes a reduction of the maximum temperature in the sim-

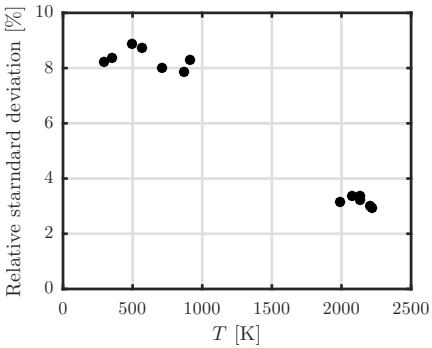

Figure 5.4. Relative standard deviation of CARS measurements at different temperatures. The measured values 300 - 900 K are determined in the flow of a tube heater and the other measured values in the exhaust gas region of a flat flame burner at different equivalence ratios. Statistics are based on 400 samples.

ulation. The radiation losses also increase with the fuel/air ratio. Therefore, the expected systematic error is well below the values as shown in Fig. 5.5.

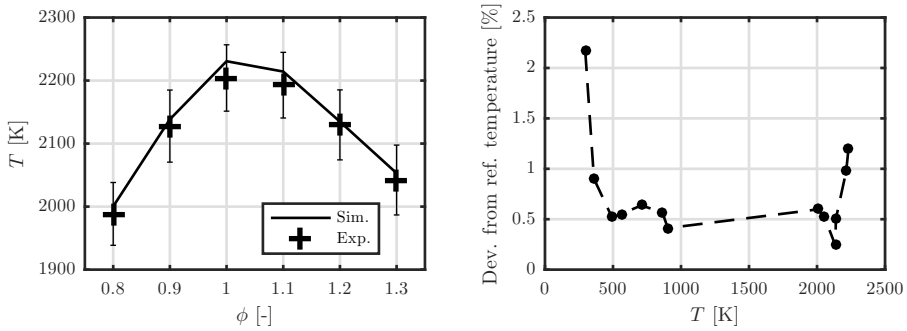

Figure 5.5. Accuracy measurement of the CARS system. Left: Upper temperature range, measured in a flat flame. Also shown is the comparison between the measured and calculated temperature of the flat flame. Right: Deviation from the reference temperatures as a function of the temperature.

5.1.2 CO-LIF

5.1.2.1 Optical setup

For the measurement of CO-concentrations, quantitative CO-LIF using two-photon excitation is applied. The $B^1\Sigma^+(v' = 0) \leftarrow\leftarrow X^1\Sigma^+(v' = 0)$ transition of CO is excited at 230.1 nm [94, 120]. The emission is detected within the Angström-Bands $B^1\Sigma^+(v' = 0) \rightarrow A^1\Pi(v'' = 1)$ at around 485 nm. For excitation, a pulsed dye laser (Sirah Lasertechnik, Precision Scan) with Pyridine 1 dissolved in ethanol is pumped by the second harmonic of a Nd:YAG laser (Spectra-Physics, Quanta Ray GCR-4) operated at 10 Hz. The final UV laser beam at 230.1 nm is generated by frequency mixing the second harmonic at 345 nm with the fundamental of the dye laser radiation output at 690 nm. The UV beam is directed into the probe volume via several mirrors and focused with a $f = +300$ mm spherical lens.

To spatially overlap CARS and CO-LIF beams, a pin-hole target with a diameter of 100 μm is placed on the burner nozzle. This target is moved in the y-z plane until all three CARS beams pass through the pin-hole without any disturbance. The CO-LIF beam is then directed through the pin-hole. For this purpose, a small mirror is placed directly behind the lens which focuses the CARS beams into the probe volume. If the CO-LIF beam passes completely through the pin-hole, the CARS and CO-LIF beams are superimposed in the measurement volume.

For the correction of the LIF signal intensity with the pulse energy of the laser, an energy meter (Coherent, EnergyMax) is located behind the first mirror. The data of

the energy meter are recorded for each pulse and converted into the corresponding value in mJ.

CO fluorescence is collected using a combination of an achromatic lens (f = + 160 mm) and a 100 mm $f/2$ macroscopic objective lens (Carl Zeiss, Makro Planar T * 100/2), and recorded by an intensified CCD camera (Princeton Instruments, PI-MAX 2). For the acquisition of in situ background images, the camera is operated at 20 Hz while the laser system's repetition rate is fixed at 10 Hz. A band-pass filter centered at 485 nm is used to suppress interferences from the C_2-Swan bands. Interfering flame luminosity is additionally reduced by a 50 ns camera gate that is synchronized with the laser pulse. For the evaluation, only the fluorescence in the focus area of the excitation laser beam is of interest. Therefore, only a small part of 120 (x) × 49 (z) pixels is used in the camera chip. This corresponds to a recording window of 2 (x) × 0.8 (z) mm^2. The 120 pixels in the x-direction are again combined into 5 pixels (binning).

The dependency of the CO-LIF signal on temperature, wall-distance and laser energy is taken into account for in a calibration procedure outlined in [99, 100], and briefly described in the following section.

5.1.2.2 Data evaluation

Extraction of measurement area

The applied CO-LIF measurement technique is a zero-dimensional point-wise measurement. However, the fluorescence is detected with a two-dimensional camera sensor and is subsequently converted to point-wise information. The slightly moving laser-focus area due to the flame fluctuation can be extracted from the two-dimensional LIF image. The procedure, especially for LIF measurements in the vicinity of surfaces, has great advantages over a zero-dimensional detector.

To evaluate the local fluorescence intensity corresponding to the zero-dimensional measurement point, a control area is extracted from the recorded raw image (see Fig. 5.6, left). In the beam direction (x-direction), the focal point of the laser is in the middle binned-pixel column. To limit the control area, the three inner binned-pixel columns are used and integrated in the x-direction. This corresponds to a measurement length of approximately 1.2 mm. In the beam normal direction (z), the center of gravity of intensity integrated in the x-direction (see Fig. 5.6, right) is calculated. The ±5 binned-pixels in z-direction (150 μm) from the calculated center of gravity are used for further integration. The calculated value finally represents the measured fluorescence intensity I_{LIF} of the control area. Beam steering may deflect the exciting laser beam out of the measurement area. In this case, the

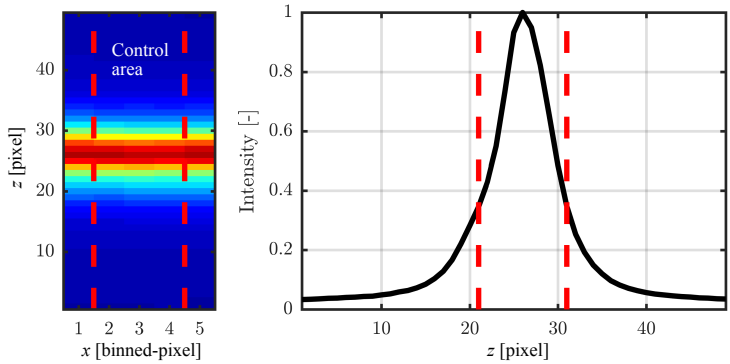

Figure 5.6. Extraction of the CO-LIF measurement volume. Left: Raw image of the fluorescence with the control area drawn in the beam wise direction. Right: Mean intensity curve of the fluorescence with marked integration range in the beam normal direction.

center of gravity of the integration area in the raw image shifts up or down in the z-direction.

Calibration

As mentioned in Section 3.3.3, Eq. (3.23) allows a quantitative determination of the concentration of species in fluids using the LIF method. The direct way would be a determination of all the relevant coefficients of the equation and the subsequent calculation of the CO concentration from the measured fluorescence intensity. In reality, this is not possible due to many external influencing factors. Instead, a specific calibration of used measurement system is generally applied. In this work, the procedure developed in [100] is used. A formula for calculating the CO concentration, X_{CO}, can be derived from the LIF intensity, I_{LIF}, as,

$$X_{\mathrm{CO}} = (I_{\mathrm{LIF}} - I_{\mathrm{BG}}) \cdot \frac{1}{a \cdot E_{\mathrm{Laser}}^{b}} \cdot \frac{T}{T_0} \cdot C_{\mathrm{Geo}}(y) \cdot C_{\mathrm{CO_T}}(T, \phi) \cdot C_{\mathrm{Cal}}. \tag{5.1}$$

All of the variables used in Eq. (5.1) and the calibration procedure will be explained in the following part and are summarized in Fig 5.7.

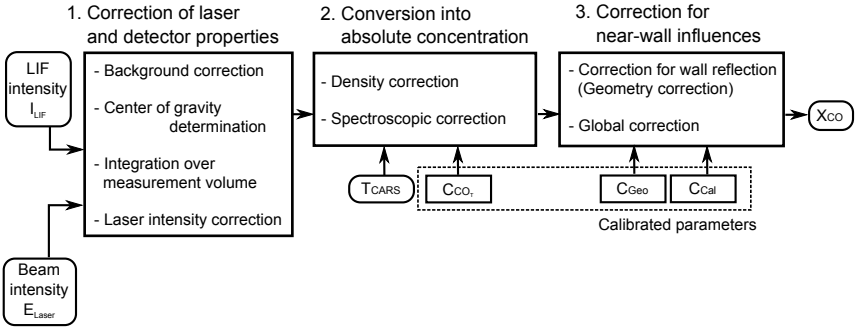

Figure 5.7. Flow chart for the calculation of absolute CO concentrations.

Laser-energy correction

The first step in the correction of laser and detector properties is to subtract the background of the individual raw image. The background images are recorded between two LIF signal images. According to Eq. (3.23), the fluorescence intensity in a two-photon process depends quadratically on the laser intensity. However, as a result of the occurrence of induced competing processes, this usually deviates from the quadratic relationship and the exponent b ([-]) of the dependence in Eq. (5.1) becomes smaller than 2. To determine this dependence, the LIF emission is recorded in a 1 % CO test gas mixture in nitrogen at different laser intensities. For this purpose, the laser is attenuated by a mixture of ethanol (with MEK[1]) dissolved in distilled water with different concentrations. An exponent of $b = 1.26$ is determined for the present experimental setup.

Density correction

For the quantitative measurement of a species by means of LIF, a density correction is always necessary. Without this correction, only the particle number density of the excited gas can be determined. In turbulent flows, it is additionally necessary to measure the temperature simultaneously. In this experiment, this is done by means of the information from the CARS data. With the ideal gas law ($\varrho \propto 1/T$), the measured particle number density can be corrected by a reference temperature T_0.

[1] MEK: Methyl Ethyl Ketone. Some commercial products of ethanol is denatured with MEK, which absorbs the UV laser.

Spectroscopic correction

Regardless of the density correction described above, the measured fluorescence signal is significantly dependent on the temperature of the excited molecule. As the combustion progresses, the temperature rises and more molecules are in the excited state. At the same time, the lower gas density with increased temperature changes the number of possible collision partners in the measurement volume. Since the possibility of collision depends not only on the number of impact partners but also on the property of the mixture, the equivalence ratio must also be taken into account.

Using a 1 % CO test gas diluted by nitrogen, the temperature dependence of the fluorescence in the range between 300 K and 900 K is investigated. The test gas is heated with a tube heater and the temperature is determined by means of the simultaneously recorded CARS data. In addition, the influence of the temperature and mixture composition is determined by using the flat flame burner operated with three different equivalence ratios (ϕ = 0.83, 1.0, 1.2) for the high-temperature range. The equilibrium CO concentrations and temperatures of the three flames are determined by a one-dimensional flame calculation (Cantera). Subsequently, the measured LIF intensities of the test gas and flat flame are corrected by the procedures previously outlined for *laser-energy correction* and *density correction*. After these corrections, the relative fluorescence per CO content is calculated. Thus, three stoichiometry and temperature-dependent calibration curves of the factor C_{CO_T} (T, ϕ) ([-]) result in the correction of spectroscopic effects.

Figure 5.8 shows the measured relative CO-LIF intensity combined with a piecewise cubic polynomial ($= C_{CO_T}^{-1}$). In the lower temperature range, all three curves follow each other, since they are measured with the test gas with no difference between stoichiometries. For higher temperatures, the CO fluorescence shows a significant dependence on the gas partners existing in the mixture. The leaner the mixture becomes, the more the fluorescence is enhanced at high temperatures. Between the measurement points of the test gas and those from the flat flame, there is a relatively large gap without data. In this area, it is difficult to obtain data points because on one hand the available heaters, which can heat the test gas higher, are getting larger and more complex, and on the other hand, the exhaust gas temperature of the flame is determined by the equivalence ratio. For this reason, one support point has been added to each curve in Fig. 5.8 to prevent the overshooting of the polynomial.

This calibration method is based on the assumption that the fluorescence intensity in the temperature range of the tube heater is independent of the collision

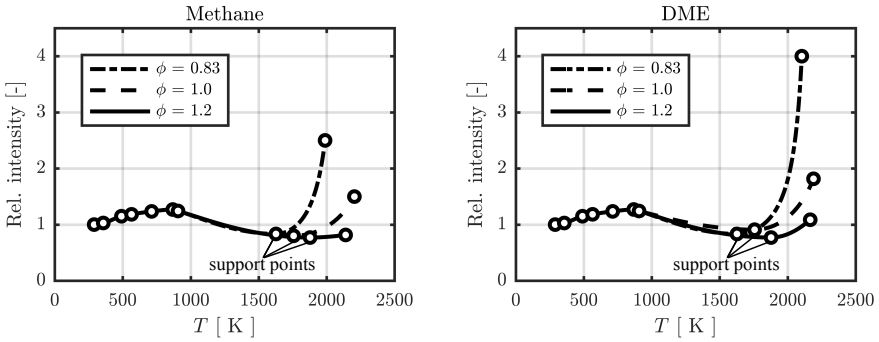

Figure 5.8. Relative CO-LIF intensity ($= C_{CO_T}^{-1}$) versus temperature as a function of stoichiometry. The measurement points and support points are linked by a piece-wise cubic polynomial.

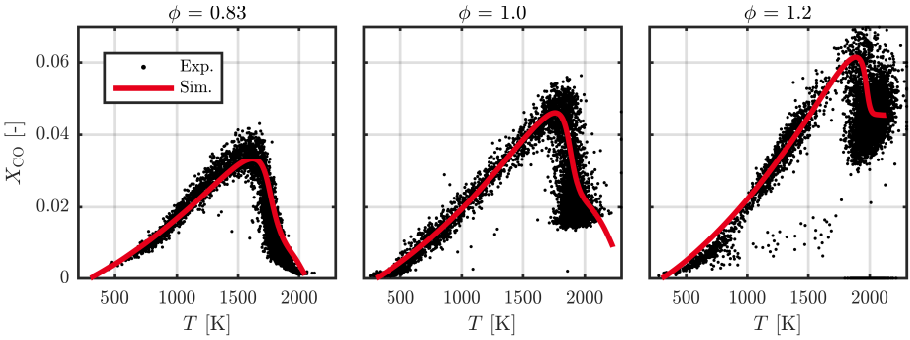

Figure 5.9. Comparison of the measurement of the free branch of the V-flame by means of CARS / CO-LIF (black dots) and a one-dimensional adiabatic flame calculation with Cantera (red line). The three measured flames with $\phi = 0.83$, 1.0 and 1.2 for methane/air mixture are shown.

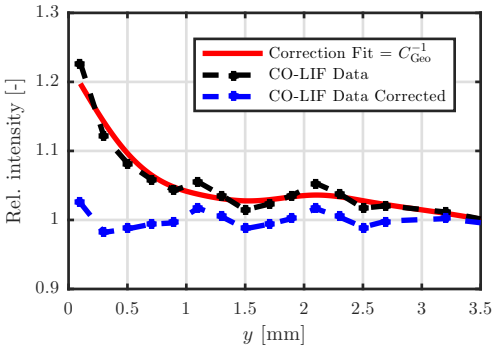

Figure 5.10. Influence of the wall on the recorded LIF intensity at different distances to the wall (black line), the calculated fit of the correction function (red line) and the processed LIF intensity after the applied correction (blue line).

partners. The temperature range of 300 - 900 K measured with the tube heater takes place only in the area of the flame quenching near the wall. To test this statement and also to optimize the position of the support points mentioned above, the three flame configurations are measured in the free branch of the SWQ burner using CARS and CO-LIF. In this area there is no interaction of the flame with the wall and an undisturbed premixed flame can be assumed. Figure 5.9 shows the comparison of the measurement with the one-dimensional calculation of a free flame (Cantera). It shows a good agreement of the measurement results with the calculation over the entire temperature range. The deviation from the reference temperature will be discussed in the evaluation of the accuracy.

Geometrical correction factor C_{Geo}

In the case of the near-wall LIF measurement, a geometry correction must be carried out, since shading and reflections can lead to a reduction or elevation of the LIF signal. For this purpose, measurements are also carried out with 1 % CO test gas at room temperature to investigate the influence from the wall on the signal level. The measured values are normalized to a reference value 10 mm away from the wall and the geometric influence is tabulated in the form of a correction map. The correction map is visualized in Fig. 5.10.

Global calibration factor C_{Cal}

For the final conversion of the LIF intensity into a concentration value, a global calibration factor, C_{Cal} ([-]), is determined. This includes experiment-dependent factors such as the size of the measurement volume, the transfer function of the imaging system (solid angle etc.) and the quantum efficiency of the detector. To determine this calibration factor, again a test gas with a mixture of 1 % CO in nitrogen at room temperature is used with the tube heater. After applying all previous correction factors, this results in a linear relationship between measured intensity, I_{LIF}, and CO concentration, X_{CO}, with a fixed scalar value, C_{Cal}.

5.1.2.3 Further analysis

For a detailed analysis of CO formation and oxidation of the near-wall flame, scatter plots of CO mole fraction versus temperature are presented. Measurement positions are fixed in space, independent of the instantaneous flame position. Note that due to the aforementioned Helmholtz resonances for laminar flames close to the wall, remaining fluctuations of the flame front position are observed. Thus, the flame is moving across the respective fixed probe volume. As a result, various thermochemical states of the flame can be observed in all CO/T scatter plots at a specific axial position z and wall distance y. Figure 5.11 presents a scatter plot for the data measured at $z = 48$ mm across the unbounded flame branch (no wall present, various y-positions) of a stoichiometric methane/air flame. Two branches are observed and are assigned to the CO formation zone and the CO oxidation zone. Scatter plots as shown in Fig. 5.11 will be used later on in section 5.3 to discuss the impact of wall temperatures, fuel types and turbulence upon thermochemical states.

5.1.2.4 Spatial and temporal resolution

As already described in the previous section, the field of view is placed around the focal point of the CO-exciting laser beam and the area for the evaluation (3 binned-pixel columns (binned in x-direction) × 10 pixel rows in z-direction) is automatically selected. In the beam-wise direction, the length of the measurement volume is thus set to 1.2 mm. In the beam-normal direction, the focus diameter of the laser beam is the limiting factor. This is determined by means of a beam monitor (DataRay, WinCam D) to be 150 μm (FWHM). This results in a measuring volume of approximately 150 μm × 150 μm × 1.2 mm. The temporal resolution is given by the laser pulse duration. This is detected by means of a photodiode and is

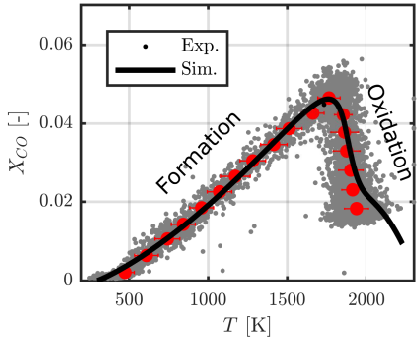

Figure 5.11. Thermochemical CO/T states measured at the free branch of the V-flame for methane with $\phi = 1$ (gray dots). Conditional average (red dots) of experimental data are compared to the results of a one-dimensional flame calculation of a freely propagating adiabatic flame (black solid line).

measured to be approximately 10 ns in this experiment. The system repetition rate is 10 Hz.

5.1.2.5 Precision and accuracy

The precision is given in the form of the relative standard deviation analogous to the consideration in the CARS method. The detected LIF signal in the exhaust zone of the flat flame is considered. The equivalence ratio of the flame is varied in order to cover different temperatures (1900 - 2200 K) and CO concentrations (0.07-6 %). The measured LIF signal is corrected to the absolute CO concentration with the above mentioned procedure without the geometrical correction. To evaluate the precision, the shot-to-shot (time) standard deviation is calculated and normalized with the absolute mean value. Figure 5.12 (left) shows the precision of approximately 4 - 6 %. Since the CO-LIF is corrected with single shot temperatures from CARS thermometry, the methodology applied here can not be more precise than that of CARS.

The precision of the measurement system near the wall must be also evaluated due to the applied geometric correction. For this purpose, a test gas with 1 % CO concentration passed through the nozzle of the SWQ burner with the wall present (no flame). Subsequently, the LIF signal is detected at different wall distances y and again the relative standard deviation is determined. Figure 5.12 (right) shows

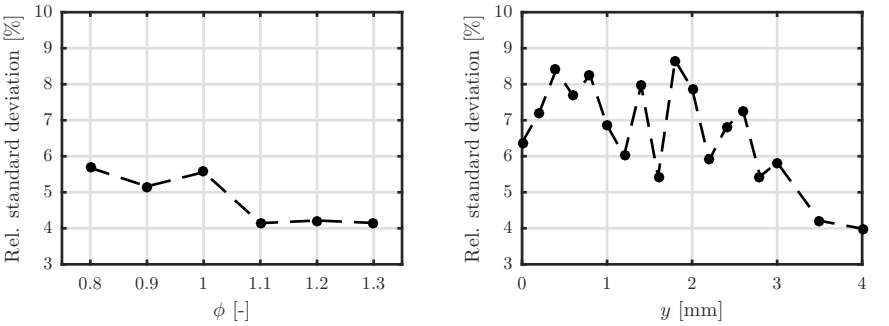

Figure 5.12. Left: Relative standard deviation of the CO-LIF system with the involvement of the CARS system (measured on the flat flame burner). Right: Relative standard deviation of the CO-LIF system near the wall, measured on the SWQ burner with a CO test gas. Statistics are based on 400 samples.

that the wall does not have a large influence on the precision. This varies from 4 to 8.5 % regardless of the distance between the measurement volume and wall.

The accuracy of the CO-LIF system can only be specified in combination with CARS. Essentially, the accuracy depends on the quality of the fit of the calibration polynomial (Fig. 5.8). The best way to quantify the accuracy of the measurement system is to take a flame in the CO/T state space as shown in Fig. 5.11. To determine the accuracy, the measured data are compared with the one-dimensional simulation of a flat flame. This is done by calculating the conditioning average for experimental data in the CO concentration direction with a window width $\Delta X_{\mathrm{CO}} = 0.004$, which is plotted as red dots in Fig. 5.11. It can be seen in Fig. 5.13 that in the temperature range of 600-1750 K, an accuracy of better than 5 % can be achieved. At very low and very high temperatures, however, the CO concentration is overestimated by up to 40 %. In these areas, however, the absolute concentration is also very low, so that even a small measurement error has a strong effect on the accuracy.

The influence of the wall on the accuracy is very difficult to quantify. This is because any interference with the wall has already been removed with the geometrical calibration.

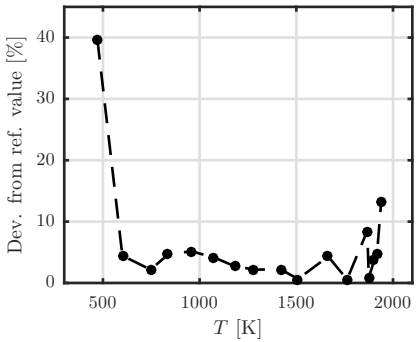

Figure 5.13. Deviation of the CO-LIF measurement from the reference CO concentrations in the case of $\phi = 1.0$ for methane/air mixture.

5.1.3 Phosphor thermometry (PT)

5.1.3.1 Optical setup

Using the lifetime method, phosphor thermometry enables semi-invasive and spatially resolved surface temperature measurements [70]. In this study, particles of the thermographic phosphor $Gd_3Ga_5O_{12} : Cr, Ce$ [72] (GGG) and a temperature resistant binder (ZYP Coatings, HPC Binder) are deposited to the wall surface as a thin line (1 mm broad) using an airbrush method. Its extension in the z-direction allows the recording of surface temperatures up- and downstream of the different quenching heights of the flames. A Q-switched frequency-quadrupled Nd:YAG laser (Spectra-Physics, Quanta Ray INDI, 10 Hz repetition rate) operating at a wavelength of 266 nm is used as an excitation source. The laser-pulse energy is adjusted by a combination of a half-wave plate and polarizing beam splitter cube. For shaping the laser beam, a beam homogenizer (Holo Or, HM-201-WYA) is used to convert the Gaussian laser beam profile into a top hat one.

After the excitation, the temperature-dependent phosphorescence decay is detected with a high-speed CMOS camera (Photron, FASTCAM SA-X2) equipped with a 105 mm objective lens. A $f\# = 5.6$ is used to ensure both a sufficiently high depth of field and signal intensity. A band-pass filter (550 to 2700 nm) is positioned in front of the camera to reduce noise derived from lasers and flames. The image size is 48 × 128 pixels, corresponding to an area of 3.2 (x) × 8.5 (z) mm^2 on the wall surface. The CMOS camera is operated at 480 kHz such that each

waveform of the temporally decaying phosphorescence is recorded by a sequence of 750 images. The camera trigger starts 50 images prior to the laser's Q-switch trigger.

5.1.3.2 Experimental setup for calibration

To determine the characteristic decay time for each temperature, the phosphorescence is recorded under defined boundary conditions at different known temperatures. For the calibration, the phosphor is coated on a test plate made of heat-resistant stainless steel and the plate is fixed in a sample holder (see Fig. 5.14). During the calibration measurements, the direct contact between the sample holder and the reference thermocouple of type N is guaranteed. In order to investigate the temperature dependence of the decay time, the entire sample holder is placed in a tube furnace (Carbolite GmbH, CTF 12/100/900, D = 105 mm, L = 900 mm, $T_{\max}$ = 1473 K) and heated. The reference thermocouple is used for the temperature control.

For the excitation and detection systems, i.e. laser, camera and optics (except for an additional mirror in front of the camera) are same as the setup used in the measurement, which is described in the previous section. The additional mirror is used to match the distance between the measured surface and camera during both the calibration and the measurement.

5.1.3.3 Data evaluation

To correct the distortion of the recorded images, the combination of a dot target (LaVision, Type 7) and a target-based dewarping algorithm (Lavision, DaVis 8.3) is used. For the background correction, the average intensity of the first 45 images of each loop is used. All images are corrected pixel-wise for nonlinearity of the CMOS chip, based on the procedure presented in [186].

The uniqueness of the decay curve can be ensured for mono-exponential manner and characterized by the decay time, τ, determined with the algorithm described in [26]. The measured decay curve can be described as

$$I(t) = I_0 \exp\left(-\frac{t}{\tau}\right) + I_{\text{offset}}. \tag{5.2}$$

I_{offset} is the time average of the signal intensity before the excitation, i.e., the background. Figure 5.15 shows the time-resolved normalized signal intensity of a single shot and the mono-exponential fit. When calculating the decay characteristics, a fit window is determined by

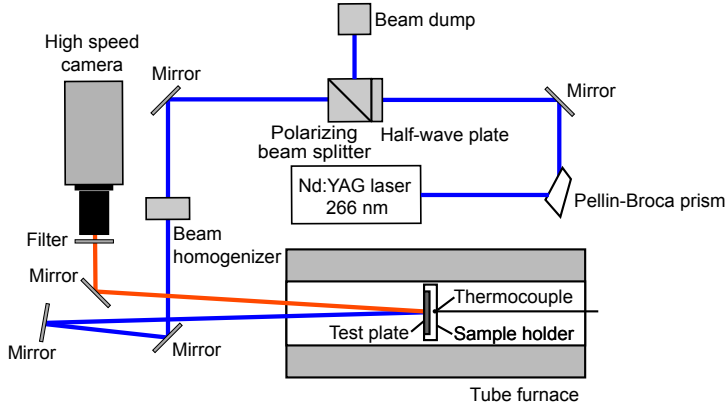

Figure 5.14. Overall design for the temperature calibration of the thermographic phosphor, consisting of frequency-quadrupled Nd:YAG laser, optics, detection system and the coated sample in the tube furnace.

$$\begin{aligned} t_1 &= t_0 + c_1 \cdot \tau, \\ t_2 &= t_0 + c_2 \cdot \tau, \end{aligned} \tag{5.3}$$

which is limited and dependent on the decay time τ and the constants c_1 and c_2. Because τ is not known at the beginning, a starting value is determined as $\tau_0 = c_0 \cdot \Delta t$, which depends on the length of the recording window, Δt, and the constant, c_0. The decay time is finally determined by iterative steps and the final constants are kept for both the calibration and measurement. To evaluate the decay processes of $Gd_3Ga_5O_{12} : Cr, Ce$, the constants as follows are used: $c_0 = 0.05$, $c_1 = 0.5$ and $c_2 = 4.0$.

Figure 5.16 shows the temperature/decay time characteristics derived from the calibration. Each data point represents the temporal and spatial mean values of 75 sequences and 20 × 20 pixels corresponding to the average of 30000 individually evaluated decays. During the measurement, temperatures corresponding to the recorded decay curve in each pixel can be determined by a comparison with this dependency. Temperatures are binned in the horizontal x-direction such that quasi-instantaneous one-dimensional temperature profiles are achieved in the axial z-direction.

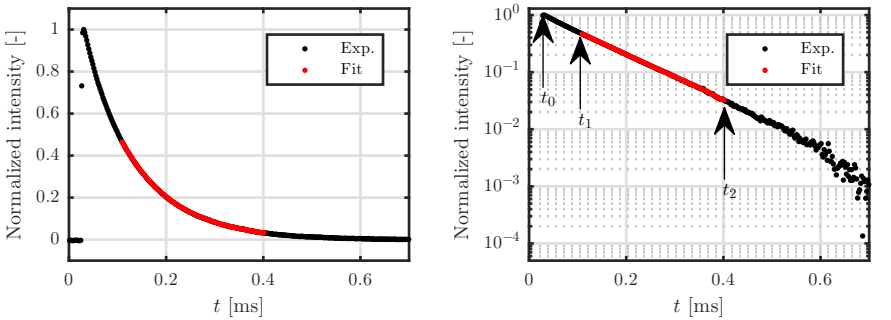

Figure 5.15. Normalized decay of $Gd_3Ga_5O_{12}:Cr,Ce$ at 373 K at a pixel of the camera with a linear- (left) and a logarithmic- (right) horizontal axis. The mono-exponential fit ($c_1 = 0.5$, $c_2 = 4.0$) curves are also shown (red).

5.1.3.4 Spatial and temporal resolution

The field of view for phosphor thermometry is placed at the area of interest (48 × 128 pixels corresponding to 3.2 (x) × 8.5 (z) mm^2) and binned in the horizontal (x) direction. This results in a quasi-instantaneous measurement in the axial (z) direction. The temporal resolution is given by the repetition rate of the excitation laser which is synchronized with CARS/CO operated at 10 Hz, and the decay time of used phosphor $Gd_3Ga_5O_{12}:Cr,Ce$, which is in the order of 10 - 100 μs.

5.1.3.5 Precision and accuracy

In order to evaluate the precision of the PT system, the data recorded during the calibration is considered. The relative standard deviations in time and space are shown in Fig. 5.17. The temporal (shot-to-shot) and spatial (fluctuations in space) standard deviations of the temperature at the calibration points are between 1.0 K and 7.5 K, resulting in a relative standard deviation of 0.15 to 3.2 % over the measured temperature range (300 K – 800 K). The system accuracy of PT is not given here because it requires the reference temperature of the target surface which is not taken in this work.

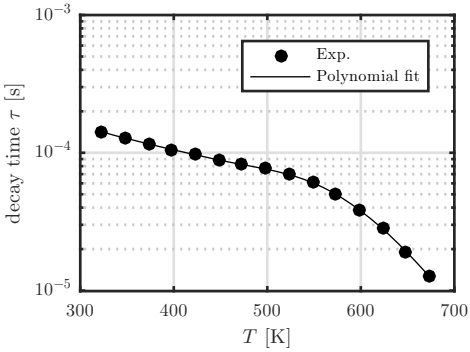

Figure 5.16. Calibration curve of $Gd_3Ga_5O_{12}$: Cr, Ce recorded in the tube furnace.

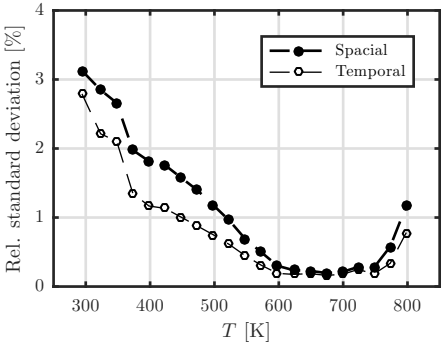

Figure 5.17. Relative standard deviation of the calculated temperature at the calibration points.

5.1.4 OH-PLIF

5.1.4.1 Optical setup

For the flame front detection using planar OH-LIF imaging, a dye laser (Sirah Lasertechnik, Double Dye) is tuned to 282.9 nm (after frequency doubling) to excite the $Q_1(6)$ line of the $A^2\Sigma^+(v' = 1) \leftarrow X^2\Pi(v'' = 0)$ transition [49] of the OH radical marking the burned gas region. As dye, Rhodamine 6G dissolved in ethanol is used. The dye laser is pumped by a frequency-doubled Nd:YAG laser (Spectra-Physics, Quanta-Ray, PIV 400, only one cavity used) operated at 10 Hz. The pulse energy at this wavelength is reduced to $\approx$ 2 mJ due to excessive reflections of the laser beam on the wall. Using a combination of cylindrical lenses (f = -50 and +300 mm), the laser beam is shaped to a laser sheet and focused with another cylindrical lens (f = +600 mm) to an approximately 150 μm sheet in the probe volume. The laser beam is normal to the burner wall oriented, but tilted by about 30° to the exit plane of the nozzle because of the limited accessibility of the burner. The resulting laser sheet is arranged to include the focal point of the CARS and CO-LIF laser beams.

The OH-PLIF emission ($\approx$ 308 - 313 nm) is detected perpendicularly to the laser light sheet using a band-pass filter (Laser Components, UV-B, 308±10 nm, transmission > 80 %), a UV-transparent lens (f = 150/2.5, Halle), an image intensifier (LaVision, IRO) and a CCD camera (LaVision, Flowmaster). The region of interest (ROI) is resolved by 768 × 1088 pixels on the camera sensor, recording an area of 10.6 × 15 mm^2. Because of the limited optical access, the detection and excitation systems are tilted relative to the y-direction by an angle of 30° (see Fig. 5.1).

5.1.4.2 Data evaluation

For the background correction, ensemble-averaged background images are subtracted from individual LIF images. Before each operating condition, a series of 50 individual images of the background signal is recorded. These background images are taken both with laser operation in the absence of the flame and without laser operation in the existence of the flame. The mean background image is then subtracted from each individual signal images, thus the influences by the flame chemiluminescence and the other fluorescence of the wall contamination due to the laser sheet can be removed. To correct the distortion of the camera images, the combination of a dot target (Type 7, LaVision) and a target-based dewarping algorithm (LaVision, DaVis 8.3) are used.

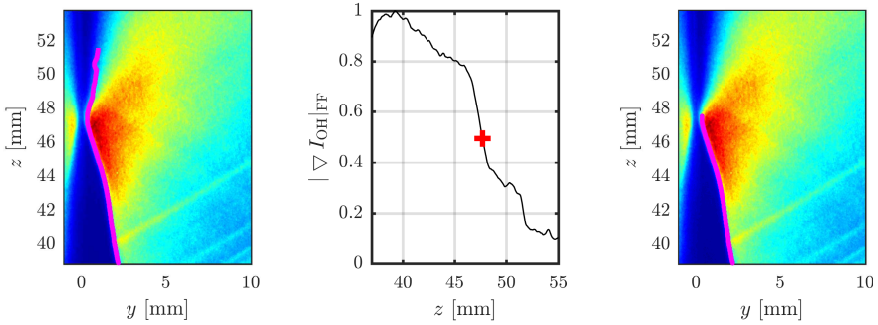

Figure 5.18. Detection of the flame front and the flame quenching point in a laminar configuration of the SWQ burner. Left: raw image of the OH-LIF with the detected path of the steepest OH gradient by a Canny-edge filter (magenta line). Center: profile of the amount of OH Gradients along the path of the steepest OH gradient. Right: resulting flame front with quenching point (magenta line).

For each OH image, flame fronts are extracted using a Canny edge filter [30]. Figure 5.18 (left) shows an example of a recorded OH raw image of the FWI zone for a laminar methane/air flame. The detected flame front is marked as a red line (already spatially calibrated and normalized). For the definition of the quenching point, a similar procedure as the one outlined in [99, 100] using the OH gradient field is applied as follows.

The absolute value of the flame-normal OH gradient, $|\nabla I_{\mathrm{OH}}|_{\mathrm{FF}} = |\delta I_{\mathrm{OH}}/\delta x_{\mathrm{normal}}|$, is determined along the detected flame front. For normalization, the maximum value of the flame-normal OH gradients is used. Figure 5.18 (center) shows the extracted curve of $|\nabla I_{\mathrm{OH}}|_{\mathrm{FF}}$ along the determined flame front over the axial position, z. $|\nabla I_{\mathrm{OH}}|_{\mathrm{FF}}$ decreases rapidly when approaching the quenching point. Here, flame quenching is defined at that axial position where the normalized OH-gradient decreases to 0.5, which is derived from [97]. At sections below the threshold, the flame is considered quenched and the flame front no longer exists. Figure 5.18 (right) shows the flame front resulting from this procedure.

5.1.4.3 Spatial and temporal resolution

The spatial resolution of the OH-LIF system depends on the optical resolution of the camera and image intensifier system. In general, the properties of the image

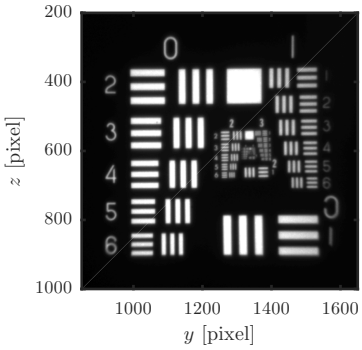

Figure 5.19. Recorded image of the USAF 1951 target.

intensifier are the limiting factors in the resolution. The optical resolution is often determined by means of the following contrast transfer function (CTF) [66].

$$\mathrm{CTF} = \frac{I_{\max} - I_{\min}}{I_{\max} + I_{\min}} \tag{5.4}$$

The contrast transfer function is a measure of the ability of an optical system to display contrast differences at a particular local resolution. For determining the CTF of the optical detection system, a USAF 1951 resolution target is placed at the probe volume. The resolution target has a series of bar patterns of decreasing size (Fig. 5.19). This target contains numbered bar groups consisting of six test target elements. The change of the spatial frequency of these elements is on a geometric progression based on the sixth root of 2.

The results of these measurements are given in Fig. 5.20 (left) as the intensity profile through the selected bar group (group 1). The CTF is derived from the profile as shown in Fig. 5.20 (right) with given spatial frequencies [lp(line pairs)/mm]. To obtain the value of the spatial resolution, the spatial frequencies at contrast values of 26.4 % (Rayleigh criterion) are determined. The spatial resolution is given as $k = 3.3$ lp/mm which corresponds to $s = 303$ μm. Conversion from [lp/mm] to [μm] is achieved according to $s = 1000\ /\ k$ μm.

The temporal resolution is given by the laser pulse duration. This is detected by means of a photodiode and is measured to be approximately 9 ns in this experiment. The system repetition rate is 10 Hz.

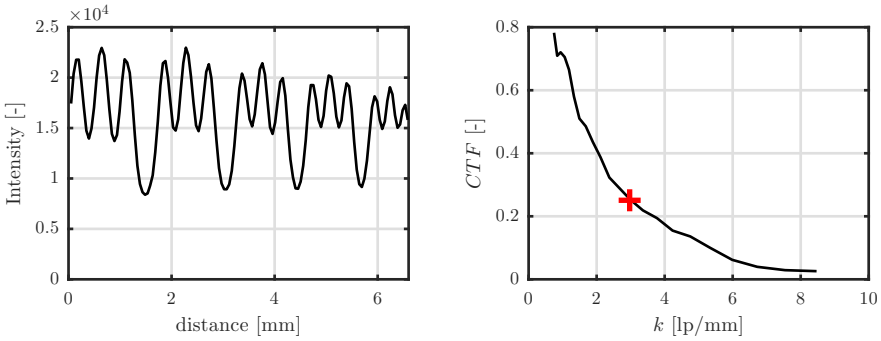

Figure 5.20. Determination of the spatial resolution of the OH-LIF detection system. Left: The intensity profile of the line scan for the group 1 in the USAF 1951 target. Right: Computed Contrast Transfer Function (CTF) and the corresponding resolution limit (+) of the detection system used in this work.

5.1.4.4 Precision and accuracy

The precision of the OH-LIF system can be determined using the free branch of the laminar V-flame. For this purpose, the flame front is extracted directly in the vicinity of the flame holder. In this area, the acoustically induced vibrations of the flame front in the interaction zone only play a minor role and the flame burns stationary. The fluctuation of the detected flame front position can give a minimum deviation of the measurement system. However, it cannot be determined whether the remaining fluctuations come from the flame characteristics. Figure 5.21 shows a section of the mean flame front and the associated horizontal fluctuations of the flame front position (shot-to-shot standard deviation). The averaged deviation is around ± 50 μm, which corresponds to an estimation of the precision.

Accuracy of OH-LIF measurements in terms of the flame-front detection would be possible by the comparison of a reference position of the flame front with that derived from simulation. This can be done, for example, by means of a DNS calculation of a simple flow configuration, but would go far beyond the scope of this work. For this reason, it is not necessary here to specify an accuracy of the measurement.

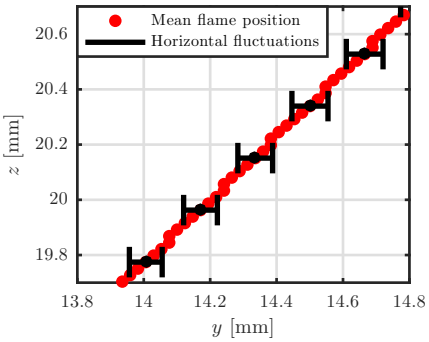

Figure 5.21. The standard deviation of the detected flame front position at a section of the free branch of the V-flame. The detected mean position of the flame front (red dots) and corresponding horizontal fluctuations in the position determination (black error bars) are shown.

5.2 Results and discussion for wall heat flux

The results presented in the following section are based on those already published in [113].

5.2.1 Global overview of V-flame

For different wall temperatures and both investigated fuels, ensemble-averaged flame front positions of laminar flames derived from OH-LIF images are presented in Fig. 5.22. Quenching heights are located at the highest point of each line that represents the ensemble-averaged flame front position. Varying wall temperatures significantly impact quenching heights. Increasing the wall temperature from 330 to 670 K, the quenching height decreases considerably. For methane/air and DME/air flames, the quenching points move upstream by 2 and 1.5 mm. For DME flames, the overall quenching heights are lower compared to those of methane flames, owing to a larger laminar flame speed [121].

5.2.2 Temperature profiles

Figure 5.23 shows ensemble-averaged axial profiles of the gas phase (top) and wall temperatures (bottom) for flames at laminar flow conditions. The gas temperature profiles are measured at a fixed position from the wall at the wall-normal y =

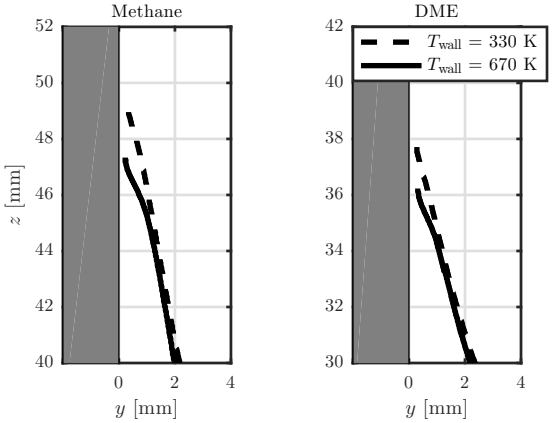

Figure 5.22. Ensemble-averaged positions of the flame front during side-wall quenching for methane and DME with $\phi = 1$ and wall temperatures, T_{wall}. The grey rectangle ($y < 0$ mm) marks the position of the wall. Notice that the axial scales are different for both fuels because the respective quenching zones for methane and DME flames are located 10 mm apart from each other.

100 μm (wall-closest position). The profiles have been obtained by traversing the burner assembly in the axial z-direction, starting upstream of the quenching point and ending in the post-flame region, after passing the quenching zone. For increasing wall temperatures, the location of the maximum gas temperature moves upstream and peak temperatures increase. The z-position of the peak temperature is related to the axial location where quenching occurs. Consistent with the observations presented in Fig. 5.22, DME/air flames are quenched further upstream than methane/air flames. Higher wall temperatures cause increased temperatures of the yet unburned gasses within the laminar boundary layer. This behavior is expected from inspecting gas temperatures measured upstream of the quenching points. Higher initial temperatures of the unburned gas mixtures cause an increased laminar burning speed [85]. Thus, for elevated wall temperatures the flame burns closer to the wall and the quenching distance is reduced.

In Fig. 5.24, selected ensemble-averaged profiles of gas phase temperatures are shown in the y-direction for $T_{\text{wall}} = 330$ K and 670 K, respectively. A set of 400 data points is recorded. Measurements shown are performed at three different z-positions, starting at the wall ($y = 100$ μm) and ending in the exhaust gas region ($y = 4$ mm) after passing the main reaction zone, i.e., the flame front.

Upstream of the quenching point (i.e., $z = 48.5$ mm for the methane/air flame, $T_{\text{wall}} = 330$ K), the temperature profile closely matches that of an unbounded flame.

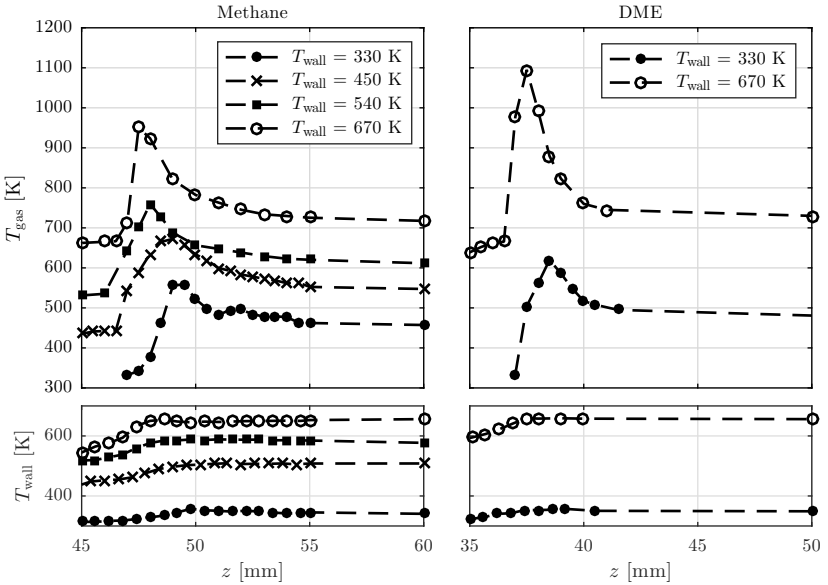

Figure 5.23. Axial profiles of ensemble-averaged gas phase temperatures at $y = 100$ μm (top) and wall surface temperatures (bottom). Data for stoichiometric methane/air flames are displayed on the left and for stoichiometric DME/air flames on the right. Statistics are based on 400 samples.

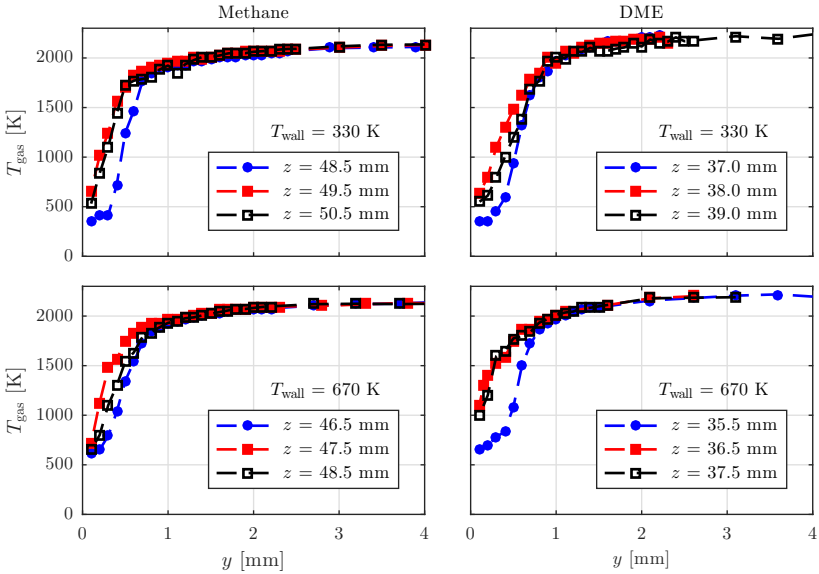

Figure 5.24. Wall-normal profiles of ensemble-averaged gas phase temperatures for wall temperatures of 330 K (top) and 670 K (bottom). Data for stoichiometric methane/air flames are displayed on the left and for stoichiometric DME/air flames on the right.

Low temperatures associated with unburned gas mixtures are located close to the wall, whereas at larger wall distances the gas phase temperature increases, approaching adiabatic flame temperatures (2220 K for methane, 2290 K for DME). At the quenching position, gradients of the wall-normal temperature profile are at maximum. Downstream of the quenching point heat release rates approach zero [141] and the profiles flatten due to diffusion processes. Although these temperature profiles show a similar shape independent of the fuel, some differences are observed. These differences are at least in part due to the fact that the axial positions relative to the actual quenching point are slightly different.

5.2.3 Wall heat fluxes

Ensemble-averaged wall heat fluxes are estimated by assuming one-dimensional heat conduction,

$$\dot{q} = -\lambda \frac{\partial T_{\text{gas}}}{\partial y} \tag{5.5}$$

with λ being the thermal conductivity and $\partial T_{\text{gas}}/\partial y$ the temperature gradient in the wall-normal direction. One-dimensional heat conduction is justified because wall-normal temperature gradients in the gas phase are significantly larger than temperature gradients along the wall. $\partial T_{\text{gas}}/\partial y$ is deduced from the ensemble-averaged gas phase temperatures measured at $y = 100$ μm and wall temperatures recorded at the respective axial height. Values for the thermal conductivity λ are calculated for an equivalence ratio of 1.0 and gas phase temperatures at $y = 50$ μm, resulting from linear interpolation between the wall temperature and gas temperature measured at $y = 100$ μm. Effects due to differential diffusion are assumed to be of minor importance compared to large heat conduction and hence here neglected. Chemical reactions on and close to the wall are as well assumed to be of minor significance on the estimated value of the thermal conductivity. Using these assumptions, the surface-normal heat flux equals the wall heat flux at the gas-solid interface.

The resulting heat flux for laminar flow conditions is shown in Fig. 5.25. Peak heat fluxes for the case of $T_{\text{wall}} = 330$ K for the methane flame agree well with the earlier measurements in [99, 100] using temperature gradients solely from gas phase thermometry and those reported in Boust et al. [20] for comparable flames within a side-wall quenching configuration. During flame quenching, the maximum wall heat flux is observed to be larger for higher wall temperatures. This counter intuitive result is caused by higher peak temperatures appearing closer to the wall (compare Fig. 5.24) which finally results in steeper temperature gradients. Approaching the post-flame region, increasing wall temperatures show contrary effects. As expected for hot flows without any heat release due to chemical reactions, heat fluxes decrease for increasing wall temperatures.

5.2.4 Quenching distances

In a previous experimental determination of quenching distances, δ_{Q} (horizontal y-distance between wall and flame front at the axial z-position of quenching), Boust et al. [18] used the disappearance of chemiluminescence signals near the wall. Within numerical studies, Poinsot et al. [141] deduced the quenching distance by the location of the maximum heat flux. Mann et al. [126] as well as Popp and Baum [144] determined the quenching distance from the closest separation between a specific isothermal contour representing the flame front and the wall.

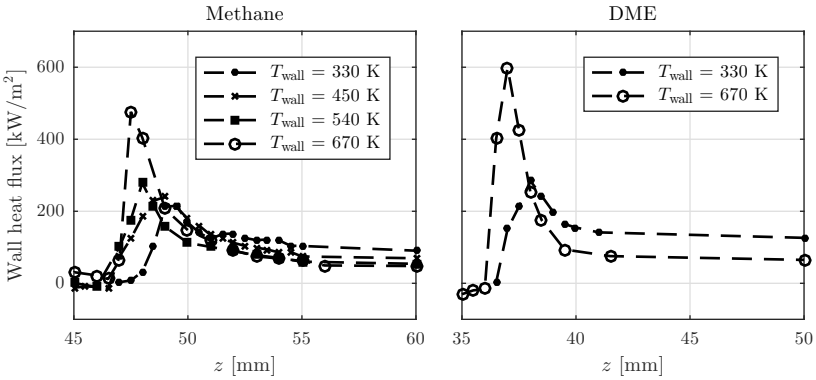

Figure 5.25. Ensemble-averaged axial profiles of the estimated local wall heat flux. Left: Stoichiometric methane/air flames. Right: Stoichiometric DME/air flames.

The isothermal contour was chosen coincident with the highest gradient of the heat release rate, which is a suitable definition of the flame front location [126]. For stoichiometric flames and fresh gas temperatures of 293 K, the corresponding isothermal contour is at 1450 K for methane and 1410 K for DME, as determined by the laminar flame calculations described in section 4.3.

For the laminar methane/air flame and a wall temperature of $T_{\text{wall}} = 330$ K, the axial profile of wall heat flux is compared to the flame front position extracted from the isothermal contour in Fig. 5.26. Considering the corresponding data from Fig. 5.25, the wall heat flux rises with increasing z-direction, until a maximum is reached at $z = 49.5$ mm. Further downstream, it drops again towards the post-flame region. According to the definition by Poinsot et al. [141], the axial position of quenching is located at $z = 49.5$ mm. On the other hand, using the isothermal contour at 1450 K, the position of the flame front is deduced from the data presented in Fig. 5.24. Analyzing Fig. 5.26, the axial position of quenching is consistently identified at $z = 49.5$ mm for both approaches. Additionally, this axial position coincides fairly well with the quenching height extracted from the OH-LIF imaging (see Fig. 5.22). Similar profiles are obtained for the other wall temperatures and fuel types. In all cases, the axial height of the minimum wall distance corresponds to the location of the maximum wall heat flux. Hence, the quenching distance, δ_{Q}, is deduced from the isothermal line closest to the wall. For the case shown in Fig. 5.26, the quenching distance is approximately 0.37 mm which agrees well with other findings using the side-wall configuration [87].

The relation between the ensemble-averaged maximum wall heat flux and quenching distance is shown in Fig. 5.27 (left) for varying wall temperatures and fuel types in laminar flames. To enable a comparison with results from the literature, the values are normalized with the characteristic heat release rate for a steady freely propagating laminar flame, termed “flame power”:

$$\widehat{\dot{q}} = \frac{\dot{q}}{\varrho \cdot s_{\mathrm{L}} \cdot c_{\mathrm{p}} \cdot (T_{\mathrm{ad}} - T_{\mathrm{u}})}. \tag{5.6}$$

Here, ϱ denotes the density of the unburned gas mixture, s_L is the laminar flame speed and T_u represents unburned gas temperatures measured at $y = 100$ μm. c_p represents the specific heat capacity per unit mass. The wall heat fluxes for $T_{\mathrm{wall}} = 330$ K shown in Fig. 5.27 (left) agree well with other findings [144]. As expected, maximum wall heat fluxes at the quenching location increase with higher wall temperatures for both fuel types, whereas the influence of the fuel type is less significant for wall heat fluxes normalized by flame power. Approaching the post-flame region shown in Fig. 5.27 (right), increasing wall temperatures have the opposite effect, expected for non-reacting hot flows.

The maximum wall heat flux during quenching is related to the closest distance of the flame to the wall. One model was proposed by Vosen et. al [182] based on the correlation between the quenching distance, δ_Q, and the maximum wall heat flux, $\dot{q}_{\mathrm{max}}$ by

$$\delta_{\mathrm{Q}} = \frac{\Delta T_{\mathrm{f}} \lambda}{\dot{q}_{\mathrm{max}}} \tag{5.7}$$

where ΔT_{f} is the temperature difference across the flame and λ is the thermal conductivity of the fuel/air mixture nearby the wall. Here, ΔT_{f} is deduced from the difference between 90 % of the adiabatic flame temperature and the respective gas phase temperatures measured at $y = 100$ μm to account for the different wall temperatures. Predictions from Eq. (5.7) are compared to experimental values of the quenching distance as shown in Fig. 5.27 (left) with dotted lines. For each wall temperature and fuel type, the calculated values correctly capture the trend observed experimentally, but absolute values differ up to 16 %. However, considering the standard deviation of the statistical mean, these differences can be rated as minor.

Figure 5.28 shows the quenching Peclet number, $Pe_{\mathrm{Q}} = \delta_{\mathrm{Q}}/\delta_{\mathrm{F}}$, which is a non-dimensional quenching distance. A characteristic flame thickness, $\delta_{\mathrm{F}} = \lambda/(s_{\mathrm{L}} c_{\mathrm{p}} \varrho)$, is used for normalizing the flame-wall distance. The measured Peclet number of the methane flame at $T_{\mathrm{wall}} = 330$ K, $Pe_{\mathrm{Q}} = 6.8$, is slightly different (12 % difference)

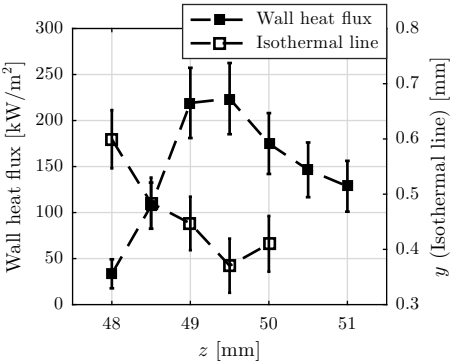

Figure 5.26. Axial profiles of the wall heat flux (close symbols) and the distances between the wall and an isothermal line representing the flame front location (here $T = 1450$ K; open symbols). The wall temperature is set to 330 K for the laminar stoichiometric methane/air flame. Error bars represent the standard deviation of measured values.

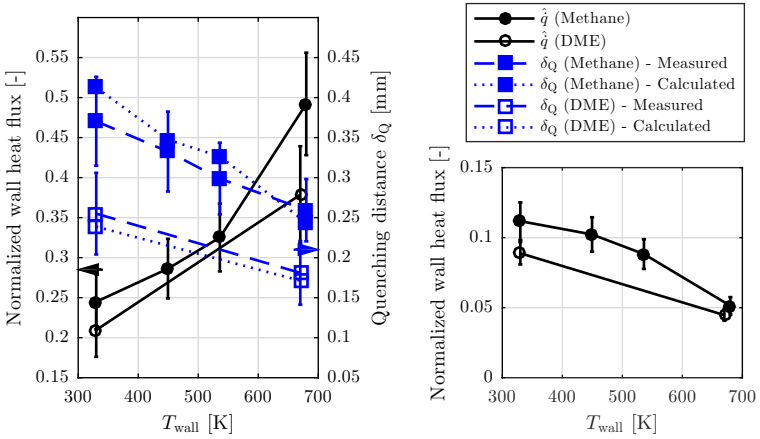

Figure 5.27. Left: Normalized peak wall heat flux along with the comparison between the measured and calculated quenching distance as a function of wall temperature and fuel type. Right: Normalized wall heat flux in the post flame region (at $z = 60$ mm for methane, $z = 50$ mm for DME). Error bars represent the standard deviation of measured values.

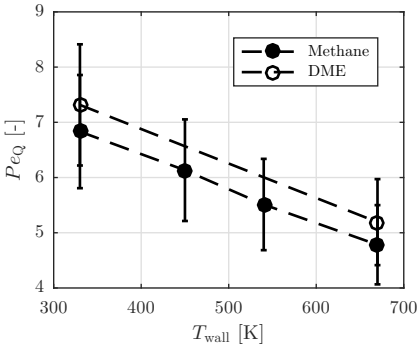

Figure 5.28. Quenching Peclet numbers, Pe_Q, evaluated from the isothermal contours that are extracted from the mean CARS data for different wall temperatures and fuel types. Error bars represent the standard deviation of measured values.

than the results from a previous study using the same configuration [99, 100]. Deviations of Peclet numbers in the literature [142] are caused by the different definitions of the flame thickness. The quenching Peclet numbers, Pe_Q, decrease with higher wall temperatures whereas the influence of the fuel type is less pronounced. This behaviour is in accordance with previous numerical findings [90].

5.3 Results and discussion for thermochemical states

5.3.1 Thermochemical states of laminar flames

The behavior of selected near-wall laminar flames is studied in more detail by analyzing the thermochemical states in terms of CO/T-scatter plots for $\phi = 1$ and $T_{wall} = 330$ K and 670 K. In Fig. 5.29, scatter plots are presented for a subset of four probe volume locations ranging from $y = 0.1$ to 0.7 mm at the quenching height. The scatter plots are separated into CO formation and CO oxidation branches, based on the location of the probe volume relative to the flame front position derived from OH-LIF. In case the CO/T probe volume is located within a region of ± 200 μm around the flame front, the sample is assigned to the CO formation branch (blue dots in Fig. 5.29). In case the probe volume is displaced at least 200 μm from the flame front in the direction of the post flame region, the CO/T plots are allocated to the CO oxidation branch (red dots in Fig. 5.29). For

selected CO mole fractions, conditional mean temperatures and respective root-mean-square (RMS) values are indicated as closed symbols and horizontal error bars, respectively. Similar to the unbounded flame, averaged RMS values range around 70 K. For comparison, the results from laminar flame calculations with (non-adiabatic) and without heat losses (adiabatic) are presented. Characteristic time scales of CO formation and oxidation are color-coded (Fig. 5.29, left column), deriving from the one-dimensional laminar flame calculations. Closer to the wall, at positions $y < 0.3$ mm, the preheat zone and primary reaction zone are probed (CO formation), whereas further away from the wall the post-flame zone is accessed, which is characterized by CO oxidation.

At the quenching height, the flame has reached its closest position to the wall. CO formation and oxidation branches are influenced by the presence of a cold wall. The experimental data for methane and DME flames shows that the CO oxidation branch is significantly shifted to lower temperatures for the entire near-wall region, which as expected, is not in accordance with the adiabatic flame simulation. In contrast, the non-adiabatic approach partially follows the experimental trend in the oxidation region. Close to the wall, at $y = 0.1$ mm, the CO formation branches for methane flames are located at lower temperatures than the one calculated with both adiabatic and the non-adiabatic boundary conditions. For DME flames, CO formation branches is shifted to much less extent. For methane at $y = 0.1$ mm with $T_{\text{wall}} = 330$ K, the temperature associated with the maximum CO concentration is reduced by approximately 640 K compared to the adiabatic flame calculation. The shift of the CO formation/oxidation branches to lower temperatures is more remarkable with $T_{\text{wall}} = 670$ K. At $y = 0.1$ mm, both CO branches for methane and DME flames are clearly located at lower temperatures than the one calculated with both adiabatic and the non-adiabatic boundary conditions. Very close to the wall, the effect of the wall on both formation and oxidation branches cannot be reproduced by the one-dimensional flame calculations. This is examined in more detail by a time scale analysis below.

Using the results from one-dimensional laminar flame calculations, spatial CO profiles are transformed into the time coordinate, τ (color code in Fig. 5.29, left column), using the local flow velocity, v, as shown in Fig. 5.30 (in case of $T_{\text{wall}} = 330$ K). Based on this representation, characteristic time scales of CO chemistry are estimated similar to [99, 100]. A characteristic time scale for CO formation, τ_{Fo}, is estimated by the time needed to attain from 10 % of the maximum CO concentration ($X_{\text{CO,max}}$) to the $X_{\text{CO,max}}$. The time scale for CO oxidation , τ_{Ox}, is deduced from the time span between the CO peak and the instant where the CO concentration dropped to the threshold value $X'_{\text{CO}} = X_{\text{CO,eq}} + 0.01(X_{\text{CO,max}} - X_{\text{CO,eq}})$. Since the non-adiabatic flame does not entirely reach the chemical equilibrium despite of

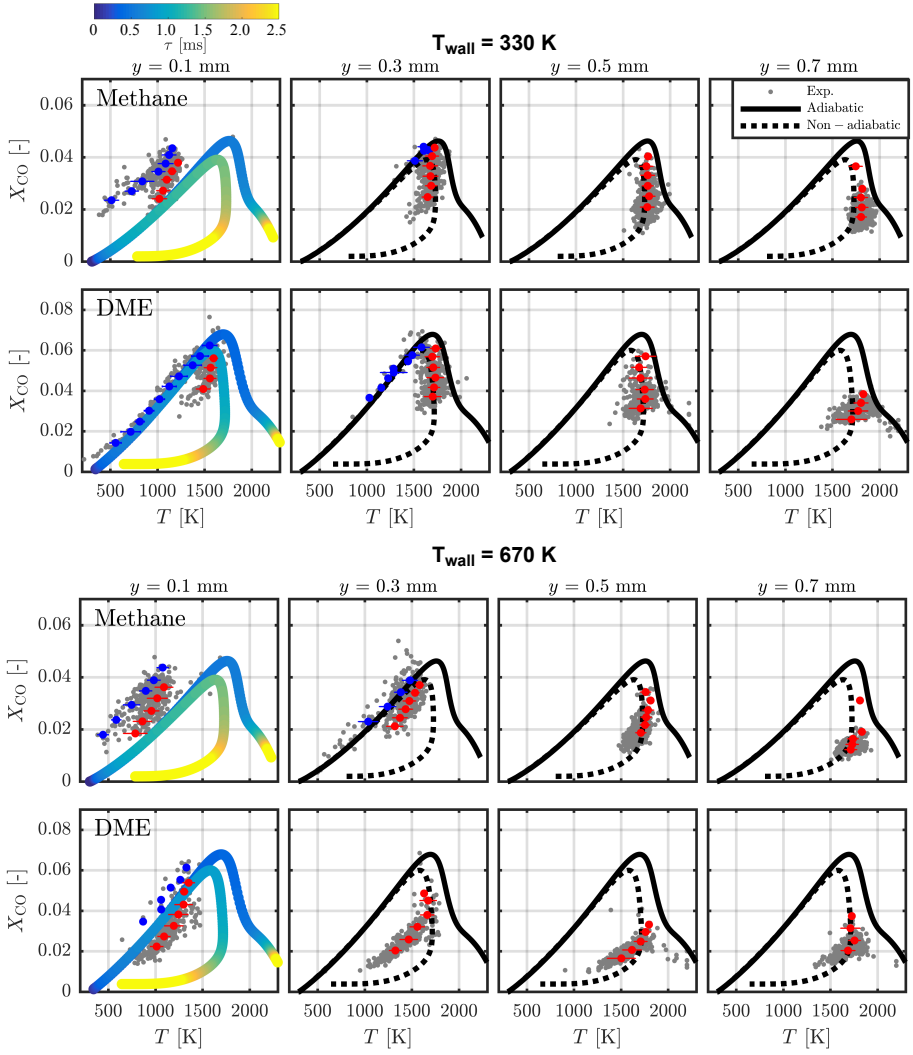

Figure 5.29. Scatter plots of gas phase temperatures and CO mole fractions for T_{wall} = 330 K (top) and 670 K (bottom) at the quenching height. Data of 400 samples for each wall distance (y = 0.1 - 0.7 mm) are shown in separated plots. All data are recorded at ϕ = 1. Conditional mean (blue: CO formation branch and red: CO oxidation branch) and RMS (horizontal error bar) of experimental data are compared to the results obtained from a one-dimensional laminar flame calculation with (dotted line) and without wall heat transfer (solid line). For y = 0.1 mm, the simulations are color-coded; the different colors represent time durations from the start of the simulation.

a prolonged computational domain, the end value of the CO mole fraction is used instead of $X_{CO,eq}$. The time scales obtained from the adiabatic case in Fig. 5.30 are $\tau_{Fo} = 0.27$ ms and $\tau_{Ox} = 4.5$ ms for the methane/air flame, and $\tau_{Fo} = 0.17$ ms and $\tau_{Ox} = 3.0$ ms for the DME/air flame. For the non-adiabatic case, formation time scales increase, whereas oxidation time scales slightly decrease. Respective time scales for the methane/air flame are $\tau_{Fo} = 0.71$ ms and $\tau_{Ox} = 4.2$ ms, and $\tau_{Fo} = 0.43$ ms and $\tau_{Ox} = 2.4$ ms for the DME/air flame. In Fig. 5.31, the corresponding ranges of time scales are marked as grey areas. For both fuels, CO formation is at least five times faster than oxidation.

To evaluate the effect of heat transfer close to the wall, the characteristic time scales for CO formation and oxidation from the simulations are compared to time scales of heat conduction deduced from experimental results. Assuming that heat conduction is dominating heat losses, the time scale of heat conduction, τ_H,

$$\tau_H = \frac{L^2}{\lambda} \varrho c_p \tag{5.8}$$

can be used as a characteristic time scale [127]. The parameter L is a characteristic length scale, representing the wall-normal distance, y. Thermal conductivity, λ, specific heat capacity, c_p, and density, ϱ, are estimated assuming unburned fuel/air mixtures for temperatures as measured for each specific wall-normal distance, y. In Fig. 5.31, time scale ranges of CO formation and oxidation are compared to time scales of heat transfer (in dependence of the wall normal distance). For the methane flames at locations $y \leq 0.2$ mm with both wall temperatures and for the DME flames at $y < 0.1$ mm ($T_{wall} = 330$ K) and $y \leq 0.2$ mm ($T_{wall} = 670$ K), both time scales of CO formation and oxidation are larger than those of heat transfer. Thus, both branches are expected to be influenced by heat losses to the wall, which is in accordance to experiments (Fig. 5.29). For methane flames at locations $y \geq 0.4$ mm and for DME flames at $y > 0.2$ mm with both wall temperatures, the time scale of CO formation is smaller than that of heat transfer. In turn, CO formation should remain unaffected in these regions. Again, this expectation compares well with experimental evidence. The CO oxidation process remains slower than the heat transfer within the entire near-wall region presented in Fig. 5.29 such that the oxidation branch is shifted towards lower temperatures in the whole range, as is from Fig. 5.29.

The reason why the present laminar flame calculations cannot reproduce the influence of the wall on the CO formation branch is due to limitations of the one-dimensional model. Varying the heat conduction parameter C introduced in Eq. (4.4), it is observed that τ_{Fo} directly correlates with the overall flame time scale $\tau_f = \delta_f / s_d$, where s_d represents the flame displacement speed (for the adiabatic

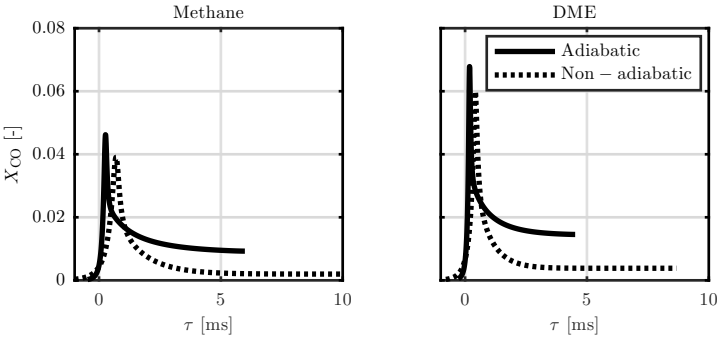

Figure 5.30. Temporal profiles of CO mole fractions separated in formation and oxidation branches for premixed stoichiometric methane/air and DME/air flames with T_{wall} = 330 K, obtained from one-dimensional flame simulations with (dotted line) and without wall heat transfer (solid line).

case $s_d = s_L$). The flame time scale (or chemical time scale) increases with heat loss until the flame finally quenches. As observed for flame calculations in Fig. 5.29, specifically for the non-adiabatic flame which is almost quenched, the formation branch remains unaffected by heat losses. A reasonable argument is that thermochemical states close to the wall correspond to flame structures which would eventually extinguish if they are not back-supported by the transport of heat and intermediate species from flame elements further away from the wall. Thus, multi-dimensional transport processes due to convection and diffusion are assumed to be responsible in this region. Hence, the interaction of laminar flames with walls cannot be modelled entirely by a one-dimensional approach. These findings are in agreement with two-dimensional simulations of a quenching flame by Ganter et al. [77]. Their DNS study indicated that multi-directional species diffusion has a significant influence on CO formation near the wall.

This limitation of the one-dimensional flame simulation implies a need for future model development of tabulated chemistry approaches regularly used in simulating turbulent premixed flames. These approaches typically rely on tabulated one-dimensional flame simulations. To extend tabulated chemistry concepts to side-wall quenching, multi-directional transport processes must be included.

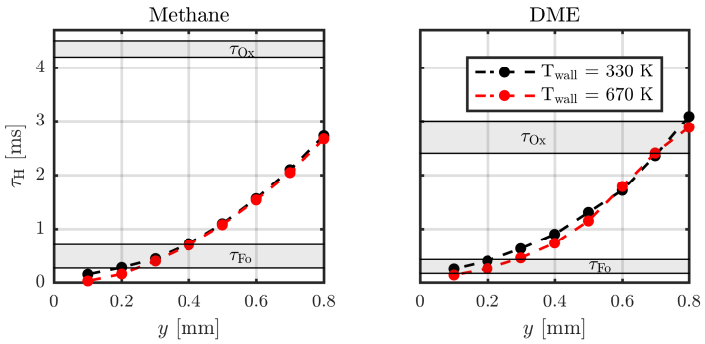

Figure 5.31. Estimated heat transfer, τ_H, depending on the wall distance, y. The gray areas represent ranges of time scales of CO formation, τ_{Fo}, and CO oxidation, τ_{Ox}, estimated from adiabatic and non-adiabatic one-dimensional flame calculations. In case heat transfer is faster than the corresponding chemical time scale, the respective CO branch is influenced.

5.3.2 Thermochemical states of turbulent flames

Thermochemical states observed in turbulent flames usually show a more complex behavior than those of laminar flames. For performing a thermochemical analysis of turbulent flow conditions, a turbulence grid is installed into the interior nozzle of the SWQ burner. The Reynolds number is maintained at 5000 in order to investigate only the influence of turbulence. Figure 5.32 shows CO/T scatter plots at a height of $z = 42.5$ mm (mean quenching height) for a stoichiometric methane/air flame with a wall temperature of $T_{wall} = 330$ K. Similar to Fig. 5.29, scatter plots are distinguished in CO formation and CO oxidation branches, based on instantaneous flame positions derived from OH-LIF. Conditional mean and root-mean-square (RMS) temperatures for selected CO mole fractions are indicated as filled symbols and horizontal error bars, respectively. Compared to laminar flames, the average of RMS temperatures remains at similar values of 70 K for the CO formation branch, whereas the RMS value increases to 130 K for the CO oxidation branch at $y \geq 0.3$ mm. This indicates that turbulence primarily affects temperature fluctuations within the CO oxidation region.

For each location of the wall normal distance, y, both the CO formation and the oxidation branch are shifted to lower temperatures. This shift is more pronounced at $y = 0.1$ mm and for larger wall distances the CO oxidation branch is significantly more affected. Additionally, due to increased scattering within the

oxidation branch, intermediate states between both branches are observed. It is an indication that both branches are influenced by a wall heat transfer increase due to turbulence.

Following the procedure discussed for laminar flames, chemical time scales are compared to time scales of heat transfer. Because the time scale of heat conduction τ_H shown in Eq. (5.8) does not account for turbulent conditions, integral turbulent time scales are used instead. Integral time scales are deduced from temporal autocorrelation function, R_{ii}, of the fluctuating axial velocity component, u_z', close to the wall (Fig. 5.33) according to Section 2.1.1, Eq. (2.11). For velocity components, a separate experiment of high-speed PIV (operated at 10 kHz) is carried out with the configuration presented in Section 4.2.1[2]. The center of the PIV interrogation volume closest to the wall is located at $y \approx 0.15$ mm. The integral time scale corresponds to the integral of the determined autocorrelation up to the first zero crossing of R_{ii}. Using PIV data at the mean quenching height, the integration yields a value of 0.4 ms close to the wall ($y < 1.0$ mm) and in the order of 1.0 ms far from the wall. The value close to the wall is on the same order of magnitude as CO formation (0.27 - 0.71 ms, compare Fig. 5.31 left) but one order of magnitude smaller than CO oxidation (4.2 - 4.5 ms). However, considering the limited spatial resolution of the PIV measurements acting as a low pass filter, the apparent integral time scale is most certainly overestimated such that the impact upon the CO formation branch, specifically at small wall distances ($y \leq 0.3$ mm), appears plausible. Independent of this likely bias towards large values of the integral time scale, comparison to the time scale of CO oxidation is in accordance with the experimental observations, showing a shift to lower temperatures for the entire region investigated.

[2] This measurement was performed by Christopher Jainski and Martin Rißmann during the work on the thesis [97]. We contributed equally to this section.

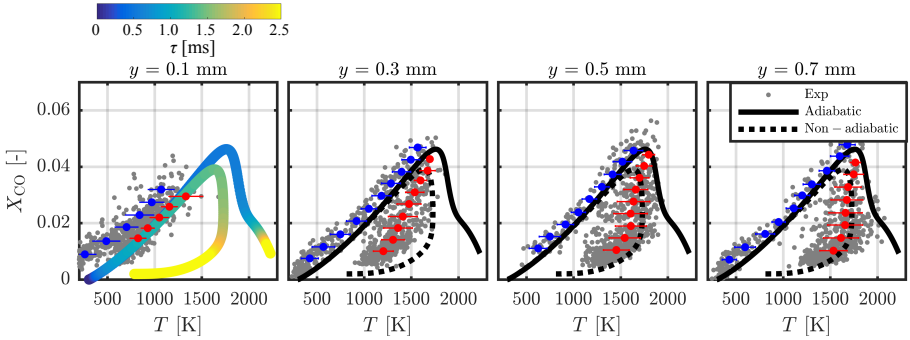

Figure 5.32. Scatter plots of gas phase temperature and CO mole fractions at a height of $z = 42.5$ mm for a methane/air turbulent flame. Conditional mean (blue and red dots) and rms (horizontal error bar) of experimental data are compared to the results obtained from a one-dimensional laminar flame calculation with (dotted line) and without wall heat transfer (solid line). For $y = 0.1$ mm, the simulations are color-coded; the different colors represent time duration from start of the simulation.

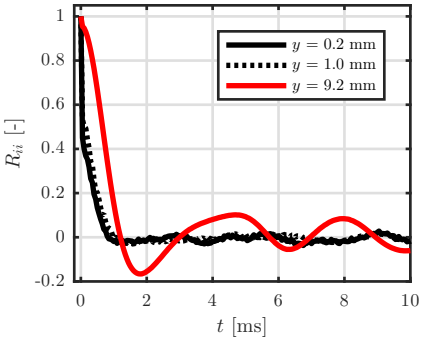

Figure 5.33. Temporal autocorrelation R_{ii} of the velocity fluctuation component u_z' at a height of $z = 42.5$ mm to determine the integral time scale.

6 Investigation of flame structures and local heat release rate

The results obtained in the previous chapter show the influence of the wall heat flux on the CO/T thermochemical states during the side-wall quenching (SWQ). In addition to the CO/T states, the heat release rate (HRR) is also strongly coupled to the wall heat flux. The focus of the experiment presented in this chapter is the imaging of local HRR on atmospheric flames in a SWQ geometry. The influence of different wall temperatures (330 and 670 K) as well as equivalence ratios (0.83 and 1.0) are compared for premixed methane/air and dimethyl ether (DME)/air flames. As discussed in Section 3.3.3.3, local HRR can be derived from the product of CH_2O- and OH-PLIF signals.

The chapter begins with a description of the optical setup used here and the characterization of the measurement systems. Subsequently, the resulting HRR images near the wall are presented for a laminar flame configuration. In addition, certain aspects of the HRR for a turbulent configuration are discussed in more detail in terms of the correlation between the flame curvature and the HRR.

The results presented in this chapter are based on those already published in [112].

6.1 Simultaneous CH_2O-PLIF and OH-PLIF

6.1.1 Optical setup

The laser-optical setup used in this experiment is shown in Fig. 6.1 and is derived from [61]. The lasers for CH_2O- and OH-PLIF are introduced to the region of interest (ROI) from the top (see Fig. 6.1 b) and the PLIF image planes are aligned perpendicular to the wall. Both LIF signals are acquired simultaneously. Different from the previous section, both PLIF methods are semi-quantitative and planar measurements. They require a laser profile correction. Since the principle of OH-PLIF used in this section is similar to that in the previous chapter, the following section introduces both setups for CH_2O-/OH-PLIF together.

The CH_2O molecule is excited in the $2_0^1 4_0^1$ band of its $\tilde{A}^1A_2 - \tilde{X}^1A_1$ transition using 339 nm (CH_2O-beam) and the OH radical is excited in the $Q_1(6)$ line of

the $A^2\Sigma^+(v'=1) \leftarrow X^2\Pi(v''=0)$ transition at 282.9 nm (OH-beam). Laser excitation wavelengths are generated using two frequency-doubled narrowband dye laser systems (Sirah Lasertechnik GmbH, Double Dye). For the CH_2O-beam, Pyridine 1 (Exciton) is dissolved in ethanol, while Rhodamine 6G (Exciton), also dissolved in ethanol, is used to generate the fundamental light for exciting OH. Each dye laser system is optically pumped using a frequency-doubled, Q-switched, pulsed Nd:YAG laser at 532 nm with a repetition rate of 10 Hz (Spectra-Physics, Quanta-Ray PIV series, PIV 400). The time separation between the CH_2O- and OH-beam is 600 ns. Averaged UV-pulse energies in the probe volume are 2.13 mJ (CH_2O) and 1.15 mJ (OH), respectively. Both laser beams are shaped to light sheets by a combination of cylindrical lenses (anti-reflection coated for UV). Each path features an individual telescope for expanding the beam and a sheet forming lens for focusing the expanded beam to the final laser sheet (see Fig. 6.1a for the arrangement of lenses and focal length). The laser-sheet thickness within the ROI is approximately 200 μm for the CH_2O-beam and 160 μm for the OH-beam.

A dichroic beam splitter (Semrock Inc., Di01-R325-25×36) is used to overlap the CH_2O- and OH-beam. The overlap of both light sheets within the ROI is confirmed using a beam monitor (DataRay Inc., WinCamD, equipped with a UV-converter). For this procedure, the wall is removed and replaced by the beam monitor. The overlap is checked at different positions in the axial direction (z-direction) to ensure that both sheets are parallel to each other. A flat fused silica glass plate (Suprasil 1, thickness 3 mm) is used to reflect a small energy fraction of the overlapped laser sheets to a reference dye cuvette (Coumarin 307 in ethanol) for simultaneous beam profiling. The PLIF-signals of the reference dye are recorded using a CCD camera (PCO AG, sensicam qe double shutter, 1376 × 1040 pixels, 6.45 μm pixel size) equipped with a 60 mm lens (Nikkor, $f\#$ 2.8). The camera is operated in double shutter mode to monitor both CH_2O- and OH-sheet profiles in consecutive frames. The distance between the glass plate and the reference cuvette matches the distance between the glass plate and the ROI. For mapping the reference cuvette image to that of the ROI, a slit, clearly defining the image boundaries, is used at the position between the beam splitter and the glass plate. The fluorescence profiles deduced by the reference cuvette images are used in the post-processing to perform a shot-to-shot laser sheet correction for the CH_2O- and OH-PLIF signals.

PLIF-signals of CH_2O and OH in the ROI are recorded perpendicularly to the incident laser sheets. The ROI covers a region of 4 (y) × 15 (z) mm^2. The CH_2O-detection system consists of an achromatic lens, an interference filter (Semrock Inc., FF01-492/SP, 390-480 nm, > 95 % transmission), an 85 mm objective lens (Carl Zeiss AG, Planar T* ZF, $f\#$ 1.4), an intensified relay optics (LaVision GmbH,

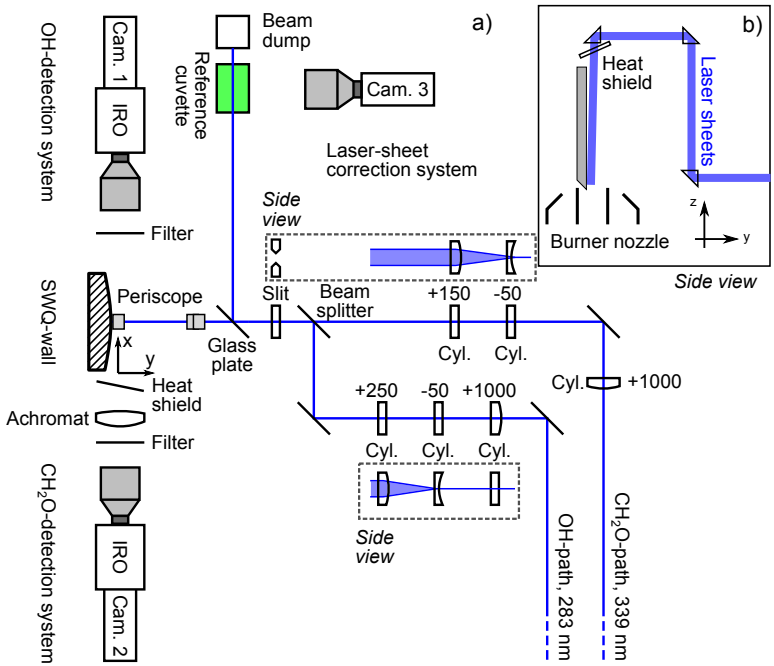

Figure 6.1. Optical setup for simultaneous CH_2O- and OH-PLIF. a) top view, b) side view of beam periscope.

low-speed IRO, gate 100 ns) and a CMOS camera (LaVision GmbH, Imager M-lite). The achromatic lens is located close to the burner exit and protected by a heat shield (Edmund Optics, Schott KG glass). The heat shield is tilted to avoid any reflections between the OH- and CH_2O-detection systems. The OH-detection system consists of an interference filter (Laser Components, UV-B, 308±10 nm, >80 % transmission), a 150 mm UV-transparent objective lens (B. Halle Nachfl. GmbH, $f\#$ 2.5), a low-speed IRO (gate 50 ns) and a sCMOS camera (LaVision GmbH, Imager sCMOS) for image acquisition.

For each operating condition, in combination with the reference cuvette images, a set of 1000 (in the laminar case) or 4000 (in the turbulent case) CH_2O- and OH-PLIF images are recorded.

6.1.2 Data evaluation

Background subtraction

For deducing relative heat release rates, CH_2O- and OH-PLIF images need a series of corrections. Before measurements in each operating condition, a series of 100 individual images of the background signal is recorded. These background images are taken both with laser operation in the absence of the flame and without laser operation in the existence of the flame. The mean background image is then subtracted from each individual signal image, thus the influences by the flame chemiluminescence and the fluorescence of the wall contamination due to the laser sheet can be removed.

Laser sheet correction

The intensity of the excitation laser is inhomogeneous in space and time. The intensity fluctuations lead to fluctuations in the detected LIF intensity. To compensate these fluctuations, the individual fluorescence images of the reference cuvette are used. For each reference image, background images recorded without laser operation are subtracted. After the subtraction, each intensity in the pixels of reference images are spatially averaged in the beam-wise direction. The resulting one-dimensional profile is normalized by the maximum intensity in the series of reference images in each operating condition. This processing enables to normalize the temporal laser-intensity fluctuation within each operating condition. To minimize the noise, the normalized profile is smoothed with a linear regression filter. The profile is inverted and grown into the size of the original image in ROI in the beam-wise direction. Figure 6.2 shows a typical image of the correction factor.

To map the correction image to the PLIF image, the edge positions of the slit in both reference and PLIF images are used. For this purpose, the image recording is carried out with slightly closed slit (closed until the edges of the slit appear in the reference and PLIF camera images) separately from the measurement. The mapped shot-to-shot spatial correction images are multiplied by each individual CH_2O- and OH-PLIF image. Figure 6.3 shows a comparison between an exemplary raw OH-PLIF image and the corrected image.

Image mapping

In a final step, calibration target recordings (LaVision GmbH, Type 11-fine) are used to map CH_2O- and OH-PLIF images to each other and to transform them

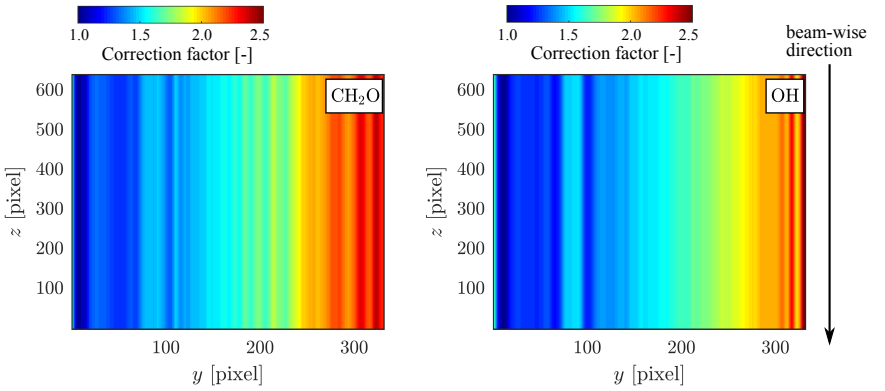

Figure 6.2. Correction images to compensate for the spatial laser inhomogeneities of CH_2O- and OH-PLIF images. Notice that the visualized scales in horizontal axis are larger than that in vertical axis to clearly indicate the inhomogeneous laser-sheet profile.

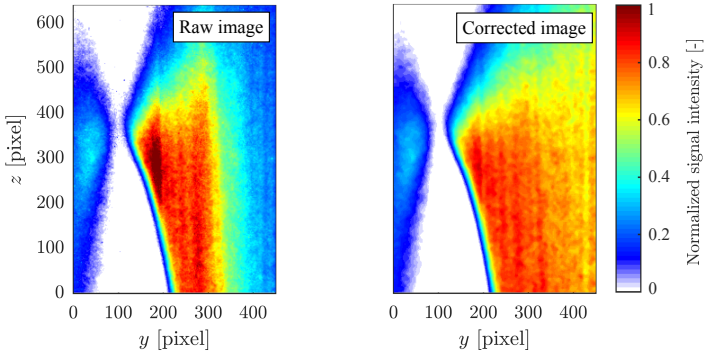

Figure 6.3. Selected OH-PLIF images. Left: Raw image after background subtraction in the pixel-based camera coordinate system. Right: Corrected image by the laser intensity. The intensity is normalized by the maximum intensity in the series of PLIF images in each operating condition.

from pixels to a physical space coordinate system. For the transformation, a third order polynomial function is used (DaVis 8.3, LaVision GmbH). To prepare both PLIF images for the final multiplication, image intensities are interpolated to equal grids (10 μm-spacing). Relative HRRs are finally deduced by the multiplication $S_{CH_2O} \times S_{OH}$. Furthermore, HRRs are normalized by values obtained for planar adiabatic flames burning far from the wall as described later in Section 6.2.

6.1.3 Spatial and temporal resolution

The spatial resolution of the CH_2O- and OH-LIF system is evaluated by the procedure described in Section 5.1.4 using the USAF 1951 resolution target and a contrast transfer function. The resulting spatial resolutions are 57 μm for the CH_2O-LIF system and 37 μm for the OH-LIF system. The temporal resolution is given by the laser pulse duration. This is detected by means of a photodiode and is measured to be approximately 10 ns in this experiment. The system repetition rate is 10 Hz.

6.1.4 Precision and accuracy

The precision and accuracy of the CH_2O- and OH-PLIF system in terms of two-dimensional species distribution measurement are difficult to quantify. Therefore, the results of CH_2O- and OH-PLIF measurements are used and discussed only semi-quantitatively in this work, which are corrected for the laser-sheet inhomogeneities but not for the influences of temperature and quenching.

6.2 Results and discussion for the laminar flame configuration

For the detailed analysis of selected near-wall flames, the local heat release rate is determined using simultaneous CH_2O- and OH-PLIF. Measurement areas are fixed in space, independent of the instantaneous flame position, which slightly fluctuate in this study due to remaining Helmholtz resonances. Thus, using a flame-fixed coordinate system for ensemble-averaged images deconvolutes the results from such intermittent flame position fluctuations. The individual images are vertically shifted by their instantaneous distances to the averaged quenching point, i.e., after this offset all images feature the same quenching height. The quenching point in the axial direction is deduced from a flame front detection explained below. Figure 6.4 shows resulting ensemble-averaged, normalized CH_2O- and OH-PLIF intensities for laminar stoichiometric methane/air (top) and DME/air (bottom) flames during

SWQ (T_{wall} = 330 K). Both CH_2O- and OH-PLIF ensemble-averaged intensities are normalized to the maximum value in each averaged image, respectively.

The normalized CH_2O-PLIF image (Fig. 6.4, left) represents the preheating region of the flame. In the FWI-zone, relative CH_2O-signal magnitudes are similar compared to regions further away from the wall. Only for distances where $y <$ 0.08 mm a steep gradient is observed especially in the DME flame. Starting at $y \approx$ 0.3 mm from the wall, the CH_2O-distribution broadens in regions away from the wall, which indicates a change in the flame structure. Gradients of the OH-PLIF signal shown in Fig. 6.4 (middle) trace the flame front and the OH-PLIF signal behind the flame front marks high-temperature post flame regions. Slightly downstream of the CH_2O-signal, the gradient of the OH-PLIF signal in the FWI-zone decreases. This again confirms a change in the flame structure close to the wall. Compared to CH_2O-PLIF signals, that of OH-PLIF decrease more rapidly when approaching the wall. This is attributed to heat losses that impact the high-temperature zone to a greater extent than the low-temperature zone as indicated by CH_2O.

For the local heat release rate (HRR) imaging, the corresponding pixel-by-pixel product of the CH_2O- and OH-LIF signal is calculated as a semi-quantitative indicator (Fig. 6.4, right). The HRR values are normalized to an adiabatic unstretched flame region (rectangle in Fig. 6.4, right). The relative HRR distribution shows decreasing values for wall-normal distances where $y <$ 0.25 mm for the methane/air flame and $y <$ 0.38 mm for the DME/air flame. In accordance to the broadened CH_2O and OH distributions far from the wall, the HRR-zone similarly broadens.

An important quantity for describing FWI processes is the quenching distance, δ_Q. Various approaches for determining the quenching distance are reported in literature and are already discusses in Section 5.2.4. In this chapter, two methods are used and compared to each other. For the first approach, δ_Q is determined from the results of the planar OH-LIF measurement as applied in the previous section. There, δ_Q is represented by the wall-normal distance between the flame front and wall. The flame front is extracted from the steepest OH-gradient in the flame-normal direction. For the second approach, the flame front is extracted from HRR profiles. In the first step, the axial quenching height is defined by the first approach using the OH-gradient. In the second step, the flame front is assumed to coincide with the highest HRR value at the axial position of quenching. Figure 6.5 (left) shows the ensemble-averaged, wall-normal profiles of OH, CH_2O and HRR at the axial position of quenching for the methane/air flame with the wall temperature of 330 K at a laminar flow configuration. The quenching distances derived from the first and the second approach are shown as the cross marks in Fig. 6.5 (left). Figure 6.5 (right) compares the results of the two definitions of δ_Q derived for different operating conditions of wall temperature, equivalence ratio and fuel type. For each

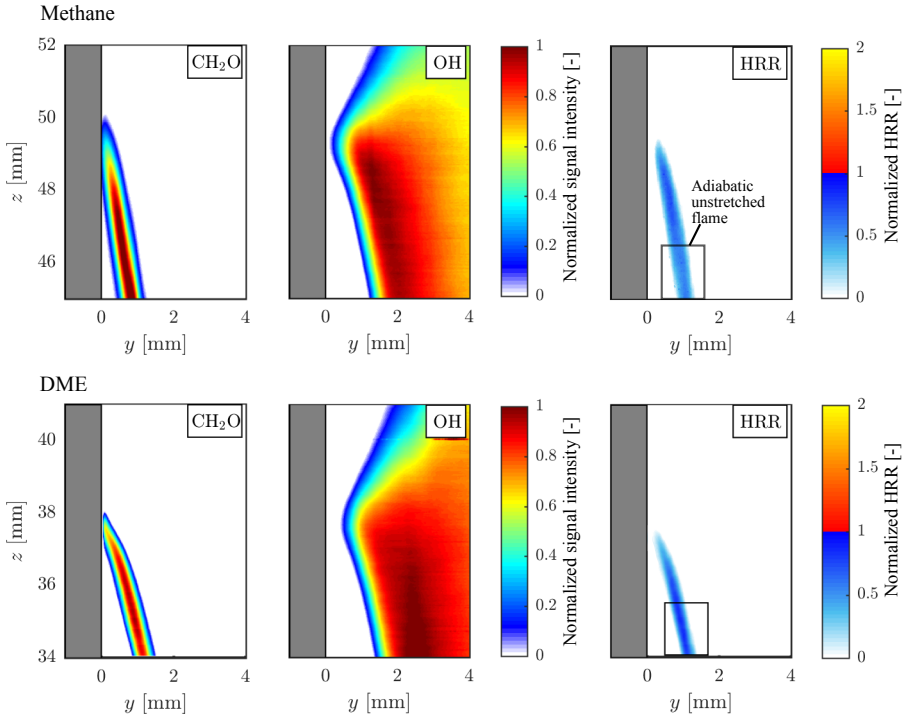

Figure 6.4. Ensemble-averaged normalized CH_2O-, OH-PLIF images and corresponding relative HRR images during SWQ for a laminar methane (top) and DME (bottom) flame ($\phi = 1$). The wall temperature is set to 330 K. The gray rectangle ($y < 0$ mm) marks the position of the wall. For HRR images, bi-modal color map is used to outline differences from adiabatic unstretched flame. Statistics are based on 1000 samples.

equivalence ratio, the δ_Q determined by the HRR is 40 - 50 μm smaller than the values obtained from the OH-PLIF images.

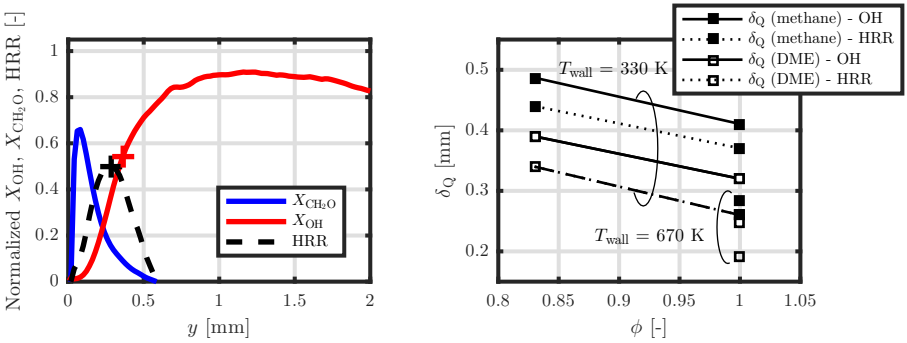

Figure 6.5. Left: Ensemble-averaged, wall-normal profiles of CH_2O, OH and the product of CH_2O×OH (HRR) at the quenching height (z = 49.5 mm) for a laminar, stoichiometric methane/air flame with the wall temperature of 330 K. Right: Comparison of quenching distances derived from OH-PLIF images and HRR images in dependence of equivalence ratio, wall temperatures and fuels. Statistics are based on 1000 samples.

6.3 Results and discussion for the turbulent flame configuration

Figure 6.6 shows a selected instantaneous CH_2O- and OH-PLIF signal, and the corresponding relative HRR image from turbulent stoichiometric methane/air and DME/air flames (T_{wall} = 330 K). Similar to the laminar case, the HRR image is normalized to the maximum intensity in the unstretched flame region (rectangle in Fig. 6.6, right). In accordance to laminar flow conditions, HRRs decrease when the flame approaches the wall. However, in the turbulent case, relative HRRs significantly fluctuate in space and time. Instantaneous normalized HRRs vary along the flame front as it is affected by local turbulent eddies imposing flame stretch and causing curvature. These fluctuations are identified with a statistical analysis in the following.

The flame front in the turbulent flame configuration is extracted from the normalized maximum HRR positions along the flame front defined by the OH-gradient. A steep decrease in the maximum HRR is observed approaching the wall and the quenching point. Using this data, quenching is defined at the position where the maximum HRR falls below 0.5. In contrast to the laminar configuration, the flame is highly wrinkled and the quenching height and distance vary in time and space. A mean flame progress variable c is calculated from the average of instantaneous binarized HRR images separating unburned (c = 0) from burned regions (c = 1). Figure 6.7 (left) shows the resulting c distribution of the stoichiometric DME/air

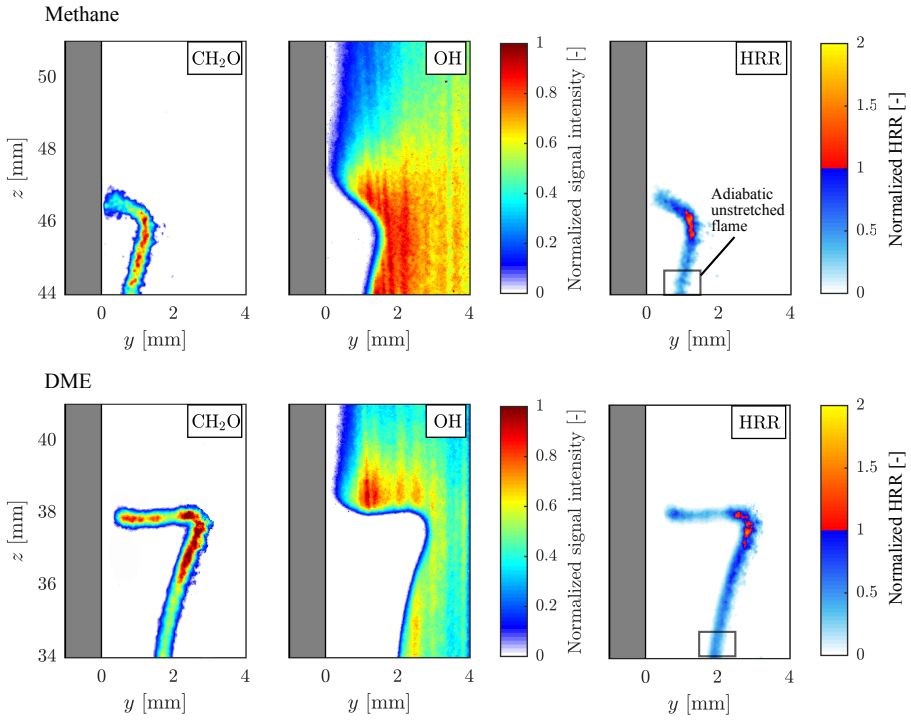

Figure 6.6. Instantaneous normalized CH_2O-, OH-PLIF images and corresponding relative HRR images during SWQ for turbulent methane (top) and DME (bottom) flames ($\phi = 1$, $T_{wall} = 330$ K). For HRR images bi-modal color map is used to outline differences from adiabatic unstretched flame. The gray rectangle ($y < 0$ mm) marks the position of the wall.

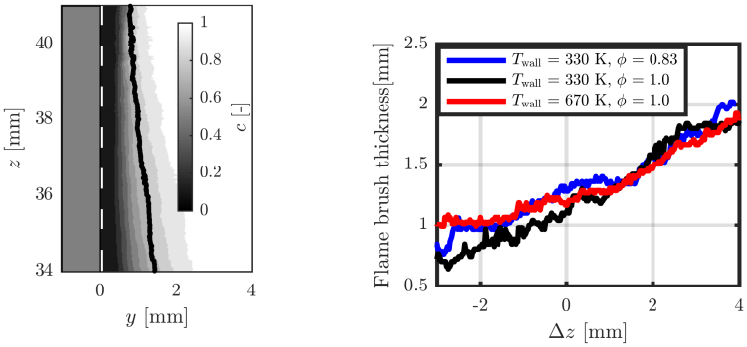

Figure 6.7. Left: Flame brush visualized by the mean flame progress variable, c, and mean flame front position (thick black line) for turbulent, stoichiometric DME-air flames. Right: Averaged flame brush thickness with flame-fixed coordinate system. Statistics are based on 4000 samples.

flame with $T_{wall} = 330$ K as the representative case. The distribution of c represents the flame brush and its evolution along the wall. For mean flame positions far-off the wall, the flame brush is wide. Further downstream where the flame interacts with the wall, the flame brush narrows. In this region, turbulent eddies push the flame against the wall, which reduces flame wrinkling [150].

The thickness of the flame brush is defined here as the flame front-normal difference of positions at $c = 0.1$ and $c = 0.9$ in the following. For each operation condition of DME flames, the flame brush thickness along the wall is shown in Fig. 6.7 (right) with a flame-fixed coordinate system. Positive values of Δz represent a position upstream of the quenching point, while negative values of Δz are located downstream of the quenching point of the flame. There is little variation in flame brush thickness with varying equivalence ratios, and similar behavior is found for methane flames.

The behavior of the local HRR is studied in more detail by analyzing the correlation with the flame curvature. As it is apparent from Fig. 6.6 (right), relative HRRs vary along the instantaneous flame front due to local turbulent eddies imposing flame stretch and causing curvature. The variation of HRR with the flame curvature is investigated using the results obtained from HRR images. The local curvature in the plane of observation is calculated from the flame-fixed coordinates using the following equation [89]:

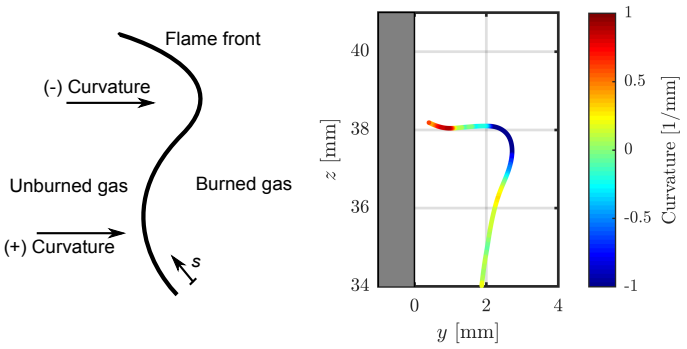

Figure 6.8. Left: Schematic showing the definition of curvature along the flame front derived from HRR imaging. Right: Instantaneous flame curvature derived from the HRR image during SWQ for a turbulent DME-air flame ($\phi = 1$) shown in Fig. 6.6.

$$H = \left[\left(\frac{d^2y}{ds^2} \right)^2 + \left(\frac{d^2z}{ds^2} \right)^2 \right]^{\frac{1}{2}}. \tag{6.1}$$

The choice of differential width size (ds) is crucial for the calculation of curvature. In order to obtain curvatures from both small-scale and large-scale wrinkles along the flame, the value of ds is determined as the averaged flame brush thickness described above for each operating condition.

A schematic representation of this curvature is shown in Fig. 6.8 (left). Positive curvature is defined as convex in the unburned gas region, whereas negative curvature is defined as concave in the unburned gas. Figure 6.8 (right) shows the instantaneous flame curvature derived from the HRR-image shown in Fig. 6.6 (bottom, right).

The wall-normal profiles of curvature, averaged in the z-direction, are shown in Fig. 6.9 (left) for turbulent methane and DME flames with different equivalence ratios and wall temperatures. The averaged curvature strongly decreases when the flame approaches the wall ($y < 0.5$ mm) for both fuel types due to increasing viscosity. Comparing averaged curvatures for different wall temperatures, the near-wall curvature decreases with higher wall temperature as expected for increased viscosity of higher near-wall gas temperatures. The influence of the equivalence ratio is less significant.

The correlation of the flame curvature and HRR is shown as the profile of the conditionally averaged HRR, which is done across the flame front in space, against the flame curvature in Fig. 6.9 (right) for turbulent flames with different equivalence ratios and wall temperatures. Overall, an increase in HRR with negative curvature is observed, which is clearly found with the lean DME flame. This behavior is discussed in more detail by introducing the Lewis number effect [115]. Thus, when the effective Lewis number (Le_{eff}) defined by Eq. (6.2) is larger than 1, thermal diffusion to the unburned gas is more dominant compared to deficient species diffusion [1] as schematically shown in Fig. 6.10.

$$Le_{eff} = \frac{\text{Thermal diffusion}}{\text{Deficient species diffusion}}. \tag{6.2}$$

With the negative flame curvature, the unburned gas is further heated and it promotes the flame. This results in an increase in heat release rate, which is found with the lean DME flame due to its Le_{eff} being larger than 1 [190].

[1] The deficient species correspond to the fuel and oxidizer species for lean and rich mixtures, respectively.

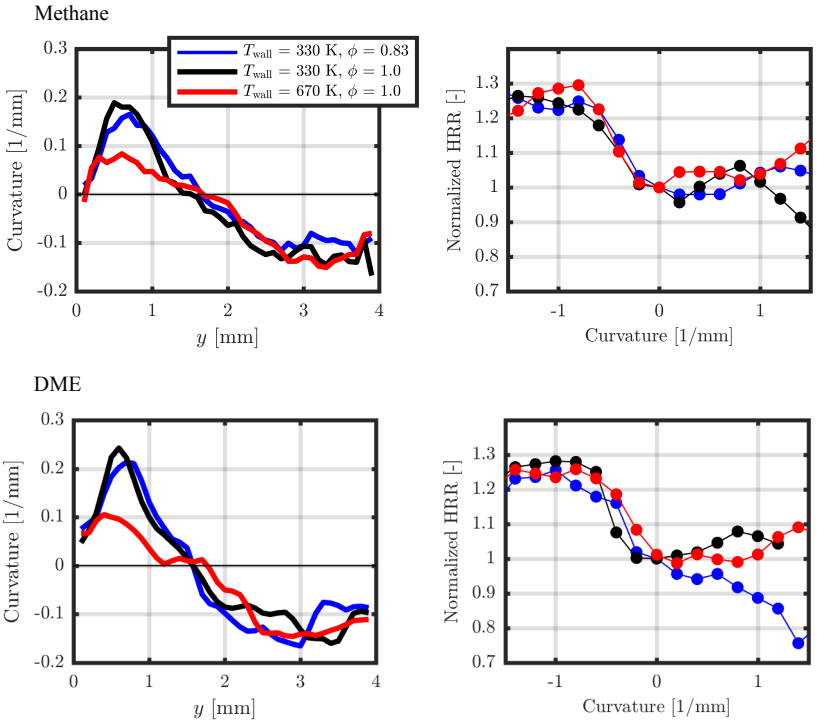

Figure 6.9. Left: Wall-normal profiles of curvature averaged in the z-direction against the wall-normal distance, y. Right: Conditionally averaged profiles of HRR against curvature. Statistics are based on 4000 samples for a turbulent, stoichiometric methane/air flame (top) and a DME/air (bottom) flame.

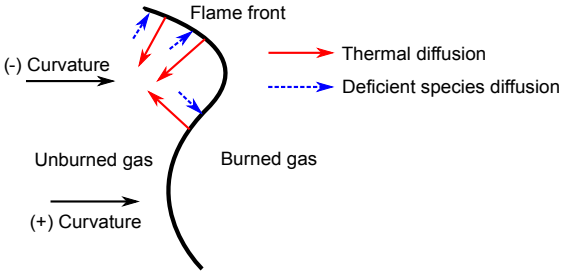

Figure 6.10. Schematic view of the thermal and species diffusion with Lewis number effect ($Le_{eff} > 1$).

7 Feasibility study on near-wall Raman measurements

The results obtained by simultaneous CARS and CO-LIF measurements shown in Section 5.3 provide thermochemical states of premixed flames at non-adiabatic conditions. For the better understanding of near-wall reactions, the measurement of additional product species simultaneously with the temperature and CO concentration is desired.

Raman spectroscopy is a promising technique to quantify combustion-related product species simultaneously. For this purpose, laser-based point-wise or line-imaged instantaneous Raman/Rayleigh scattering has been developed continuously over the last decades [8, 11]. The demands on laser, optical and detection systems make gas phase Raman spectroscopy challenging due to the weakness of the spontaneous Raman scattering process. Furthermore, the processing of the data into quantitative concentrations is complex due to the temperature dependence of Raman cross sections. Especially near the wall, scattering and reflection noises from the wall on the weak Raman signal are even higher than with other measurement techniques (e.g. CARS, LIF).

7.1 State of the art

As the state of the art reported in literature [39], spontaneous Raman scattering was utilized previously in a stationary laminar SWQ configuration. For excitation, a continuous wave argon-ion laser was used, providing a spatial resolution of 80 μm at the probe volume location. Temperatures were deduced from nitrogen number densities in combination with the ideal gas law. Hydrocarbon densities were obtained by integration of the Raman spectra in the C-H stretch region. Due to varying Raman cross-sections of intermediate hydrocarbons, only C-H bonds were extracted, not individual mole fractions of fuel or specific intermediate hydrocarbons. In a study by Appel et al. [4], one-dimensional Raman imaging was applied with OH-LIF in a near-wall measurement. Wall-normal profiles of major species concentrations were used to evaluate the validity of detailed combustion models, including the homogeneous and heterogeneous phase chemistry. Raman measurements as close as 0.6 mm to the wall were reported.

In this chapter, a feasibility study on near-wall Raman spectroscopy applied to the used SWQ geometry is carried out. Since the $H_2O_{(g)}$ molecule is a product in hydrocarbon flames and an appropriate species to describe a progress variable, it is selected as a target molecule in this work. Another advantage of focusing on the $H_2O_{(g)}$ molecule is that the spontaneous Raman scattering spectrum of $H_2O_{(g)}$ is far from that of other main combustion species. The closest distance to the wall is desired to be comparable to CO-LIF, and is on the order of 0.1 mm. The purpose of this study is to determine the closest distance of the probe volume to the wall, and to characterize the signal quality near the wall. In this study, a two-dimensional camera is used instead of the spectrometer. The $H_2O_{(g)}$ signal originating from spontaneous Raman scattering is separated from all remaining emission by using a narrow band-pass filter. For this reason, the method used here will be called "Raman imaging" in the following section.

7.2 Principles

Raman and Rayleigh scattering processes are closely related from the physical point of view. While the Raman scattering process is an inelastic process, the Rayleigh scattering process is its elastic counterpart. Since all molecules in the detection volume participate in the scattering process, it is possible to measure the concentrations of several combustion-related species ($CO_2, O_2, CO, N_2, H_2O, CH_4$ and H_2) simultaneously [7]. The advantage of Raman and Rayleigh spectroscopy is that only one laser is required and this laser does not have to be tuned to a specific wavelength, since the exciting wavelength is irrelevant to the scattering process.

In Raman scattering, the radiation emitted by a specific molecule changes in frequency. If the frequency is lower compared to the excitation beam, it is called Stokes-Raman, and if the frequency is higher, it is anti-Stokes-Raman as discussed in Section 3.3.2. For example, some Raman shifts ($\Delta\nu$) are shown in Table 7.1 [57]. The described processes are illustrated by the diagram shown in Fig. 7.1. The Rayleigh, the Stokes-Raman and the anti-Stokes-Raman processes are shown there.

The scattered Stokes-Raman signal is linearly proportional to the number density of the respective excited species as follows [110]

$$N_i \propto S_{Raman,i}. \tag{7.1}$$

Since differential Raman cross-sections are temperature dependent, temperatures are commonly measured simultaneously with the Raman scattering.

Table 7.1. Raman shifts of different species at laser excitation with 532 nm [57].

Species	$\Delta\nu$ [cm^{-1}]	Wavelength [nm]
N_2	2330	607.3
O_2	1556	590.0
H_2	4161	683.2
H_2O	3652	660.5
CO	2175	600.5
CO_2	1388	574.4
	1285	571.0
CH_4	2915	629.6
	3017	633.7

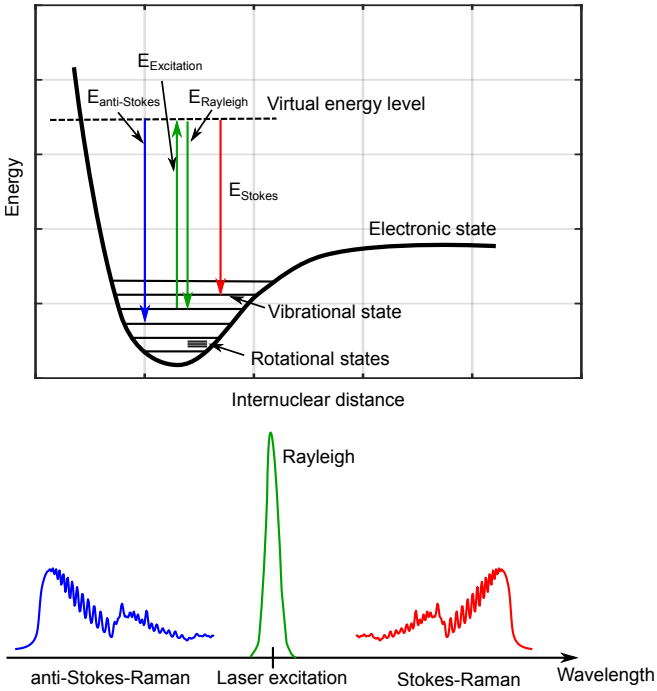

Figure 7.1. Elastic and inelastic Rayleigh and Raman scattering process and the resulting spectra [57]. The shift of the wavelength is shown in the lower part of the figure.

7.3 Experimental setup

Raman imaging is conducted with the configuration shown in Fig. 7.2. The Raman scattering is excited by a cluster of four sequentially fired, frequency doubled Nd:YAG lasers (InnoLas) operating at 532 nm [155]. The system repetition rate is 5 Hz. Dichroic optics are used to combine the four subsequent pulses and the beam waists are adjusted by optical telescopes. Three optical delay lines stretched all pulses to ≈ 500 ns (FWHM) to decrease the probability of an optical breakdown. The alignment of all beams is mostly covered by using three motor driven mirror mounts. The combined laser energy at the probe volume is up to 1.6 J/pulse and is focused by a 750 mm lens.

The $H_2O_{(g)}$ Raman signal detection system consists of a 150 mm achromatic lens, three interference filters (two high-pass, one band-pass), an 85 mm objective lens (Canon, $f\#1.2$) and a low-noise, thermo-electrically cooled electron-multiplying CCD (EMCCD) camera (Andor iXon) as shown in Fig. 7.2. The Rayleigh scattering and wall reflections from the laser are suppressed with these filters. With a band-pass filter, the Raman emission of the $H_2O_{(g)}$ molecule (≈ 650-665 nm) is selected. In this wavelength range, there are no spectral cross influences and superimpositions with other main combustion species. The transmittance of filters are summarized in Fig. 7.3. For a better signal-to-noise ratio, a spatial pixel binning on the camera chip (8 pixels in the beam direction, 2 pixels in the beam-normal direction) is applied. The exposure time of the camera is set to 1 ms.

The burner configuration used in this study is sketched in Fig. 7.2b. It consists of a stainless steel tube (d = 20 mm) for the premixed gases and a ceramic rod (d = 1 mm) as a flame stabilizer. Homogeneously mixed methane and dry air are fed to the tube at room temperature. All flow rates are controlled by calibrated mass flow controllers (Bronkhorst). Feasibility measurements are performed with an equivalence ratio of 1.0 and a Reynolds number of 1500 based on the tube exit conditions. The flow rate of the mixture is adjusted to stabilize the premixed flame at the rod. Since the V-flame is stabilized at the rod, one branch of the V-flame impinges on a water-cooled stainless steel wall and quenching occurs.

The coordinate system is defined such that z represents the axial direction and x denotes the beam-wise direction. The image is recorded at the quenching position. For the determination of the wall-closest position, the wall, as well as the burner, is moved step-wise perpendicular to the beam-wise direction. At some point, the wall starts to interact with the Raman laser beam and a strong breakdown occurs on the wall surface. Since the beam diameter estimated by the FWHM of the vertical signal profile in the mean image (see Fig. 7.4) is about 240 μm, the wall closest position would be about 120 - 240 μm. In this position, however, a frequent interaction

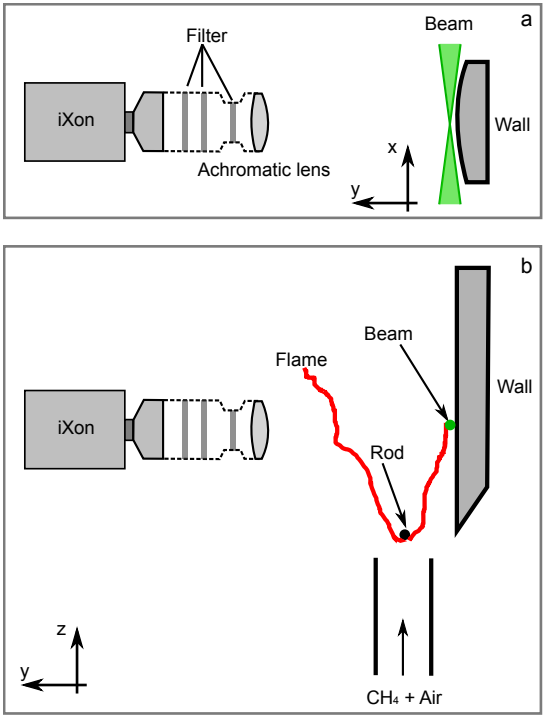

Figure 7.2. Optical arrangement for the Raman imaging. a) Top view, b) side view.

of the laser beam with the wall is observed by beam steering. The measurement point, therefore, is set to another 50 μm further from the wall.

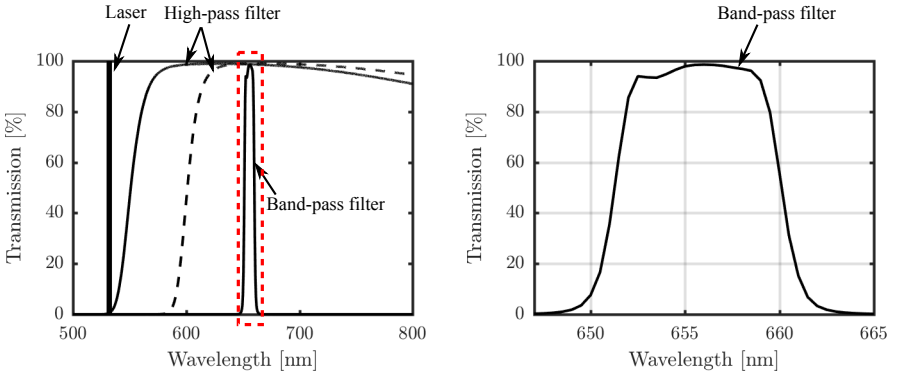

Figure 7.3. Left: The transmittance of filters used in $H_2O_{(g)}$ Raman imaging. Right: Enlargement of the $H_2O_{(g)}$ Raman band-pass filter (red rectangle in the left).

7.4 Results and remarks

Figure 7.4 shows selected instantaneous and ensemble-averaged $H_2O_{(g)}$ Raman images for methane stoichiometric flames during the flame-wall interaction at the wall-closest position. Raman signals significantly fluctuate in the FWI-zone because the test burner is operated in the turbulent configuration.

The power of signal fluctuations, σ_s^2, put into the relation with the power of noise fluctuations, σ_n^2, is known as the signal-to-noise ratio (SNR) and is generally expressed in decibels [175] as follows

$$\text{SNR} \quad [\text{dB}] = +10\log\left(\frac{\overline{\sigma_s^2}}{\overline{\sigma_n^2}}\right). \tag{7.2}$$

Figure 7.5 shows the intensity curves long the dotted lines in Fig. 7.4. For the estimation of the SNR, the signal fluctuations are distinguished from the noise in the raw images. Thus, the intensity of the rectangle area in Fig. 7.5 averaged in space and time is taken as a background value, and the intensity profiles in Fig. 7.5 are used for the evaluation of the SNR. The calculated background intensity is subtracted from the peak value of the selected profile, which is defined as the signal fluctuation, σ_s^2, whereas the deviation from the background is defined as the noise, σ_n^2. The calculated SNR is averaged in time for instantaneous images. The

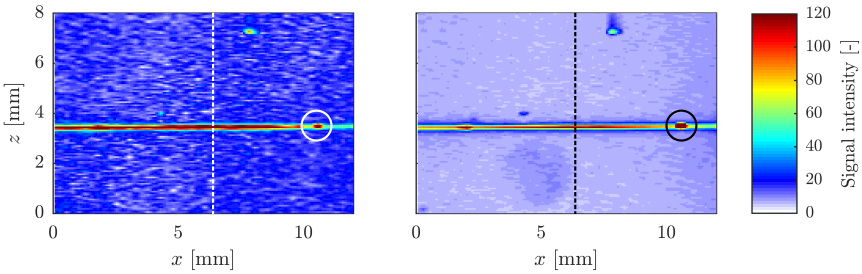

Figure 7.4. Left: Instantaneous $H_2O_{(g)}$ Raman image during FWI for a stoichiometric methane flame. Right: Ensemble-averaged $H_2O_{(g)}$ Raman image during FWI for a methane flame. The high intensity in the circle-marked area is due to a small groove on the wall. Statistics are based on 1000 samples.

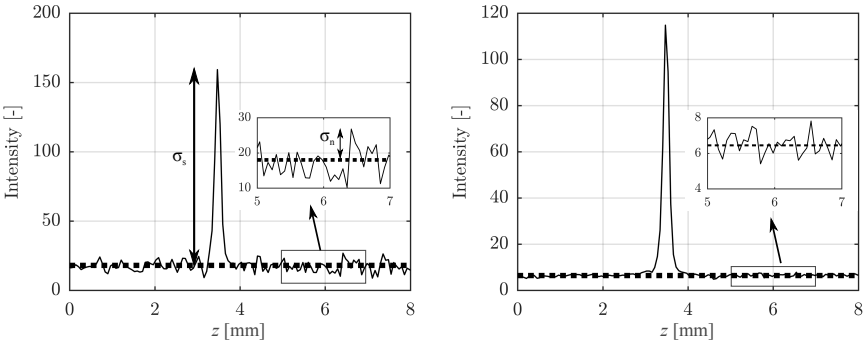

Figure 7.5. Intensity curves along the marked area with dotted lines in Fig. 7.4. Left: The profile derived from instantaneous $H_2O_{(g)}$ Raman images. Right: The profile derived from ensemble-averaged $H_2O_{(g)}$ Raman images.

resulting SNR in instantaneous images is ≈ 23 dB ($\overline{\sigma_s}/\overline{\sigma_n} \approx 28$) , and ≈ 37 dB ($\overline{\sigma_s}/\overline{\sigma_n} \approx 55$) in the averaged image, which are suitable for further measurements.

As a remark, the high intensity in the circle-marked area in Fig. 7.4 is due to the small groove on the wall formed by the laser beam touching the wall for an instant. Even with an instant interaction between the laser and wall, the laser energy is high enough to form the groove on the wall. For further measurements, special care is necessary to avoid such interactions.

As an outlook for further research in this area, an in-situ calibration should be performed to quantify the signal with the temperature information. By analogy to the CO calibration method discussed in Section 5.1.2, the tube heater with a water evaporator can be used in the range of low temperatures (300 - 1000 K). The $H_2O_{(g)}$ concentration in the measurement volume is calculated by the exact knowledge of mass flows assumed as homogeneous mixture. For higher temperatures, the calibration is carried out with the flat flame burner. The equilibrium $H_2O_{(g)}$ is determined by the one-dimensional flamelet calculation. For the temperature data, CARS thermometry can be applied. A calibration table of the $H_2O_{(g)}$ Raman signal at different temperatures and $H_2O_{(g)}$ concentrations should be created. The Raman signal must also be corrected to the excitation energy measured in the single shot. Furthermore, the influence of the wall reflection on the Raman signal at different wall distances should be determined and taken into account by a geometric correction factor.

8 Conclusions and outlook

The flame-wall interaction (FWI) is a combination of many individual processes between flame, wall and flow, which is characterized by very small spatial and temporal scales. During FWI, the flame quenching generally takes place in the sub-millimeter range and in the order of one millisecond. The state of today's experimental and numerical combustion research is far from the capability of fully explaining the fundamental phenomena of the FWI in complex and application-oriented configurations. The aim of this work is to investigate and characterize FWI by means of suitable laser-optical methods. Experiments were performed on generic burner configurations with the side-wall configuration, where a branch of a V-flame interacts with a laterally oriented and temperature-controlled wall. Laminar and turbulent boundary conditions were generated and compared with each other. Many measurement results of the turbulent flame could be explained and understood on the basis of the much simpler laminar flames.

As measurement methods, a number of modern laser diagnostic technique (PIV, CARS, CO-/OH-/CH_2O-LIF and phosphor thermometry) were used in various experimental setups, including the system relevant parameters of equivalence ratio, wall temperature and fuel type. By combining different methods, a large number of variables, such as gas phase/wall surface temperature, CO concentration and CH_2O/OH distributions, could be measured and correlated simultaneously. This is required for answering the questions listed in the introduction of this thesis. In the following section, the most important findings will be summarized.

Heat transfer to the wall

The basis of FWI processes is the large heat loss of the flame across the wall. Thus, the knowledge of wall heat fluxes in this area is necessary for the understanding of FWI. In this work, CARS and phosphor thermometry were combined to investigate side-wall quenching for various wall temperatures ranging from 330 to 670 K and for two different fuels (methane and DME) in stoichiometric mixtures with air. From the comprehensive measurements, gas and wall temperature profiles wall heat fluxes and quenching distances were deduced. The main findings are summarized as follows:

- With increasing wall temperature, quenching heights and quenching distances decrease due to increased laminar flame speeds in the boundary layer. Compared to methane/air flames, DME/air flames are quenched further upstream at smaller quenching distances, which is also attributed to increased laminar flame speeds.

- At the location of flame quenching, wall heat fluxes are larger for elevated wall temperatures because the flame burns closer to the wall (reduced quenching distances).

- Downstream of the quenching location, wall heat fluxes are lower for elevated temperatures as is expected for chemically non-reactive fluids.

Thermochemical state during the flame-wall interaction

The interaction pathways in FWI were investigated in a further measurement of thermochemical states in terms of CO/T scatter plots. Thermochemical states provide the opportunity to look at the flame dynamics with flame chemistry. Temperature and CO concentrations were simultaneously measured by CARS and CO-LIF. Above all, in the fixed viewpoint, the significantly greater influence on the CO oxidation in the vicinity of the wall was shown in comparison to the CO formation. A comparison with numerical results from one-dimensional flame calculations was also used to understand the behavior. The main findings are listed as follows:

- For laminar flow conditions, the CO formation branch at locations very close to the wall is shifted to lower temperatures specifically for flames fueled with methane, whereas for DME, CO formation remains much less affected. This behavior is explained by comparing time scales of CO formation to those of the heat transfer. For CO oxidation, heat transfer is always faster such that the CO oxidation branch is shifted to lower temperatures for the entire near-wall region.

- Laminar one-dimensional flame calculations accounting for the wall heat transfer are capable to correctly represent the experimental trend in the CO oxidation region, whereas the effect of the wall on the CO formation branch cannot be reproduced. CO formation close to the wall is significantly influenced by multi-dimensional heat transfer and species diffusion, which cannot be modelled by a one-dimensional approach.

- For turbulent flow conditions (only methane/air flame), intermediate states between the CO formation and oxidation branches are populated due to

turbulent mixing. Compared to laminar flame conditions, the CO formation branch is less affected which is in accordance with the integral time scale of turbulent heat transfer. Time scales of the CO oxidation branch are larger than the integral time scales and are consequently shifted to lower temperatures in the entire near-wall region.

Local heat release rate of the near-wall flame

Relative HRRs were estimated using the correlation of the product of relative CH_2O- and OH-distributions, derived from PLIF imaging. CH_2O-PLIF signals retain high values even very close to the wall. In contrast, OH-PLIF signals decrease more rapidly when the flame approaches the wall. Broadening of the CH_2O distribution and flattening of the OH-signal gradient indicate a change in the flame structure within the flame-wall interaction zone. These findings are similar for laminar and turbulent flow conditions. However, in the turbulent case, fluctuations prevail in the FWI zone and were analyzed statistically regarding flame curvature. Comparing the near-wall curvature with different wall temperatures, flame curvature decreased with higher wall temperatures due to increased viscosity of higher temperature near-wall gases. The correlation of heat release rate, flame curvature and wall-normal distance was investigated using the instantaneous HRR images for different wall temperatures and equivalence ratios. The correlation of HRR and curvature shows an indication of the Lewis number effect.

Outlook

From the insights obtained in this work, future activities can be derived. In order to identify factors influencing combustion processes close to the wall, a canonical configuration is still of great importance and it would be necessary to broaden the experimental configurations on the FWI burner. For the wall surface property, in addition to the surface temperature investigated in this work, surface roughness and catalytic properties play important roles in the after-treatment systems of automotive applications. Another focus would be the investigation of further longer-chain fuels. These are characterized by more complex reaction kinetics for the chemistry, so that a greater influence of enthalpy loss to the wall is to be expected.

For future analysis, the combined approach of temperature and CO concentration measurements in the transient FWI is still suitable because reactions related to FWI can be derived, which is only possible to a limited extent in steady-state operation due to the low residence times of the hot gas at the surface. In the stationary operating conditions, there is also hardly any direct contact of the flame with the wall. As shown in the last part of this thesis, Raman spectroscopy is

one of the promising techniques to measure another combustion-related species to characterize thermochemical states.

Numerical studies from simple one-dimensional simulations to direct numerical simulations are always required for deeper understanding of experimental results. The comparison of experimental and numerical results can also contribute to near-wall modeling which needs to be improved especially for more complex systems, such as the existing pressurized combustion chamber or high temperature burners.

Bibliography

[1] Aldén, M., Wallin, S., and Wendt, W. "Applications of two-photon absorption for detection of CO in combustion gases". In: *Applied Physics B Photophysics and Laser Chemistry* 33.4 (1984), pp. 205–208.

[2] Allison, S. W. and Gillies, G. T. "Remote thermometry with thermographic phosphors: Instrumentation and applications". In: *Review of Scientific Instruments* 68.7 (1997), pp. 2615–2650.

[3] Andrae, J. "Numerical studies of wall effects with laminar methane flames". In: *Combustion and Flame* 128.1-2 (2002), pp. 165–180.

[4] Appel, C., Mantzaras, J., Schaeren, R., Bombach, R., Inauen, A., Kaeppeli, B., Hemmerling, B., and Stampanoni, A. "An experimental and numerical investigation of homogeneous ignition in catalytically stabilized combustion of hydrogen/air mixtures over platinum". In: *Combustion and Flame* 128.4 (2002), pp. 340–368.

[5] Atkins, P. W. and Friedman, R. *Molecular quantum mechanics*. 4. New York: Oxford University Press, 2005.

[6] Ayoola, B., Balachandran, R., Frank, J., Mastorakos, E., and Kaminski, C. "Spatially resolved heat release rate measurements in turbulent premixed flames". In: *Combustion and Flame* 144.1-2 (2006), pp. 1–16.

[7] Banwell, C. N. and McCash, E. M. *Fundamentals of molecular spectroscopy*. McGraw-Hill, 1994.

[8] Barlow, R. S., Dunn, M. J., and Magnotti, G. "Preferential transport effects in premixed bluff-body stabilized CH_4/H_2 flames". In: *Combustion and Flame* 162.3 (2015), pp. 727–735.

[9] Becquerel, H. "On the rays emitted by phosphorescence". In: *Compt. Rend. Hebd. Seances Acad. Sci.* 122 (1896), pp. 420–421.

[10] Bellenoue, M., Kageyama, T., Labuda, S. A., and Sotton, J. "Direct measurement of laminar flame quenching distance in a closed vessel". In: *Experimental Thermal and Fluid Science* 27.3 (2003), pp. 323–331.

[11] Bergmann, V., Meier, W., Wolff, D., and Stricker, W. "Application of spontaneous Raman and Rayleigh scattering and 2DLIF for the characterization of a turbulent $CH_4/H_2/N_2$ jet diffusion flame". In: *Applied Physics B* 66 (1998).

[12] Birss, F. W., and D. A. Ramsay. "Computer assistance in the analysis of molecular spectra: I. rotational structure of high resolution singlet-singlet bands". In: *Computer Phyiscs Communications* 38 (1985), pp. 83–112.

[13] Böckle, S., Kazenwadel, J., Kunzelmann, T., Shin, D.-I., and Schulz, C. "Single-shot laser-induced fluorescence imaging of formaldehyde with XeF excimer excitation". In: *Applied Physics B* 70.5 (2000), pp. 733–735.

[14] Bohlin, A., Jainski, C., Patterson, B. D., Dreizler, A., and Kliewer, C. J. "Multiparameter spatio-thermochemical probing of flame–wall interactions advanced with coherent Raman imaging". In: *Proceedings of the Combustion Institute* 36.3 (2017), pp. 4557–4564.

[15] Bohr, N. "I. On the constitution of atoms and molecules". In: *The London, Edinburgh, and Dublin Philosophical Magazine and Journal of Science* 26.151 (1913), pp. 1–25.

[16] Boltzmann, L. "Ableitung des Stefan'schen Gesetzes, betreffend die Abhängigkeit der Wärmestrahlung von der Temperatur aus der electromagnetischen Lichttheorie". In: *Annalen der Physik* 258.6 (1884), pp. 291–294.

[17] Borghi, R. and Casci, C. "On the Structure and Morphology of Turbulent Premixed Flames". In: *Recent Advances in the Aerospace Sciences* (1985), pp. 117–138.

[18] Boust, B., Bernard, L., Sotton, J., Labuda, S. A., and Bellenoue, M. "A Model of Flame Quenching in Non-Isothermal Initial Conditions". In: *Proceedings of European Combustion Meeting* (2009), pp. 1–6.

[19] Boust, B., Sotton, J., and Bellenoue, M. "Experimental Study by High-Speed Particle Image Velocimetry of Unsteady Flame-Wall Inteaction in Turbulent Combustion". In: *The International Symposia on Applications of Laser Techniques to Fluid Mechanics* 13 (2006).

[20] Boust, B., Sotton, J., and Bellenoue, M. "Unsteady heat transfer during the turbulent combustion of a lean premixed methane–air flame: Effect of pressure and gas dynamics". In: *Proceedings of the Combustion Institute* 31.1 (2007), pp. 1411–1418.

[21] Boust, B., Sotton, J., Labuda, S. A., and Bellenoue, M. "A thermal formulation for single-wall quenching of transient laminar flames". In: *Combustion and Flame* 149.3 (2007), pp. 286–294.

[22] Boxx, I., Arndt, C. M., Carter, C. D., and Meier, W. “High-speed laser diagnostics for the study of flame dynamics in a lean premixed gas turbine model combustor”. In: *Experiments in Fluids* 52.3 (2012), pp. 555–567.

[23] Brackmann, C., Nygren, J., Bai, X., Li, Z., Bladh, H., Axelsson, B., Denbratt, I., Koopmans, L., Bengtsson, P.-E., and Aldén, M. “Laser-induced fluorescence of formaldehyde in combustion using third harmonic Nd:YAG laser excitation”. In: *Spectrochimica Acta Part A: Molecular and Biomolecular Spectroscopy* 59.14 (2003), pp. 3347–3356.

[24] Brand, J. C. D. “The Electronic Spectrum of Formaldehyde”. In: *Journal of the Chemical Society* (1956), pp. 858–872.

[25] Brübach, J., Hage, M., Janicka, J., and Dreizler, A. “Simultaneous phosphor and CARS thermometry at the wall–gas interface within a combustor”. In: *Proceedings of the Combustion Institute* 32.1 (2009), pp. 855–861.

[26] Brübach, J., Janicka, J., and Dreizler, A. “An algorithm for the characterisation of multi-exponential decay curves”. In: *Optics and Lasers in Engineering* 47.1 (2009), pp. 75–79.

[27] Brübach, J., Pflitsch, C., Dreizler, A., and Atakan, B. “On surface temperature measurements with thermographic phosphors: A review”. In: *Progress in Energy and Combustion Science* 39.1 (2013), pp. 37–60.

[28] Bruneaux, G., Akselvoll, K., Poinsot, T., and Ferziger, J. H. “Flame-wall interaction simulation in a turbulent channel flow”. In: *Combustion and Flame* 107.1-2 (1996), pp. 27–36.

[29] Bruneaux, G., Poinsot, T., and Ferziger, J. H. “Premixed flame–wall interaction in a turbulent channel flow: budget for the flame surface density evolution equation and modelling”. In: *Journal of Fluid Mechanics* 349 (1997), pp. 191–219.

[30] Canny, J. “A Computational Approach to Edge Detection”. In: *IEEE Transactions on Pattern Analysis and Machine Intelligence* 8.6 (1986), pp. 679–698.

[31] Cant, R. S. and Mastorakos, E. *An introduction to turbulent reacting flows*. London, Singapore, and Hackensack, NJ: Imperial College Press and Distributed by World Scientific, 2008.

[32] Chang, J., Filipi, Z., Assanis, D., Kuo, T.-W., Najt, P., and Rask, R. “Characterizing the thermal sensitivity of a gasoline homogeneous charge compression ignition engine with measurements of instantaneous wall temperature and heat flux”. In: *International Journal of Engine Research* 6.4 (2005), pp. 289–310.

[33] Chauvy, M., Delhom, B., Reveillon, J., and Demoulin, F.-X. “Flame/Wall Interactions: Laminar Study of Unburnt HC Formation”. In: *Flow, Turbulence and Combustion* 84.3 (2010), pp. 369–396.

[34] *Chem1D: A one-dimensional flame code, developed at Einhoven university of Technology. http://www.combustion.tue.nl/chem1d*.

[35] *CHEMKIN: http://www.reactiondesign.com/products/open/chemkin.html*.

[36] Cheng, R. K., Bill, R. G., and Robben, F. “Experimental study of combustion in a turbulent boundary layer”. In: *Symposium (International) on Combustion* 18.1 (1981), pp. 1021–1029.

[37] Clark, G. and Farrow, R. L. *The CARSFT Code: User and Programmer Information: Sandia National Laboratories*. Livermore, CA, 1990.

[38] Cleary, D. J. and Farrell, P. V. “Single-Surface Flame Quenching Distance dependence on Wall Temperature, Quenching Geometry, and Turbulence”. In: *SAE Technical Paper* 950162 (1995).

[39] Clendening, C. W., Shackleford, W., and Hilyard, R. “Raman scattering measurements in a side-wall quench layer”. In: *Symposium (International) on Combustion* 18.1 (1981), pp. 1583–1590.

[40] Clouthierl, D. J. and Ramsay. D. A. “The Spectroscopy of Formaldehyde and Thioformaldehyde”. In: *Annual Review of Physical Chemistry,* 34 (1983), pp. 31–58.

[41] Coriton, B., Zendehdel, M., Ukai, S., Kronenburg, A., Stein, O. T., Im, S.-K., Gamba, M., and Frank, J. H. “Imaging measurements and LES-CMC modeling of a partially-premixed turbulent dimethyl ether/air jet flame”. In: *Proceedings of the Combustion Institute* 35.2 (2015), pp. 1251–1258.

[42] Curtiss, C. F. and Hirschfelder, J. O. “Transport Properties of Multicomponent Gas Mixtures”. In: *The Journal of Chemical Physics* 17.6 (1949), pp. 550–555.

[43] Dabireau, F., Cuenot, B., Vermorel, O., and Poinsot, T. “Interaction of flames of H_2 + O_2 with inert walls”. In: *Combustion and Flame* 135.1-2 (2003), pp. 123–133.

[44] Damköhler, G. “Der Einfluss der Turbulenz auf die Flammengeschwindigkeit in Gasgemischen.” In: *Zeitschrift für Elektrochemie und angewandte physikalische Chemie* 46 (1940), pp. 601–626.

[45] Daniel, W. A. “Flame quenching at the walls of an internal combustion engine”. In: *Proceedings of the Combustion Institute* 6.1 (1957), pp. 886–894.

[46] Davy, H. “Some new experiments and observations on the combustion of gaseous mixtures, with an account of a method of preserving a continued light in mixtures of inflammable gases and air without flame”. In: *Philosophical Transactions of the Royal Society of London* 107 (1817), pp. 77–85.

[47] Dec, J. E. and Tree, D. R. “Diffusion-Flame / Wall Interactions in a Heavy-Duty DI Diesel Engine”. In: *SAE Technical Paper* 2001-01-1295 (2001).

[48] DeWitt, R. N., Harvey, A. B., and Tolles, W. M. “Theoretical development of third-order susceptibility as related to coherent anti-Stokes Raman spectroscopy (CARS)”. In: *NRL Memorandum* (1976), p. 3260.

[49] Dieke, G. H. and Crosswhite, H. M. “The ultraviolet bands of OH Fundamental data”. In: *Journal of Quantitative Spectroscopy and Radiative Transfer* 2.2 (1962), pp. 97–199.

[50] Dieke, G. H. and Kistiakowsky, G. B. “The Structure of the Ultraviolet Absorption Spectrum of Formaldehyde. I”. In: *Physical Review* 45.4-28 (1934).

[51] Ding, C.-P., Honza, R., Böhm, B., and Dreizler, A. “Simultaneous measurement of flame impingement and piston surface temperatures in an optically accessible spark ignition engine”. In: *Applied Physics B* 123.4 (2017), p. 110.

[52] Donkerbroek, A. J., van Vliet, A. P., Somers, L., Frijters, P., Klein-Douwel, R., Dam, N. J., Meerts, W. L., and ter Meulen, J. J. “Time- and space-resolved quantitative LIF measurements of formaldehyde in a heavy-duty diesel engine”. In: *Combustion and Flame* 157.1 (2010), pp. 155–166.

[53] Drake, M. C. and Haworth, D. C. “Advanced gasoline engine development using optical diagnostics and numerical modeling”. In: *Proceedings of the Combustion Institute* 31.1 (2007), pp. 99–124.

[54] Dreizler, A. and Böhm, B. “Advanced laser diagnostics for an improved understanding of premixed flame-wall interactions”. In: *Proceedings of the Combustion Institute* 35 (2015), pp. 37–64.

[55] Druet, S. A. J. and Taran, J.-P. E. “Cars spectroscopy”. In: *Progress in Quantum Electronics* 7.1 (1981), pp. 1–72.

[56] Eckbreth, A. C. “BOXCARS: Crossed-beam phase-matched CARS generation in gases”. In: *Applied Physics Letters* 32.7 (1978), p. 421.

[57] Eckbreth, A. C. *Laser diagnostics for combustion temperature and species*. 2nd ed. Amsterdam and The Netherlands: Gordon and Breach Publishers, 1996.

[58] Eckbreth, A. C. and Hall, R. J. “CARS Concentration Sensitivity With and Without Nonresonant Background Suppression”. In: *Combustion Science and Technology* 25.5-6 (2008), pp. 175–192.

[59] Eckert, E. R. G. and Drake Jr, R. M. *Analysis of heat and mass transfer*. McGraw-Hill, 1987.

[60] Egolfopoulos, F. N., Zhang, H., and Zhang, Z. “Wall effects on the propagation and extinction of steady, strained, laminar premixed flames”. In: *Combustion and Flame* 109.1-2 (1997), pp. 237–252.

[61] Eitel, F., Pareja, J., Johchi, A., Böhm, B., Geyer, D., and Dreizler, A. “Temporal evolution of auto-ignition of ethylene and methane jets propagating into a turbulent hot air co-flow vitiated with NOx”. In: *Combustion and Flame* 177 (2017), pp. 193–206.

[62] Ern, A. and Giovangigli, V. *Multicomponent Transport Algorithms*. Vol. 24. Lecture Notes in Physics Monographs. Berlin, Heidelberg: Springer Berlin Heidelberg and Springer e-books, 1994.

[63] Ewart, P. “A modeless, variable bandwidth, tunable laser”. In: *Optics Communications* 55.2 (1985), pp. 124–126.

[64] Ezekoye, O. A. and Greif, R. “A comparison of one and two dimensional flame quenching: Heat transfer results”. In: *National conference and exposition on heat transfer* (1993).

[65] Ezekoye, O., Greif, R., and Sawyer, R. F. “Increased surface temperature effects on wall heat transfer during unsteady flame quenching”. In: *Proceedings of the Combustion Institute* 24.1 (1992), pp. 1465–1472.

[66] Frank, J. *Three-dimensional electron microscopy of macromolecular assemblies*. Oxford University Press, 2006.

[67] Fraser, N., Blaxill, H., and Lumsden, Grant, Bassett, Mike. “Challenges for Increased Efficiency through Gasoline Engine Downsizing”. In: *SAE International Journal of Engines* 2.1 (2009).

[68] Friedman, R. and Johnston, W. C. “Pressure Dependence of Quenching Distance of Normal Heptane, Iso-Octane, Benzene, and Ethyl Ether Flames”. In: *The Journal of Chemical Physics* 20.5 (1952), pp. 919–920.

[69] Friedman, R. and Johnston, W. C. “The Wall-Quenching of Laminar Propane Flames as a Function of Pressure, Temperature, and Air-Fuel Ratio”. In: *Journal of Applied Physics* 21.8 (1950), p. 791.

[70] Fuhrmann, N., Brübach, J., and Dreizler, A. “Phosphor thermometry: A comparison of the luminescence lifetime and the intensity ratio approach”. In: *Proceedings of the Combustion Institute* 34.2 (2013), pp. 3611–3618.

[71] Fuhrmann, N., Kissel, T., Dreizler, A., and Brübach, J. “Gd3Ga5O12: Cr—a phosphor for two-dimensional thermometry in internal combustion engines”. In: *Measurement Science and Technology* 22.4 (2011), p. 45301.

[72] Fuhrmann, N., Litterscheid, C., Ding, C.-P., Brübach, J., Albert, B., and Dreizler, A. “Cylinder head temperature determination using high-speed phosphor thermometry in a fired internal combustion engine”. In: *Applied Physics B* 116.2 (2014), pp. 293–303.

[73] Fukui, K., Fujikawa, T., Tohyama, M., Hattori, Y., and Akihama, K. “2-D Internal EGR Distribution Measurements in an Engine by Laser-Induced Fluorescence”. In: *SAE International Journal of Engines* 6.1 (2013), pp. 289–299.

[74] Furuhama, S. and Enomoto, M. “Heat Transfer into Ceramic Combustion Wall of Internal Combustion Engines”. In: *SAE Technical Paper* 870153 (1987).

[75] Fuyuto, T., Kronemayer, H., Lewerich, B., Brübach, J., Fujikawa, T., Akihama, K., Dreier, T., and Schulz, C. “Temperature and species measurement in a quenching boundary layer on a flat-flame burner”. In: *Experiments in Fluids* 49.4 (2010), pp. 783–795.

[76] Gabet, K. N. and Sutton, J. A. “Narrowband versus broadband excitation for CH_2O PLIF imaging in flames using a frequency-tripled Nd: YAG laser”. In: *Experiments in Fluids* 55.7 (2014), p. 1.

[77] Ganter, S., Heinrich, A., Meier, T., Kuenne, G., Jainski, C., Rißmann, M., Dreizler, A., and Janicka, J. “Numerical analysis of laminar methane–air side-wall-quenching”. In: *Combustion and Flame* 186 (2017), pp. 299–310.

[78] Garland, N. L. and Crosley, D. R. “On the collisional quenching of electronically excited OH, NH and CH in flames”. In: *Symposium (International) on Combustion* 21.1 (1988), pp. 1693–1702.

[79] Glassman, I., Yetter, R. A., and Glumac, N. G. *Combustion*. Academic Press, 2014.

[80] Goodwin, D. G. “Cantera: An Object-oriented Software Toolkit for Chemical Kinetics, Thermodynamics, and Transport Processes”. In: *http://code.google.com/p/cantera* (2009).

[81] Goolsby, A. D. and Haskell, W. W. “Flame-quench distance measurements in a CFR engine”. In: *Combustion and Flame* 26 (1976), pp. 105–114.

[82] Gordon, R. L., Masri, A. R., and Mastorakos, E. “Simultaneous Rayleigh temperature, OH- and CH_2O-LIF imaging of methane jets in a vitiated coflow”. In: *Combustion and Flame* 155.1-2 (2008), pp. 181–195.

[83] Gregor, M. A. and Dreizler, A. “A quasi-adiabatic laminar flat flame burner for high temperature calibration”. In: *Measurement Science and Technology* 20.6 (2009), pp. 1–7.

[84] Gruber, A., Sankaran, R., Hawkes, E. R., and Chen, J. H. “Turbulent flame–wall interaction: a direct numerical simulation study”. In: *Journal of Fluid Mechanics* 658 (2010), pp. 5–32.

[85] Gulder, Ö. L. “Laminar Burning Velocities of Methanol, Isooctane and Isooctane/Methanol Blends”. In: *Combustion Science and Technology* 33.1-4 (2007), pp. 179–192.

[86] H. J. Curran, W. J. Pitz, C. K. Westbrook, P. Dagaut, J-C Boettner, and M. Cathonnet. “A wide range modeling study of dimethyl ether oxidation”. In: *International Journal of Chemical Kinetics* 30.3 (1998), pp. 229–241.

[87] Häber, T. and Suntz, R. “Effect of different wall materials and thermal-barrier coatings on the flame-wall interaction of laminar premixed methane and propane flames”. In: *International Journal of Heat and Fluid Flow* 69 (2018), pp. 95–105.

[88] Hanson, R. K., Seitzman, J. M., and Paul, P. H. “Planar laser-fluorescence imaging of combustion gases”. In: *Applied Physics B Photophysics and Laser Chemistry* 50.6 (1990), pp. 441–454.

[89] Haq, M. Z., Sheppard, C. G. W., Woolley, R., Greenhalgh, D. A., and Lockett, R. D. “Wrinkling and Curvature of Laminar and Turbulent Premixed Flames”. In: *Combustion and Flame* 131.1-2 (2002), pp. 1–15.

[90] Hasse, C., Bollig, M., Peters, N., and Dwyer, H. A. “Quenching of laminar iso-octane flames at cold walls”. In: *Combustion and Flame* 122.1-2 (2000), pp. 117–129.

[91] Herzberg, G. *Molecular spectra and molecular structure*. 2. New York, NY: Krieger Publishing Company, 1989.

[92] Hoffman, D., Münch, K. U., and Leipertz, A. “Two-dimensional temperature determination in sooting flames by filtered Rayleigh scattering”. In: *Optics letters* 21.7 (1996), pp. 525–527.

[93] Huang, W. M., Vosen, S. R., and Greif, R. “Heat transfer during laminar flame quenching: Effect of fuels”. In: *Symposium (International) on Combustion* 21.1 (1986), pp. 1853–1860.

[94] Huber, K. P. and Herzberg, G. *Molecular Spectra and Molecular Structure IV. Constants of Diatomic Molecules*. New York, 1979.

[95] Hyvönen, J., Haraldsson, G., and Johansson, B. “Operating Conditions Using Spark Assisted HCCI Combustion During Combustion Mode Transfer to SI in a Multi-Cylinder VCR-HCCI Engine”. In: *SAE Technical Paper* 2005-01-0109 (2005).

[96] Jackson, J. D. *Classical electrodynamics*. 3. New York, NY: Wiley, 1999.

[97] Jainski, C. “Experimentelle Untersuchung der turbulenten Flamme-Wand-Interaktion”. Dissertation. Technische Universität Darmstadt, 2016.

[98] Jainski, C., Lu, L., Dreizler, A., and Sick, V. “High-speed micro particle image velocimetry studies of boundary-layer flows in a direct-injection engine”. In: *International Journal of Engine Research* 14.3 (2012), pp. 247–259.

[99] Jainski, C., Rißmann, M., Böhm, B., and Dreizler, A. “Experimental investigation of flame surface density and mean reaction rate during flame–wall interaction”. In: *Proceedings of Combustion Institute* 36.2 (2017), pp. 1827–1834.

[100] Jainski, C., Rißmann, M., Böhm, B., Janicka, J., and Dreizler, A. “Sidewall quenching of atmospheric laminar premixed flames studied by laser-based diagnostics”. In: *Combustion and Flame* 183 (2017), pp. 271–282.

[101] Jainski, C., Rißmann, M., Jakirlic, S., Böhm, B., and Dreizler, A. “Quenching of Premixed Flames at Cold Walls: Effects on the Local Flow Field”. In: *Flow Turbulence Combust.* 25 (2017), p. 253.

[102] Janas, P., Wlokas, I., Böhm, B., and Kempf, A. “On the Evolution of the Flow Field in a Spark Ignition Engine”. In: *Flow, Turbulence and Combustion* 98.1 (2017), pp. 237–264.

[103] Judge, R. H. and Clouthier, D. J. “AsyrotWin: A 32-bit Windows version of Asyrot, A program for the analysis of high resolution singlet-singlet band spectra of asymmetric tops”. In: *Computer Physics Communications* 135.3 (2001), pp. 293–311.

[104] Kee, R. J., Grcar, J. F., Smooke, M. D., Miller, J. A., and Meeks, E. “PREMIX:A FORTRAN Program for Modeling Steady Laminar One-Dimensional Premixed Flames”. In: *Sandia Report* SAND85-8249 (1985).

[105] Kim, H., Cho, S., and Min. K. “Reduced Chemical Kinetic Model of DME for HCCI Combustion”. In: *SAE Technical Paper* 2003-01-1822 (2003).

[106] Kissel, T. “Spektroskopische Methoden zur Charakterisierung wandnaher Verbrennungsvorgänge”. Dissertation. Technische Universität Darmstadt, 2011.

[107] Kissel, T., Baum, E., Dreizler, A., and Brübach, J. “Two-dimensional thermographic phosphor thermometry using a CMOS high speed camera system”. In: *Applied Physics B* 96.4 (2009), pp. 731–734.

[108] Klein-Douwel, R. J. H., Luque, J., Jeffries, J. B., Smith, G. P., and Crosley, D. R. “Laser-induced fluorescence of formaldehyde hot bands in flames”. In: *Applied Optics* 39.21 (2000), p. 3712.

[109] Klinkenberg, A. and Mooy, H. H. “Dimensionless groups in fluid friction, heat, and material transfer”. In: *Chemical Engineering Progress* 44.1 (1948), pp. 17–36.

[110] Kohse-Höinghaus, K. and Jeffries, J. B. *Applied combustion diagnostics*. New York: Taylor & Francis, 2002.

[111] Kolmogorov, A. N. “The Local Structure of Turbulence in Incompressible Viscous Fluid for Very Large Reynolds Numbers”. In: *Dokl. Akad. Nauk SSSR* 30 (1941), pp. 301–305.

[112] Kosaka, H., Zentgraf, F., Böhm, B., and Dreizler, A. “Heat release rate imaging during side-wall flame quenching using laser-induced fluorescence of formaldehyde and hydroxyl radicals”. In: *Proceedings of 19th International Symposium on the Application of Laser and Imaging Techniques to Fluid Mechanics* (2018).

[113] Kosaka, H., Zentgraf, F., Scholtissek, A., Bischoff, L., Häber, T., Suntz, R., Albert, B., Hasse, C., and Dreizler, A. “Wall heat fluxes and CO formation/oxidation during laminar and turbulent side-wall quenching of methane and DME flames”. In: *International Journal of Heat and Fluid Flow* 70 (2018), pp. 181–192.

[114] Kyritsis, D. C., Santoro, V. S., and Gomez, A. “The effect of temperature correction on the measured thickness of formaldehyde zones in diffusion flames for 355 nm excitation”. In: *Experiments in Fluids* 37.5 (2004), pp. 769–772.

[115] Law, C. K., Jomaas, G., and Bechtold, J. K. “Cellular instabilities of expanding hydrogen/propane spherical flames at elevated pressures: Theory and experiment”. In: *Proceedings of the Combustion Institute* 30.1 (2005), pp. 159–167.

[116] Lewis, B. and von Elbe, G. *Combustion, Flames, and Explosions of Gases*. New York: Academic Press, 1951.

[117] Lewis, W. K. “The evaporation of a liquid into a gas”. In: *Transactions of ASME* 44 (1922), pp. 325–340.

[118] Li, T., Pareja, J., Fuest, F., Schütte, M., Zhou, Y., Dreizler, A., and Böhm, B. “Tomographic imaging of OH laser-induced fluorescence in laminar and turbulent jet flames”. In: *Measurement Science and Technology* 29.1 (2018), p. 15206.

[119] Lichtman, J. W. and Conchello, J.-A. “Fluorescence microscopy”. In: *Nature methods* 2.12 (2005), pp. 910–919.

[120] Linow, S., Dreizler, A., Janicka, J., and Hassel, E. P. “Comparison of two-photon excitation schemes for CO detection in flames”. In: *Applied Physics B: Lasers and Optics* 71.5 (2000), pp. 689–696.

[121] Lowry, W. B., Serinyel, Z., Krejci, M. C., Curran, H. J., Bourque, G., and Petersen, E. L. “Effect of methane-dimethyl ether fuel blends on flame stability, laminar flame speed, and Markstein length”. In: *Proceedings of the Combustion Institute* 33.1 (2011), pp. 929–937.

[122] Lu, J. H., Ezekoye, O. A., Greif, R., and Sawyer, R. F. “Unsteady heat transfer during side wall quenching of a laminar flame”. In: *Proceedings of the Combustion Institute* 23.1 (1990), pp. 441–446.

[123] Luque, J. and Crosley D. R. “LIFBASE: Database and simulation program (v 1.6)”. In: *SRI International Report MP* (1999), pp. 99–004.

[124] Luque, J., Jeffries, J. B., Smith, G. P., and Crosley, D. R. “Quasi-simultaneous detection of CH_2O and CH by cavity ring-down absorption and laser-induced fluorescence in a methane/air low-pressure flame”. In: *Applied Physics B: Lasers and Optics* 73.7 (2001), pp. 731–738.

[125] Maeding, C., Wiedmann, D., Quering, K., and Knab, O. “Improved heat transfer prediction engineering capabilities for rocket thrust chamber layout”. In: *Progress in Propulsion Physics* 2 (2011), pp. 239–250.

[126] Mann, M., Jainski, C., Euler, M., Böhm, B., and Dreizler, A. “Transient flame–wall interactions: Experimental analysis using spectroscopic temperature and CO concentration measurements”. In: *Combustion and Flame* 161.9 (2014), pp. 2371–2386.

[127] Marín, E. “Characteristic dimensions for heat transfer”. In: *Latin-American Journal of Physics Education* 4.1 (2010), pp. 56–60.

[128] Maxwell, J. C. “A Dynamical Theory of the Electromagnetic Field”. In: *Philosophical Transactions of the Royal Society of London* 155 (1865), pp. 459–512.

[129] McQuarrie, D. A. *Statistical Mechanics*. University Science, Sausalito, 2000.

[130] Meller, R. and Moortgat, G. K. “Temperature dependence of the absorption cross sections of formaldehyde between 223 and 323 K in the wavelength range 225-375 nm”. In: *Journal of Geophysical Research: Atmospheres* 105.D6 (2000), pp. 7089–7101.

[131] Menzel, R. *Photonics*. [New York]: Springer-Verlag Berlin Heidelberg, 2007.

[132] Miles, R. B., Lempert, W. R., and Forkey, J. N. “Laser Rayleigh scattering”. In: *Measurement Science and Technology* 12.5 (2001), pp. 33–51.

[133] Moule, D. C. and Walsh, A. D. “Ultraviolet spectra and excited states of formaldehyde”. In: *Chemical Reviews* 75.1 (1975), pp. 67–84.

[134] Najm, H. N., Paul, P. H., Mueller, C. J., and Wyckoff, P. S. “On the Adequacy of Certain Experimental Observables as Measurements of Flame Burning Rate”. In: *Combustion and Flame* 113.3 (1998), pp. 312–332.

[135] Navier, C. L. M. H. “Mémoire sur les lois du mouvement des fluides”. In: *Mémoires de l’Académie Royale des Sciences de l’Institut de France* 6 (1823), pp. 389–440.

[136] OECD/IEA. *Global Energy & CO2 Status Report 2017*. Vol. 25. 2018.

[137] Paul, P. H. and Najm, H. N. “Planar laser-induced fluorescence imaging of flame heat release rate”. In: *Symposium (International) on Combustion* 27.1 (1998), pp. 43–50.

[138] Peters, N. “The turbulent burning velocity for large-scale and small-scale turbulence”. In: *Journal of Fluid Mechanics* 384 (1999), pp. 107–132.

[139] Peterson, B., Baum, E., Böhm, B., and Dreizler, A. “Early flame propagation in a spark-ignition engine measured with quasi 4D-diagnostics”. In: *Proceedings of the Combustion Institute* 35.3 (2015), pp. 3829–3837.

[140] Planck, M. “Über irreversible Strahlungsvorgänge”. In: *Annalen der Physik* 306.1 (1900), pp. 69–122.

[141] Poinsot, T., Haworth, D., and Bruneaux, G. “Direct simulation and modeling of flame-wall interaction for premixed turbulent combustion”. In: *Combustion and Flame* 95.1-2 (1993), pp. 118–132.

[142] Poinsot, T. and Veynante, D. *Theoretical and numerical combustion*. 3. Bordeaux, France: self-publishing, 2012.

[143] Pope, S. B. *Turbulent flows*. Cambridge, NY: Cambridge University Press, 2000.

[144] Popp, P. and Baum, M. "Analysis of wall heat fluxes, reaction mechanisms, and unburnt hydrocarbons during the head-on quenching of a laminar methane flame". In: *Combustion and Flame* 108.3 (1997), pp. 327–348.

[145] Popp, S. *Simulation of CH_2O-LIF signals: Pernonal communication*. 08.05.2018.

[146] Popp, S., Hunger, F., Hartl, S., Messig, D., Coriton, B., Frank, J. H., Fuest, F., and Hasse, C. "LES flamelet-progress variable modeling and measurements of a turbulent partially-premixed dimethyl ether jet flame". In: *Combustion and Flame* 162.8 (2015), pp. 3016–3029.

[147] Prandtl, L. "Bericht uber Untersuchungen zur ausgebildeten Turbulenz". In: *Zeitschrift für Angewandte Mathematik und Mechanik* 5 (1925), pp. 136–139.

[148] Raffel, M. *Particle image velocimetry: A practical guide*. 2nd ed. Experimental fluid mechanics. Heidelberg and Berlin: Springer, 2007.

[149] Reynolds, O. "An experimental investigation of the circumstances which determine whether the motion of water shall be direct or sinuous, and of the law of resistance in parallel channels". In: *Proceedings of the royal society of London* 35.224-226 (1883), pp. 84–99.

[150] Rißmann, M., Jainski, C., Mann, M., and Dreizler, A. "Flame-Flow Interaction in Premixed Turbulent Flames During Transient Head-On Quenching". In: *Flow, Turbulence and Combustion* 98.4 (2017), pp. 1025–1038.

[151] Rogers, J. D. "Ultraviolet absorption cross sections and atmospheric photodissociation rate constants of formaldehyde". In: *Journal of Physical Chemistry* 94 (1990), pp. 4011–4015.

[152] Roy, S., Gord, J. R., and Patnaik, A. K. "Recent advances in coherent anti-Stokes Raman scattering spectroscopy: Fundamental developments and applications in reacting flows". In: *Progress in Energy and Combustion Science* 36.2 (2010), pp. 280–306.

[153] Schiessl, R., Pixner, P., Dreizler, A., and Maas, U. "Formaldehyde formation in the endgas of Otto engines: Numerical simulations and quantitative concentration measurements". In: *Combustion Science and Technology* 149.1-6 (1999), pp. 339–360.

[154] Schlichting, H. and Gersten, K. *Boundary layer theory: With 22 tables*. 8. Berlin: Springer, 2003.

[155] Schneider, S. "Auswirkungen der Wasserstoff-Zumischung auf die Flammenstruktur turbulenter stratifizierter Methan-Luft-Flammen". Dissertation. Technische Universität Darmstadt, 2017.

[156] Schrödinger, E. "An Undulatory Theory of the Mechanics of Atoms and Molecules". In: *Physical Review* 28.6 (1926), pp. 1049–1070.

[157] Schulz, C. and Sick, V. "Tracer-LIF diagnostics: quantitative measurement of fuel concentration, temperature and fuel/air ratio in practical combustion systems". In: *Progress in Energy and Combustion Science* 31.1 (2005), pp. 75–121.

[158] Seitzman, J. M., Haumann, J., and Hanson, R. K. "Quantitative two-photon LIF imaging of carbon monoxide in combustion gases". In: *Applied Optics* 26.14 (1987), pp. 2892–2899.

[159] Seitzman, J., Üngüt, A., Paul, P. H., and Hanson, R. K. "PLIF imaging and analysis of OH structures in a turbulent nonpremixed H_2- air flame (Planar Laser Induced Fluorescence)". In: *AIAA, Aerospace Sciences Meeting, 28 th, Reno, NV*. 1990.

[160] Semelsberger, T. A., Borup, R. L., and Greene, H. L. "Dimethyl ether (DME) as an alternative fuel". In: *Journal of Power Sources* 156.2 (2006), pp. 497–511.

[161] Settersten, T. B., Dreizler, A., and Farrow, R. L. "Temperature- and species-dependent quenching of CO B probed by two-photon laser-induced fluorescence using a picosecond laser". In: *The Journal of Chemical Physics* 117.7 (2002), p. 3173.

[162] Shibuya, K., Fairchild, P. W., and Lee, E. K. C. "Single rotational level fluorescence quantum yields, radiative lifetimes, and nonradiative decay rates of S_1 D_2CO and $H_2CO(\tilde{A}^1A^2, 4^1)$: Rotational dependence". In: *The Journal of Chemical Physics* 75.7 (1981), pp. 3397–3406.

[163] Shin, D. I., Dreier, T., and Wolfrum, J. "Spatially resolved absolute concentration and fluorescence-lifetime determination of H_2CO in atmospheric-pressure CH_4/air flames". In: *Applied Physics B* 72.2 (2001), pp. 257–261.

[164] Smith, G. P. et al. "GRI-Mech 3.0". In: *http://www. me. berkley. edu/ gri_mech/* (1999).

[165] Sotton, J., Boust, B., Labuda, S. A., and Bellenoue, M. “Head-on quenching of transient laminar flame: Heat flux and quenching distance measurements”. In: *Combustion Science and Technology* 177.7 (2005), pp. 1305–1322.

[166] Spurk, J. H. and Aksel, N. *Strömungslehre: Einführung in die Theorie der Strömungen*. 6. Berlin, Heidelberg: Springer, 2006.

[167] Spurk, J. H. and Aksel, N. *Fluid Mechanics Second Edition*. 2008.

[168] Stefan, J. “Über die Beziehung zwischen der Wärmestrahlung und der Temperatur, Sitzungsberichte der mathematisch-naturwissenschaftlichen Classe der kaiserlichen”. In: *Akademie der Wissenschaften* 79 (1879), pp. 391–428.

[169] Steinberg, A. M., Boxx, I., Stöhr, M., Meier, W., and Carter, C. D. “Effects of flow structure dynamics on thermoacoustic instabilities in swirl-stabilized combustion”. In: *AIAA Journal* 50.4 (2012).

[170] Stevens, E. J., Bray, K. N. C., and Lecordier, B. “Velocity and scalar statistics for premixed turbulent stagnation flames using PIV”. In: *Symposium (International) on Combustion* 27.1 (1998), pp. 949–955.

[171] Stokes, G. G. “On the theories of the internal friction of fluids in motion”. In: *Transactions of the Cambridge Philosophical Society* 8 (1845), pp. 287–319.

[172] Strickler, S. J. and Barnhart, R. J. “Absolute vibronic intensities in the $^1A_2 \leftarrow ^1A_1$ absorption spectrum of formaldehyde”. In: *Journal of Physical Chemistry* 84.4 (1982), pp. 448–455.

[173] Sutera, S. P., Maeder, P. F., and Kestin, J. “Vorticity amplification in stagnation-point flow and its effect on heat transfer”. In: *Journal of Fluid Mechanics* 21.03 (1965), pp. 513–534.

[174] Tamura, M., Berg, P. A., Harrington, J. E., Luque, J., Jeffries, J. B., Smith, G. P., and Crosley, D. R. “Collisional Quenching of CH(A), OH(A), and NO(A) in Low Pressure Hydrocarbon Flames”. In: *Combustion and Flame* 114.3-4 (1998), pp. 502–514.

[175] Tropea, C., Yarin, A. L., and Foss, J. F. *Springer handbook of experimental fluid mechanics*. Berlin: Springer, 2007.

[176] Trunk, P. J., Boxx, I., Heeger, C., Meier, W., Böhm, B., and Dreizler, A. “Premixed flame propagation in turbulent flow by means of stereoscopic PIV and dual-plane OH-PLIF at sustained kHz repetition rates”. In: *Proceedings of the Combustion Institute* (2012).

[177] Turns, S. R. *An introduction to combustion*. 2. Boston: McGraw-Hill, 2006.

[178] Valeur, B. and Berberan-Santos, M. N. *Molecular fluorescence: principles and applications*. John Wiley & Sons, Inc, 2012.

[179] Vitta, P., Pobedinskas, P., and Zukauskas, A. "Phosphor Thermometry in White Light-Emitting Diodes". In: *IEEE Photonics Technology Letters* 19.6 (2007), pp. 399–401.

[180] von Kármán, T. "Mechanische Ähnlichkeit und Turbulenz". In: *Nachrichten von der Gesellschaft der Wissenschaften zu Göttingen : Mathematisch-physische Klasse* (1930), pp. 58–76.

[181] von Kármán, T. and Millán, G. "Thermal theory of a laminar flame front near a cold wall". In: *Proceedings of the Combustion Institute* 4.1 (1953), pp. 173–177.

[182] Vosen, S., Greif, R., and Westbrook, C. "Unsteady heat transfer during laminar flame quenching". In: *Proceedings of the Combustion Institute* 20.1 (1984), pp. 75–83.

[183] Wakisaka, Y., Inayoshi, M., Fukui, K., Kosaka, H., Hotta, Y., Kawaguchi, A., and Takada, N. "Reduction of Heat Loss and Improvement of Thermal Efficiency by Application of "Temperature Swing" Insulation to Direct-Injection Diesel Engines". In: *SAE Technical Paper* 2016-01-0661 (2016).

[184] Wang, Y. and Trouvé, A. "Direct numerical simulation of non-premixed flame-wall interactions". In: *Journal of Physics: Conference Series* 16 (2005), pp. 119–123.

[185] Warnatz, J., Maas, U., and Dibble, R. W. *Combustion*. 4. Berlin and Heidelberg [u.a.]: Springer, 2006.

[186] Weber, V., Brübach, J., Gordon, R. L., and Dreizler, A. "Pixel-based characterisation of CMOS high-speed camera systems". In: *Applied Physics B* 103.2 (2011), pp. 421–433.

[187] Westbrook, C. K., Adamczyk, A. A., and Lavoie, G. A. "A numerical study of laminar flame wall quenching". In: *Combustion and Flame* 40 (1981), pp. 81–99.

[188] Woschni, G., Spindler, W., and Kolesa, K. "Heat Insulation of Combustion Chamber Walls — A Measure to Decrease the Fuel Consumption of I.C. Engines?" In: *SAE Technical Paper* 870339 (1987).

[189] Wu, K.-C. and Hochgreb, S. "The Roles of Chemistry and Diffusion on Hydrocarbon Post-Flame Oxidation". In: *Combustion Science and Technology* 130.1-6 (1997), pp. 365–398.

[190] Yu, H., Hu, E., Cheng, Y., Yang, K., Zhang, X., and Huang, Z. “Effects of Hydrogen Addition on the Laminar Flame Speed and Markstein Length of Premixed Dimethyl Ether–Air Flames”. In: *Energy & Fuels* 29.7 (2015), pp. 4567–4575.

[191] Zabetakis, M. G. “Flammability characteristics of combustible gases and vapors”. In: *Bureau of Mines Washington DC* 627 (1965).

[192] Zhao, Z., Chaos, M., Kazakov, A., and Dryer, F. L. “Thermal decomposition reaction and a comprehensive kinetic model of dimethyl ether”. In: *International Journal of Chemical Kinetics* 40.1 (2008), pp. 1–18.

[193] Zschutschke, A., Messig D., Scholtissek, A., and Hasse, C. “Universal Laminar Flame Solver (ULF)”. In: *https://doi.org/10.6084/m9.figshare.5119855.v2* (2017).